Technical Report
TR-22-05
September 2022

Creep rate in Cu-OFP under applied electrochemical potential and presence of sulphide

Tiina Ikäläinen
Timo Saario
Zaiqing Que

SVENSK KÄRNBRÄNSLEHANTERING AB

SWEDISH NUCLEAR FUEL
AND WASTE MANAGEMENT CO

Box 3091, SE-169 03 Solna
Phone +46 8 459 84 00
skb.se

SVENSK KÄRNBRÄNSLEHANTERING

ISSN 1404-0344
SKB TR-22-05
ID 1975974

September 2022

Creep rate in Cu-OFP under applied electrochemical potential and presence of sulphide

Tiina Ikäläinen, Timo Saario, Zaiqing Que
VTT Technical Research Centre of Finland Ltd.

Keywords: Cu-OFP, Creep rate, Sulphide, Polarisation.

Summary

The main objectives of this work were to find if the creep rate of Cu-OFP is influenced by the presence of sulphide and either anodic or cathodic polarisation.

In the first part of the study performed in sodium nitrite (1M $NaNO_2$) without sulphide, the creep rate was found to be accelerated by anodic polarisation to +1 mA/cm^2. However, the reason for the acceleration remains somewhat unresolved since the specimen failed by SCC, and the contribution of SCC micro-cracks (forming early on during the test) onto the creep rate could not be determined.

Without polarisation (i.e. at the corrosion potential), addition of sulphide (up to 10^{-3} M, equivalent to 25 mg/l) had no measurable effect on the creep rate. However, stopping the sulphide feed resulted, after some incubation time, in a transient increase of creep rate by about an order of magnitude, lasting for about 40 hours. Anodic polarisation to +1 mA/cm^2 resulted in a clear (transient) acceleration of creep, although smaller than in the case of 1M $NaNO_2$. Cathodic polarisation resulted (in some cases) in a similar transient increase of creep rate. These results may possibly be due to reductive dissolution of films resulting in injection of vacancies into Cu-OFP (in case of anodic polarisation), or to hydrogen entering the Cu-OFP material and interacting with the dislocation structure (in case of cathodic polarisation), which again accelerate creep. Confirming either of these hypotheses would need further investigation.

Surface and cross-sections studied with SEM revealed crack-like surface defects extending a few µm into the Cu-OFP material in specimens tested in air and in water without sulphide, but not in specimens tested in water with sulphides. This was explained by the rather thick sulphide film (about 10 µm) having consumed the Cu-OFP surface material in which the crack-like surface defects appeared in the specimens tested in air and water without sulphide. This may be taken as an indication that pre-existing µm-sized cracks are not able to initiate SCC in Cu-OFP in the presence of sulphides.

The main conclusion of the work is that the creep rate of Cu-OFP is affected by all three variables studied, i.e. anodic polarization, cathodic polarisation and sulphide exposure. However, the effects were found to be of transient type, lasting at maximum a few tens of hours.

Contents

1 Introduction

Phosphorus microalloyed copper (Cu-OFP) is proposed as the material for canisters providing the main corrosion protection in the system used to dispose of high-level nuclear waste in both Sweden and Finland. A few issues remain to be resolved, among them the influence of sulphide on the creep behavior of Cu-OFP.

Some earlier studies have indicated that anodic polarization can accelerate creep in copper. Revie and Uhlig (1974) studied oxide-free copper wires (dia 0.27 mm) immersed in deaerated acetate buffer of pH = 3.7 and in 0.01 M KCN with pH = 10.4 at 25 °C. They observed accelerated creep (by about a factor of 3) during anodic polarization at a current density of +0.9 mA/cm^2, and that the effect on creep rate was reversible, i.e. when the anodic polarization was switched off, the creep rate returned to the level before the anodic polarization. They also found that the effect of anodic polarization on creep rate becomes smaller when the thickness of the specimen is increased, which is to be expected for any surface related phenomena. Another finding of Revie and Uhlig was that cold deformation decreased the effect of anodic polarization markedly, roughly by a factor of 5.

Aaltonen et al. (2003) measured creep curves using a constant load of 180 MPa on pure copper specimens (0.4 × 9 mm cross-section and 25 mm gauge length) in 0.3 M $NaNO_2$ solution at temperatures of T = 20 to 80 °C. The specimens were intermittently anodically polarized by a current density of +1 mA/cm^2 in order to see the effect of oxidation/dissolution (and the resulting vacancy injection) on the creep rate. They observed that the anodic polarization enhanced the creep rate, roughly by a factor of 2, and that the effect was reversible. Aaltonen et al. proposed that the acceleration of creep was due to vacancies injected into the copper material during the anodic polarization, and that the same mechanism could be able to produce stress corrosion cracking (SCC) as well. It is worth noting here that the anodic current density of +1 mA/cm^2 corresponds to a corrosion rate of about 23 mm/y, which is several orders of magnitude higher than that expected in the repository conditions and thus not representative of any realistic repository conditions.

To our knowledge, there are no previous measurements of creep rate of Cu-OFP in presence of sulphide.

2 Goal

The goal of the work in the first phase was to study if the acceleration in creep rate of Cu-OFP due to anodic polarisation in $NaNO_2$-solution reported by Aaltonen et al. could be verified. The goal in the second stage was to study the effect of sulphide on the Cu-OFP creep rate, both with and without anodic or cathodic polarisation.

3 Description

The Cu-OFP material studied was delivered by SKB. The received material had approximate dimensions of 170 × 130 × 50 mm, cut from the tube T58. The material had been characterised and found to meet the requirements (Välimäki 2009). The average mechanical properties of nine samples representing different locations within the tube material are shown in Table 3-1. The average concentration of impurities is shown in Table 3-2.

Table 3-1. Average room temperature mechanical properties of the material (Välimäki 2009).

$Rp_{0.2}$ N/mm^2	R_m N/mm^2	Elongation %	Hardness HV5
42	212	52	43

Table 3-2. The average impurity concentration of the material (Välimäki 2009).

P ppm	S ppm	O ppm	H ppm
58.7	5.4	3.0	0.43

4 Methods

The Cu-OFP specimens had dimensions of 0.5 mm (thickness), 8 mm (width) and 29 mm (length of the deforming part of the body). The specimen design is shown in Figure 4-1.

After manufacturing of the specimen with spark eroding the mid part (0.5 mm thick) of the specimen was polished by hand with SiC papers up to #1200 grit, removing about 60 to 80 µm of the thickness. The specimens were attached to the loading grips of a tensile machine, electrically insulated from the grips by ZrO_2 parts. The loading part was attached to an autoclave lid and placed inside the autoclave body. All autoclave parts were made of AISI 316L stainless steel. The pull rod extended through the autoclave lid via a Ballseal™ spring loaded sealing element, with a friction force of 59 N at room temperature. The autoclave was equipped with a Ag/AgCl(0.05 M KCl) reference electrode and a Pt counter electrode. An Autolab PGSTAT302F potentiostat with Nova 2.0 software was used to measure and control the potential and current of the specimen. Tube pumps (Cole-Parmer Instrument Co.) were used to pump the electrolyte through the autoclave. The loading of the specimen was controlled by Cormet SSRT system v. 4.03. The pH was measured from grab samples using a Thermo Scientific Orion 5 Star pH-meter. The autoclave volume was 800 ml. The average feed rate of 5 ml/min thus gives a residence time of about 2.6 hours. Grab samples for sulphide analyses were taken as a rule from the outlet of the autoclave. In a few cases grab samples were taken from both inlet and outlet, resulting in the outlet value being about 15 to 20 % lower than that from the inlet.

A field emission gun – scanning electron microscope (FEG-SEM) Zeiss Crossbeam 540 equipped with solid-state four-quadrant backscatter detector and with an EDAX Octane energy-dispersive X-ray spectroscopy (SEM-EDS) detector was used to characterize the specimens.

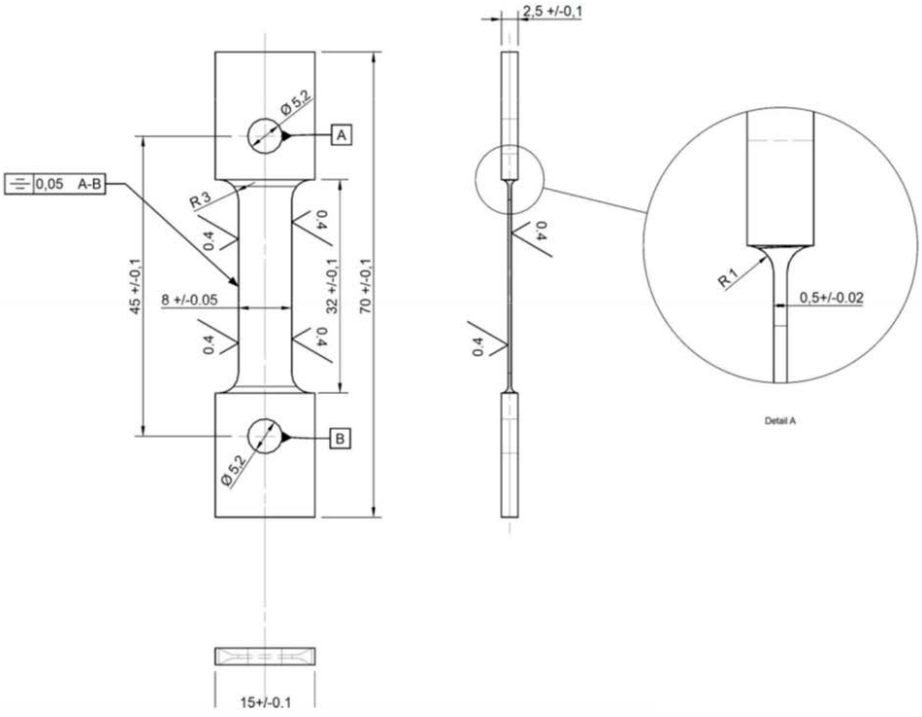

Figure 4-1. *Specimen design.*

The specimen surface and cross sections were analysed by SEM-secondary electron (SE) imaging and backscatter electron (BSE) imaging. SE imaging was performed with high voltage mode and low voltage mode at working distance (WD) of 10–15 mm. High voltage mode is with 15 keV, 1.5 nA, while low voltage mode is with 5 keV, 0.5 nA. High voltage mode is more sensitive to chemical composition difference while low voltage mode is more sensitive to surface layer topography. BSE are based on the dependence of the backscatter electron signal on the orientation of crystal lattice planes with respect to incident electron beam due to electron channelling. BSE images were acquired with the solid-state four-quadrant backscatter detector at 15 kV acceleration voltage with WD of 5–9 mm.

Inclusion and surface layer chemical analysis was performed with SEM-Energy Dispersive X-Ray (EDS) with 15 keV, 1.5 nA. For the sub-micrometer structures, to reduce the interaction volume of the incident electrons, EDS with 5 keV, 1.5 nA was applied.

Nanohardness was measured with Ultra Nanoindentation Tester, UNHT (manufacturer Anton Paar) with a Berkovich diamond tip. The measurements were performed to a constant depth of 200 nm with a deflection rate of 400 nm/min, and a holding time (at the maximum depth) of 60s.

The AFM studies were performed with Dimension 3100 AFM equipment (Digital Instruments). Analysis of the AFM results was performed using Gwyddion data analysis software (Nečas and Klapetek 2012).

5 Results

5.1 Creep tests

5.1.1 Test in 1M $NaNO_2$

Cu-OFP specimen was tested in 1M $NaNO_2$ solution at room temperature. The autoclave lid was left open, so that dissolved oxygen was constantly replenished from laboratory air. The pH of the solution was measured at 7.40 in the beginning and at 7.81 at the end of the test.

The stress and elongation are shown in Figure 5-1 as a function of time. Also marked are the times when electrochemical polarization was switched on. In the stress-time -curve small serrations can be seen. These are due to the loading machine correcting the load level back to the preset target value of 541 N (the friction load of 59 N has here already been deducted from the actual set value of 600 N). The correction span limits for this test were chosen as ±5 N (±1.25 N/mm^2).

From the elongation vs. time curve it is clear that the first anodic polarization (to +1 mA/cm^2 for 60 minutes) produced a dramatic (transient) increase in the elongation rate. The second anodic polarization (to +0.1 mA/cm^2 for 60 minutes) had almost no effect, while the cathodic reduction (to −0.447 V_{SHE} for 30 minutes) resulted again in a clearly higher (transient) elongation rate. It is noteworthy that the total elongation when the polarisations were performed, about 2 000 µm, corresponds to a total strain of about 7 %, and the elongation at the end, where the specimen failed and the load dropped to zero, corresponds to a strain of less than 10 %. This is very low in comparison to the normal room temperature fracture strain of Cu-OFP, i.e. 40 to 50 % (Kinnunen and Varis 2011).

Figure 5-2 shows the strain rate (1/s), as calculated from the elongation vs. time data shown in Figure 5-1, and the potential (V_{SHE}) as a function of time. The strain rate after reaching the target load level of 541 N (135 N/mm^2) decreased from about $\dot{\epsilon} = 1 \times 10^{-5}$ 1/s in the beginning (at about t = 210 min) to about $\dot{\epsilon} = 2 \times 10^{-8}$ 1/s (at about t = 1 300 min), during which period the potential remained at about E = +0.12 V_{SHE}. Anodic polarization to i = +1 mA/cm^2 resulted in an increase of the strain rate by roughly two orders of magnitude. Simultaneously, the potential increased immediately at the beginning of the polarization to about E = +0.38 V_{SHE}, and during the following about 30 minutes to a maximum of about E = +0.85 V_{SHE}, after which, during the last 30 minutes of the polarization the potential decreased to about E = +0.6 V_{SHE}. Anodic polarization to i = +0.1 mA/cm^2 at about t = 1 600 min did not affect the strain rate markedly, whereas cathodic polarization to −0.45 V_{SHE} for 30 min at about t = 1 700 min resulted in an increase of strain rate by about a factor of 5. The reason for the increase could be either hydrogen ingress into Cu-OFP or reductive dissolution of the existing surface film (both of which mechanisms are discussed further on within this report), or initiation of microcracks caused by SCC.

A detail of the data shown in Figure 5-2 of the period of anodic polarization to i = +1 mA/cm^2 is shown in Figure 5-3. The strain rate increases by roughly two orders of magnitude to above $\dot{\epsilon} = 1 \times 10^{-6}$ 1/s within ten minutes from the start of the anodic polarization. As the potential increases higher than about +0.6 V_{SHE}, the strain rate decreases reaching about $\dot{\epsilon} = 5 \times 10^{-7}$ 1/s, and when the potential again decreases towards +0.6 V_{SHE}, the strain rate increases back to a level above $\dot{\epsilon} = 1 \times 10^{-6}$ 1/s. This may be due to general corrosion blunting the cracks (assuming that already at this stage the strain rate is dominated by growth of SCC).

The fracture surface showed dominantly intergranular SCC (IGSCC, Figure 5-4), with some ductile mode of fracture (showing a few dimples) in the center part of the specimen failing at the end of the test period. The remaining open question is at which stage of the test the IGSCC has initiated. There are also some indications of transgranular SCC (TGSCC) taking place at the outer range of the fracture surface, before the fracture mode changes to IGSCC. Figure 5-5 shows the potentials during the experiment within the E-pH -diagram.

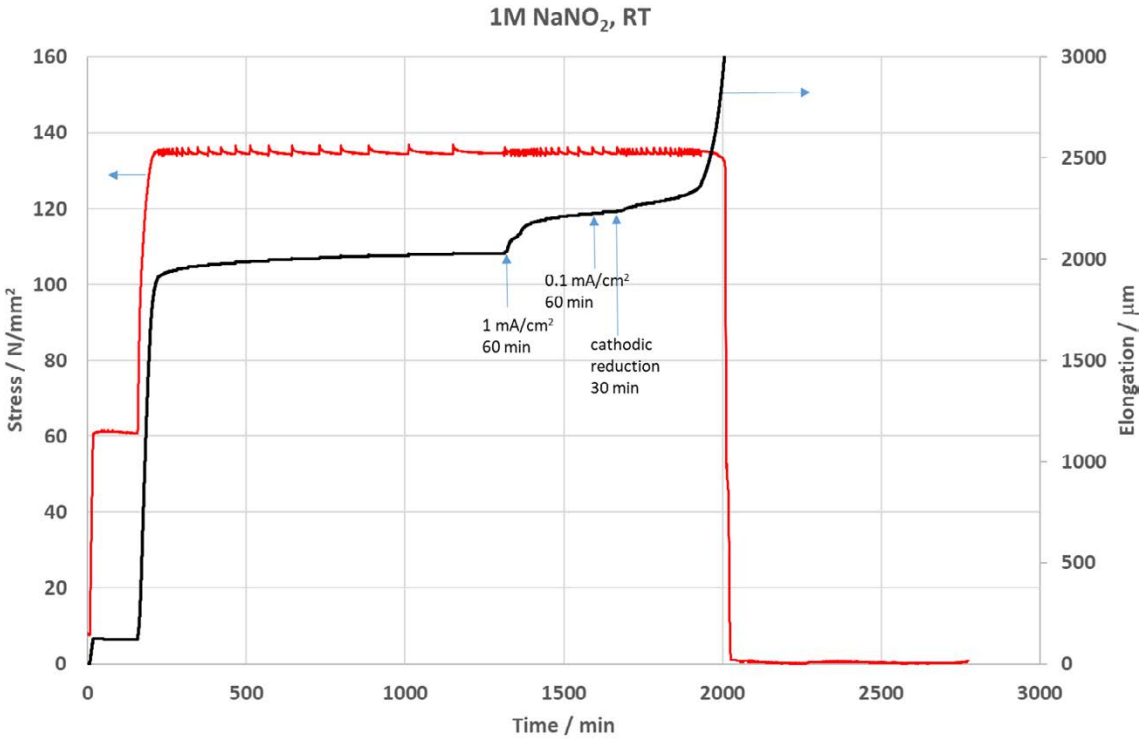

Figure 5-1. *Stress (N/mm²) and elongation (µm) as a function of time.*

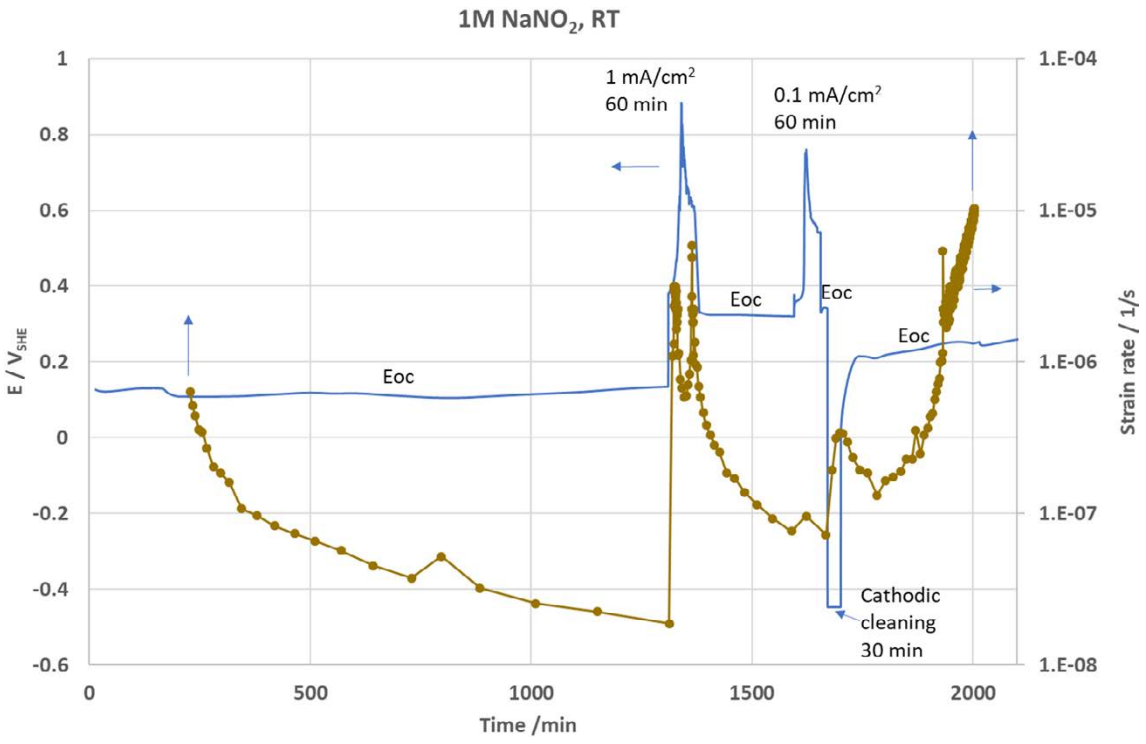

Figure 5-2. *Potential (E vs. SHE) and strain rate (1/s) as a function of time.*

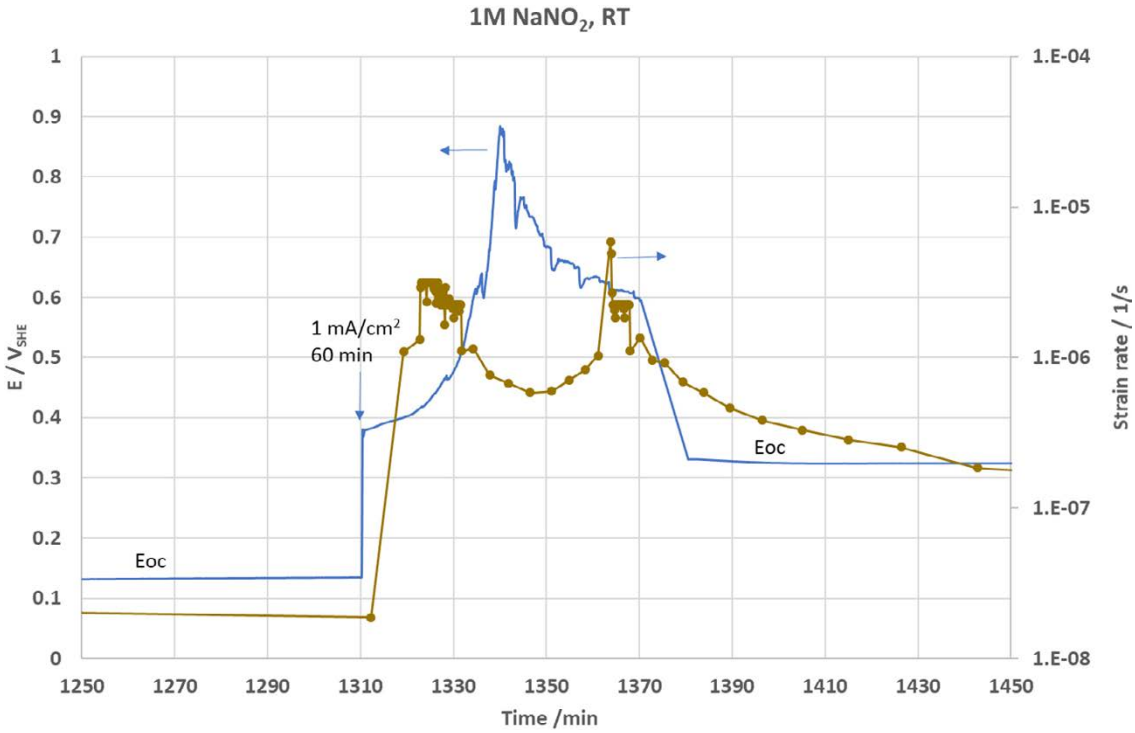

Figure 5-3. *Potential (E vs. SHE) and strain rate (1/s) as a function of time during the anodic polarization to i = +1 mA/cm² (detail of Figure 5-2).*

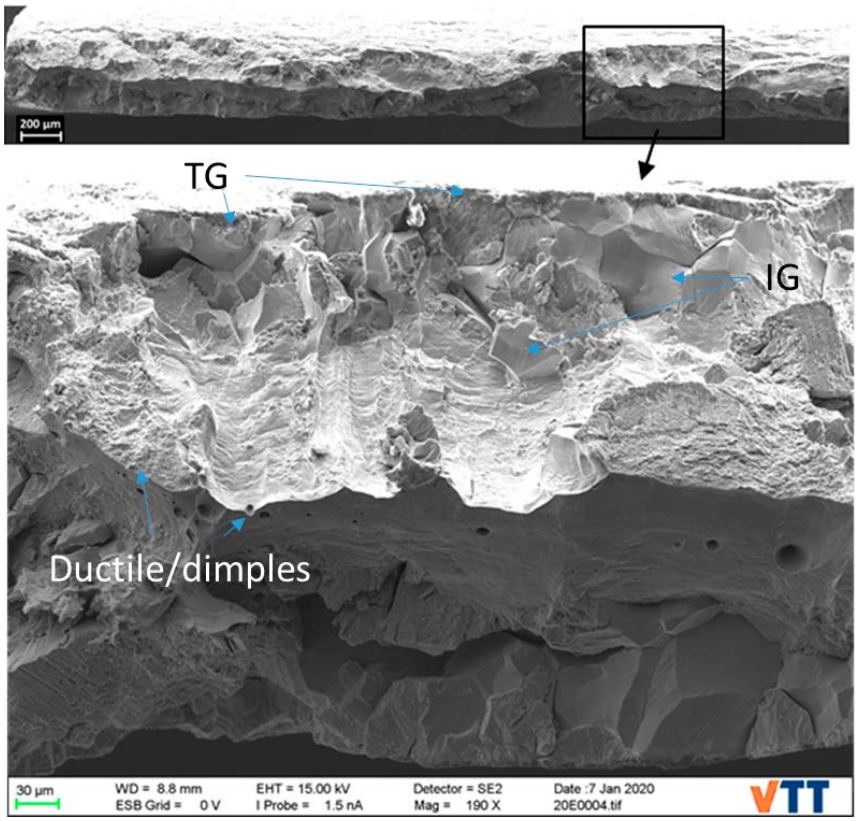

Figure 5-4. *The fracture surface of the specimen tested in 1M $NaNO_2$ at RT, transgranular SCC (TG), intergranular SCC (IG) showing open grain boundaries and some dimples in the centre (ductile fracture).*

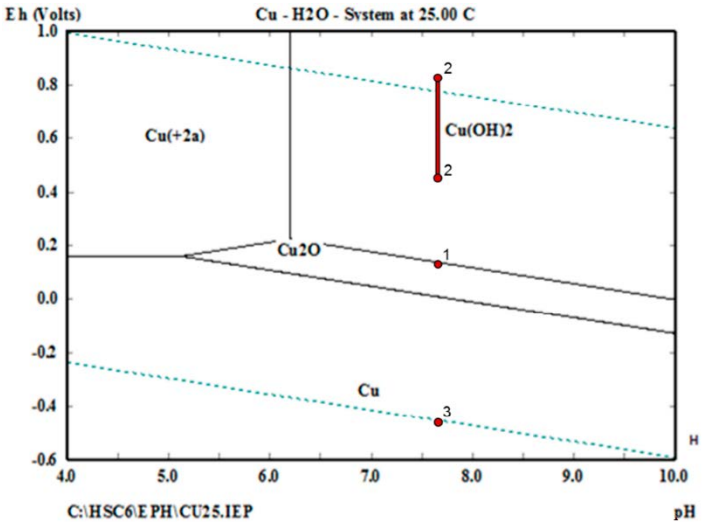

Figure 5-5. *Pourbaix-diagram of copper (10^{-6} M) at T = 25 °C. The red dot marked as 1 shows the corrosion potential of Cu-OFP during the initial loading and the following settling down of the strain rate (about 21 hrs wait). The red dots and the line between them marked as 2 shows the span of potential during the anodic polarization to i = +1 mA/cm². The red dot marked as 3 shows the potential during the cathodic polarization period (the lower blue line denotes the hydrogen line, i.e. the H_2/H^+ -equilibrium potential, below which water may dissociate producing hydrogen).*

Aaltonen et al. (2003) reported almost exactly the same corrosion potential before the onset of anodic polarization, i.e. E = −0.1 V_{SCE} (+0.14 V_{SHE}). As a result of the anodic polarization to i = 1 mA/cm² they reported an increase of the potential to about E = +0.1 V_{SCE} (+0.34 V_{SHE}), the increase taking place almost immediately and staying almost stable during the polarization. With regard to the strain rate, they reported a strain rate of about $\dot{\epsilon} = 1.1 \times 10^{-6}$ 1/s before the onset of anodic polarization, and an increase of strain rate to about $\dot{\epsilon} = 2.4 \times 10^{-6}$ 1/s due to the anodic polarization. The maximum strain rate achieved by Aaltonen et al. during the anodic polarization coincides rather well with that observed in the current study, whereas the strain rate just before the anodic polarization was much lower in the current study in comparison with that reported by Aaltonen et al. There were quite a few differences in the test parameters between the current test set and that adopted by Aaltonen et al. In their work, they studied Cu-OF (cold worked) instead of Cu-OFP and used 0.3 M $NaNO_2$ instead of 1 M $NaNO_2$. Maybe more importantly, they used a higher stress level, 180 N/mm², and after the initial loading waited only for about 1.5 hrs for the stabilization of the strain rate before the onset of anodic polarization. It is suggested that the main reason for a much lower strain rate before start of the anodic polarization in this work when compared to that found by Aaltonen et al. is the much longer time spent at the corrosion potential. The strain rate in the present test at about 1 300 minutes, i.e. just before starting the anodic potential was about 2×10^{-8} 1/s, about two orders of magnitude lower than that in the Aaltonen et al. work, while the maximum strain rate during the anodic polarization was roughly the same in both investigations.

5.1.2 Test 2 – target 10^{-4} M (phase 1) and 10^{-3} M (phase 2) HS^-

The experimental setup was the same as in Test 1 described above, except for the electrolyte. The experiment was performed in a 0.1 M phosphate buffer ($Na_2HPO_4 \times 2H_2O$ / $NaH_2PO_4 \times 2H_2O$) solution of pH = 7.2. It is worth noting here that according to the literature phosphate acts as an inhibitor for corrosion of copper in presence of sulphate (in alkaline pH range), forming highly insoluble Cu_3P. Since in this study no Cu_3P was found, it is likely that the buffer choice has only an insignificant effect to the results gained. In Phase 1, the sulphide addition was made at a concentration of 64 mg/l to a 10 l glass stock vessel filled with the buffer solution. Another 10 l glass stock vessel was filled with pure buffer solution. Each vessel was connected to a designated tube pump, with which the two flow rates could be controlled separately. The two silicon tubes were connected to AISI 316 tubing just before the autoclave, so that the flow reaching the autoclave had a controlled sulphide concentration. After flowing through the autoclave, the solution was directed to a 40 l storage tank where $FeCl_3 \times 6H_2O$ was used to neutralize sulphide. In Phase 2, the sulphide addition was made at

a concentration of 40 mg/l to a 10 l glass stock vessel filled with the buffer solution, and pumped through the autoclave without an additional pure buffer solution. The pH at the end of the experiment was measured at pH = 7.39.

Two methods were used to determine sulphide concentration from grab samples, Lange DR 2800 spectrophotometer with LCK 653-kit (0.1–2 mg/l) and Chemetrics C-9510D-kit for large concentrations (5–300 mg/L). The Lange DR 2800 shows values up to 3.5 mg/l and the Chemetrics can be used down to 2.5 mg/l with lesser accuracy, so the two methods offer some overlapping in the sulphide analysis.

Both the glass stock vessels were continuously purged with 5N N_2 (Aga Ltd) to keep oxygen out and to balance the pressure drop caused by the outgoing flow. At the pH used in this experiment, about 45 % of the sulphide is in the form of gaseous H_2S, Figure 5-6. Thus, due to the continuous bubbling gaseous H_2S was able to escape from the stock solution and the sulphide in the stock solution tended to diminish as a function of time (if a constant flow rate was maintained).

The stress and elongation of Phase 1 of the experiment are shown in Figure 5-7 as a function of time. Also marked are the times when electrochemical polarization was switched on. In the stress-time -curve small serrations can be seen. These are due to the loading machine correcting the load level back to the preset target value of 541 N (the friction load of 59 N has here already been deducted from the actual set value of 600 N). The correction span limits were chosen in this run as ±3 N (± 0.75 N/mm^2).

From the elongation vs. time curve in Figure 5-7 it is clear that the first anodic polarization (to 1 mA/cm^2 for 60 minutes) produced a clear increase in the elongation rate. The three further anodic polarizations (to 0.05 mA/cm^2 for 60 minutes) had no clear effect on the elongation rate.

The measured potential and calculated strain rate as well as the measured sulphide concentrations (Lange 2800) are shown in Figure 5-8 as a function of time. The sulphide concentration varied from 5×10^{-5} M (1.6 mg/l) to 9×10^{-5} M (3 mg/l) and was thus slightly below the target value of 10^{-4} M (3.2 mg/l). During the first anodic polarization (to 1 mA/cm^2 for 60 minutes), the strain rate increased from $\dot{\epsilon} = 5.7 \times 10^{-8}$ 1/s to a maximum of $\dot{\epsilon} = 2.7 \times 10^{-6}$ 1/s, i.e. by a factor of about 50. Simultaneously, the corrosion potential increased from E = −0.497 V_{SHE} to above E = +1.3 V_{SHE}, i.e. more than 0.5 V above the oxygen line (the potential above which water decomposes producing oxygen). According to the Pourbaix-diagram, Figure 5-9, in this area the stable surface film is $Cu(OH)_2$. Thus, it is very likely that $Cu(OH)_2$ was forming on the surface during the anodic polarization to +1 mA/cm^2 for 60 minutes. At the very high positive potential reached during the polarization to +1 mA/cm^2 several other sulphur containing species besides HS^- can form. Their possible contribution to the observed creep rate cannot be totally excluded. The sulphide analysis method used does not detect other sulphides than HS^-. However, presence of strong reducing agents, including thiosulfate and sulfite, may interfere with the measurement and result in a smaller measured value.

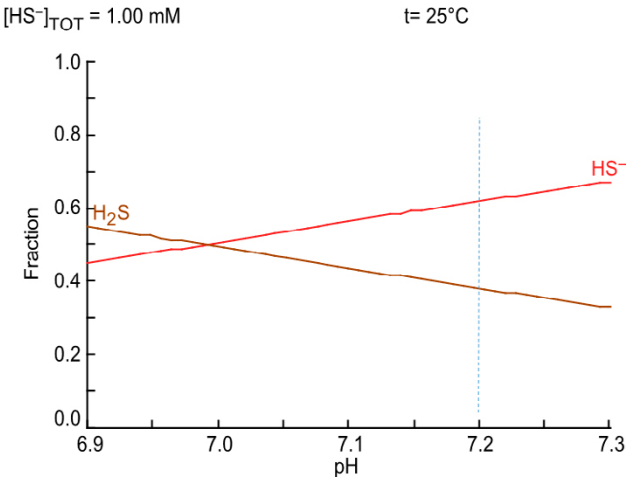

Figure 5-6. *Equilibrium speciation of H_2S/HS^- as a function of pH. The dotted blue line depicts the pH in the current experiment.*[1]

[1] Calculated by Christina Lilja 2020-06-23, with the Spana software, KTH, version 2020-Feb-05.

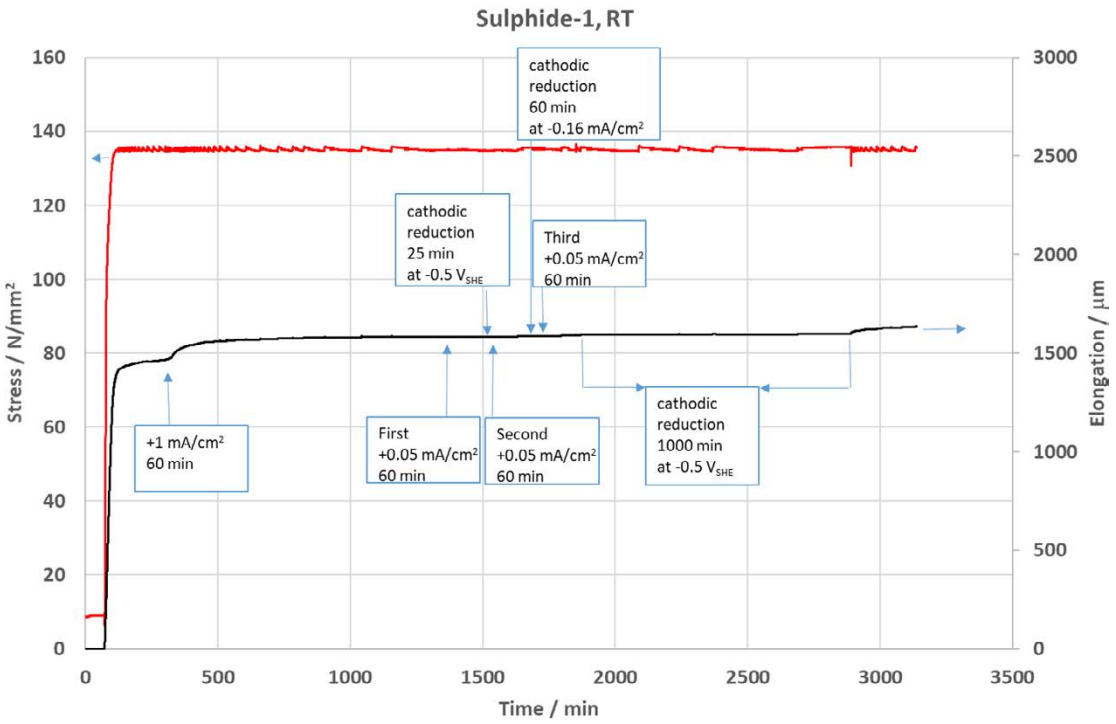

Figure 5-7. *Stress (N/mm²) and elongation (µm) as a function of time, Phase 1.*

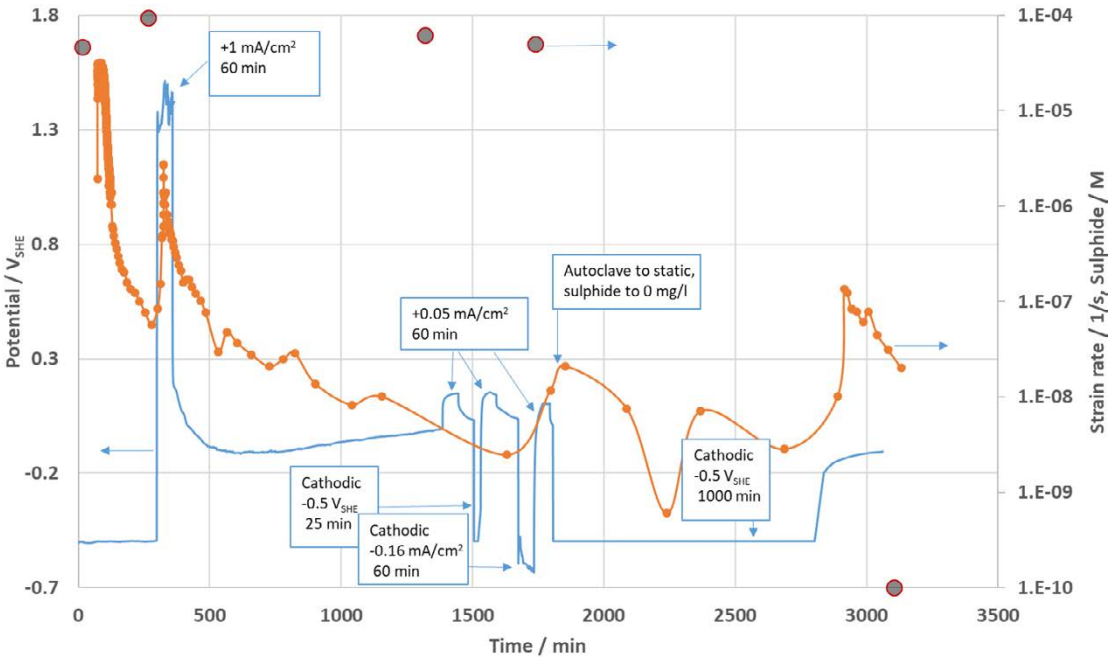

Figure 5-8. *Sulphide concentration (M, right axis), strain rate (1/s, right axis) and potential (V_{SHE}, left axis) as a function of time, Phase 1.*

Before the third anodic polarization to 0.05 mA/cm² for 60 minutes the specimen was subjected to a galvanostatic cathodic polarization to −0.16 mA/cm² for 60 minutes. After this treatment, the following anodic polarization to 0.05 mA/cm² for 60 minutes possibly resulted in a small increase in the strain rate (although at these very low strain rates the data points are too few to determine the range of normal scatter). If verifiable, the increase could also be due to the previous galvanostatic cathodic polarization. During the anodic polarizations to 0.05 mA/cm² for 60 minutes, the specimen potential increased to about E = +0.1 V_{SHE}, which is within the Cu_2O stability area at this pH (see the red dot numbered 3 in Figure 5-9). Since no increase in the strain rate was observed during these

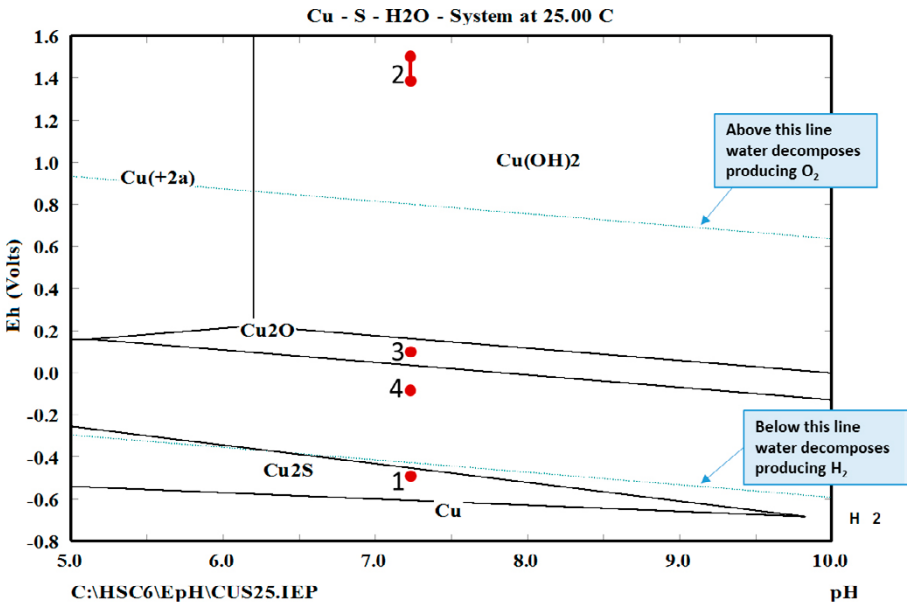

Figure 5-9. *Pourbaix-diagram of the Cu-S-H2O -system at T = 25 °C ([HS⁻] = 10^{-4} M, [Cu] = 10^{-6} M). The red dots depict the following stages: 1) corrosion potential at the beginning, 2) potential during the anodic polarization to +1 mA/cm² for 60 minutes, 3) potential during polarization to +0.05 mA/cm² for 60 minutes and 4) corrosion potential at the end (after a cathodic polarization for 1 000 min to −0.5 V_{SHE}).*

polarizations, it could be that the increase in the strain rate observed during the anodic polarization to 1 mA/cm² for 60 minutes is in fact related to the potential residing within the stability area of $Cu(OH)_2$, in line with the hypothesis by Aaltonen et al. that anodic dissolution results in vacancies being injected into the material, thus causing increase in strain rate.

After the third anodic polarization to +0.05 mA/cm² for 60 min, the autoclave was made static, i.e. the flow through the autoclave was stopped. The sulphide concentration was measured to be zero at about t = 3 100 min. In Figure 5-8, at the end of the data set, after keeping the specimen at the cathodic potential of E = −0.5 V_{SHE} for 1 000 min, when the polarization was terminated and the specimen was left at open circuit, the strain rate was observed to show a rapid increase followed by a slower decrease. During this time the corrosion potential reached a level of about E = −0.1 V_{SHE}, i.e. clearly within the stability area of metallic copper, Figure 5-9. Since there is likely no surface film formation process occurring at this potential, the increase in strain rate could be due to the extended cathodic polarization sequence.

The test was continued by Phase 2 as shown in Figure 5-10 and Figure 5-11. At about t = 7 100 min (while the autoclave was still in static mode and the sulphide concentration was zero) an anodic polarization to +1 mA/cm² was made for 60 min, resulting in an increase in the measured elongation rate, Figure 5-10, the calculated strain rate, Figure 5-11, as well as in an increase of the potential to a maximum of about +1.8 V_{SHE}, Figure 5-11.

At about t = 8 400 min, the autoclave was once more connected to the flow with a measured sulphide concentration varying between $[HS^-]$ = 20 to 25 mg/l (0.63×10^{-3} to 0.78×10^{-3} M). The potential shows an immediate decreasing trend, as expected, Figure 5-11. The addition of sulphide seems to result in a small decrease of the strain rate, although due to scatter and the previous similar trend this is speculative.

After proper settling time, three consecutive anodic polarizations were performed, to +0.05 mA/cm² for 60 min, to +0.1 mA/cm² for 60 min and to +1 mA/cm² for 60 min. None of these polarisations resulted in a noticeable change in the strain rate, although they of course had a clear effect on the potential, Figure 5-11. The maximum potentials achieved during the anodic polarizations to +1 mA/cm² for 60 min with $[HS^-]$ = 0 mg/l and $[HS^-] \approx$ 25 mg/l are shown in Figure 5-12 as red dots numbered 1 and 2, respectively. They are both well into the stability area of $Cu(OH)_2$. The anodic polarization to +1 mA/cm² for 60 min with $[HS^-]$ = 0 mg/l produced a marked increase in the strain rate, while that with $[HS^-] \approx$ 25 mg/l produced no noticeable increase in the strain rate, as shown in Figure 5-11.

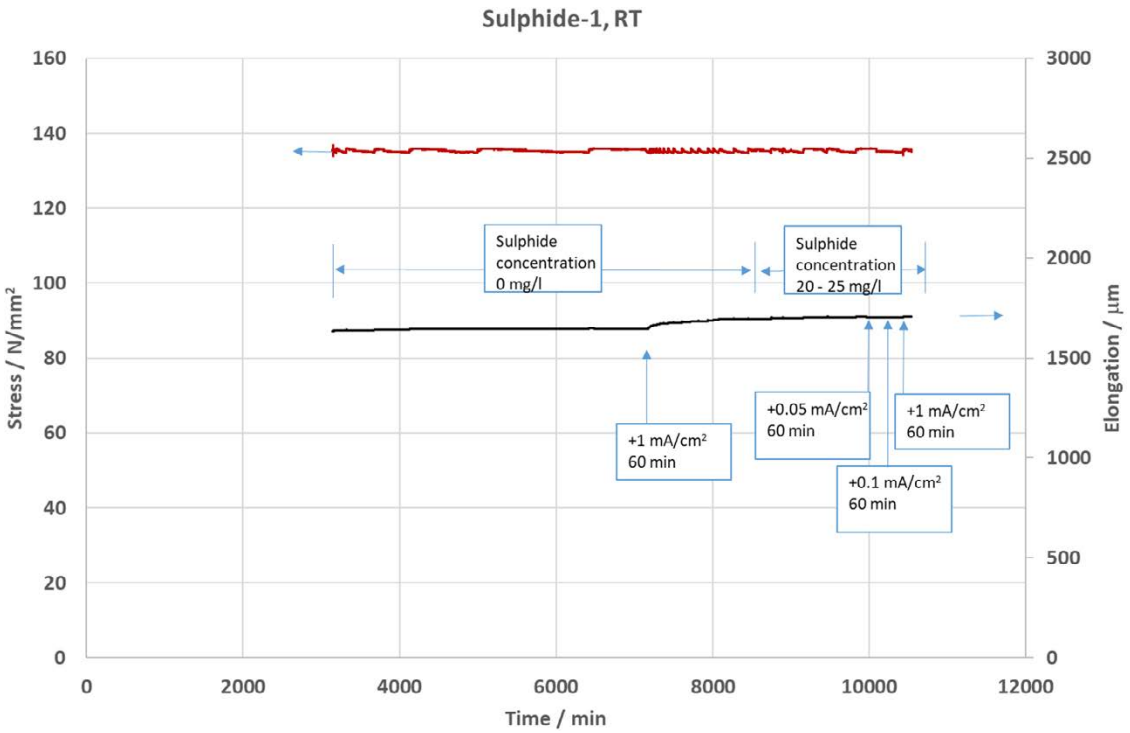

Figure 5-10. *Stress (N/mm²) and elongation (µm) as a function of time, phase 2.*

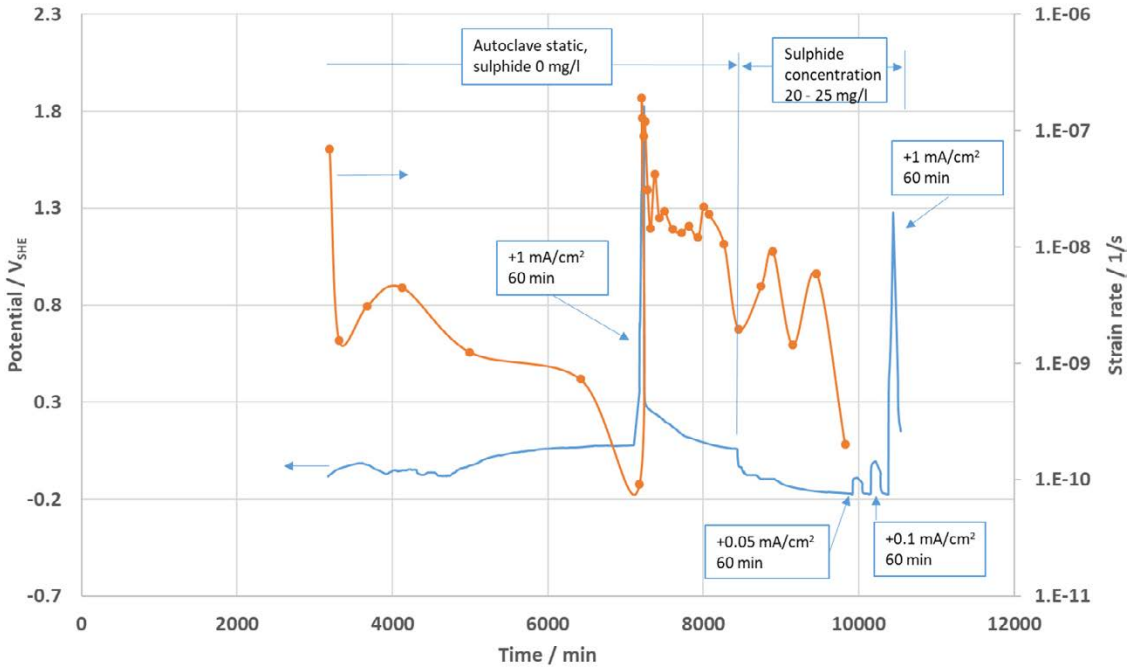

Figure 5-11. *Strain rate (1/s, right axis) and potential (V_{SHE}, left axis) as a function of time, phase 2. The dashed line depicts the strain rate not changing due to the three last anodic polarizations.*

The two anodic polarization sequences are, however, not completely comparable, since at the start of the second anodic polarization there might still be some remnants of the surface film formed during the first anodic polarization (i.e. a mixture of oxide and sulphide).The maximum potential achieved during the anodic polarizations to +0.05 mA/cm^2 for 60 min with [HS$^-$] ≈ 25 mg/l (the red dot numbered 3 in Figure 5-12), resides clearly within the stability are of copper. In this case, no noticeable increase in the strain rate was observed, Figure 5-11, as was also the case for the lower sulphide concentration of about 2.5 mg/l (7.8×10^{-4} M) for the same current density, Figure 5-8.

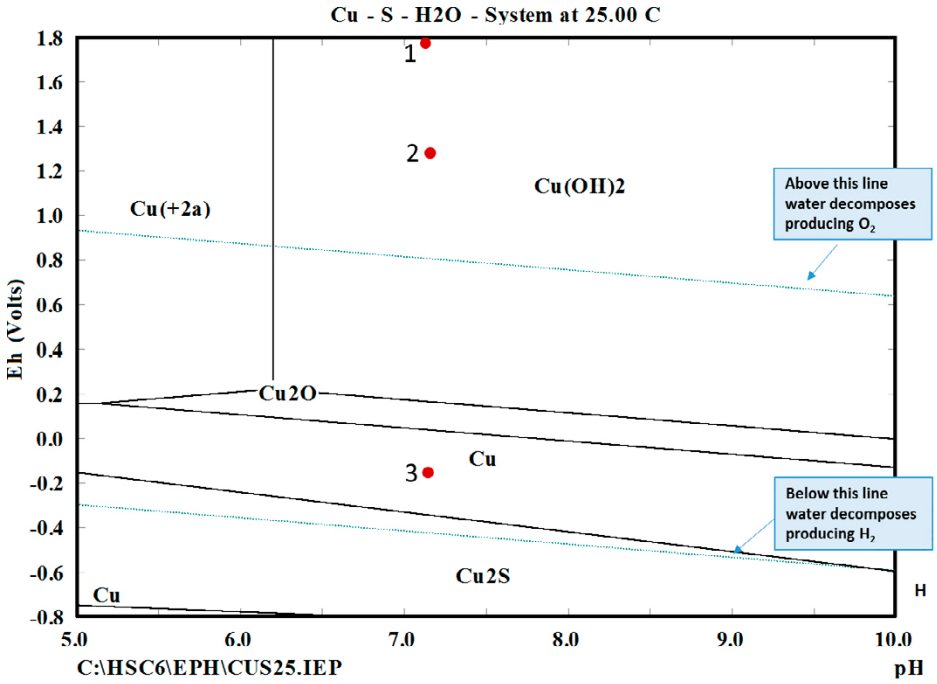

Figure 5-12. *Pourbaix-diagram of the Cu-S-H2O -system at T = 25 °C ([HS⁻] = 10^{-3} M). The red dots depict the following stages: 1) potential during the anodic polarization to +1 mA/cm² for 60 minutes with [HS⁻] = 0 mg/l, 2) potential during polarization to +1 mA/cm² for 60 minutes with [HS⁻] ≈ 25 mg/l, 3) potential during polarization to +0.05 mA/cm² for 60 minutes with [HS⁻] ≈ 25 mg/l.*

Figure 5-13 shows the maximum potential achieved during the anodic polarizations as a function of the sulphide concentration. It seems that increasing sulphide concentration decreases the maximum potential, i.e. sulphide seems to act as a "chemical potentiostat" able to counteract the effect of polarization by external means. This could be interpreted as part of the applied anodic current being spent in reactions within the electrolyte instead of reactions of the copper surface. It would appear that in the present study, applying the anodic polarization to +1 mA/cm² results in an increase of the potential to such high levels that they do not represent any relevant case of the copper canisters.

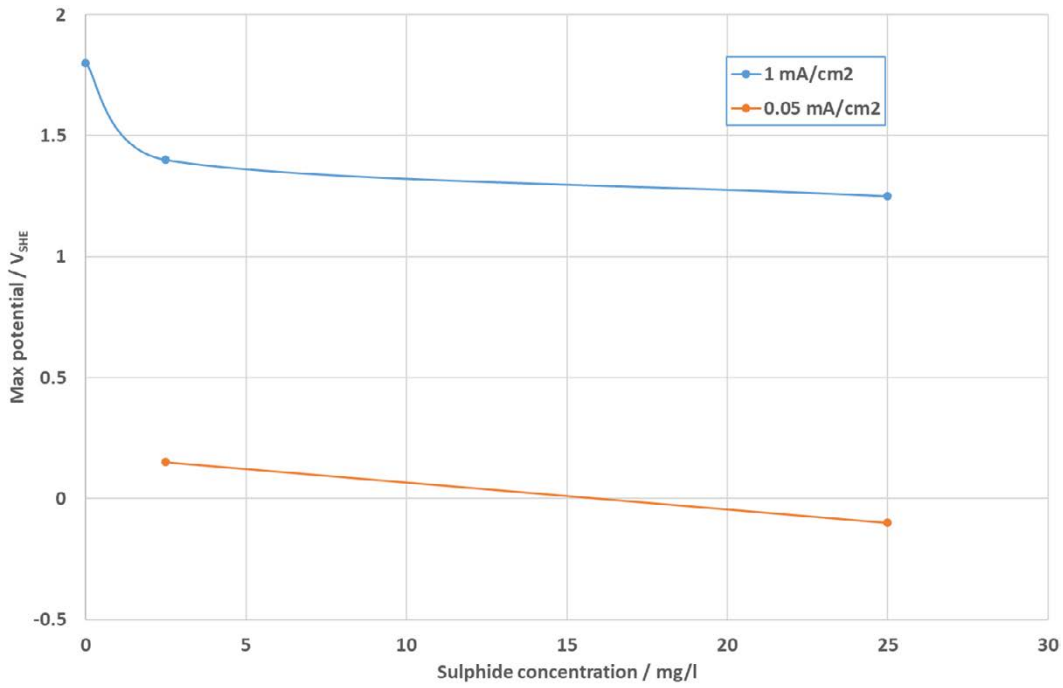

Figure 5-13. *Maximum potential achieved during the anodic polarizations as a function of the sulphide concentration.*

5.1.3 Test 3 – target 10^{-3} M HS^-

The experimental setup was the same as in Test 2 described above. This test was directed at studying the direct effect of 10^{-3} M HS^- on the creep rate of Cu-OFP, without any previous polarisations, and to verify the effect of anodic polarisation to i = 1 mA/cm^2 for 60 minutes on the creep rate. The pH at the end of the experiment was measured at pH = 7.38.

The stress and elongation of the experiment are shown in Figure 5-14 as a function of time. Also marked are the times when sulphide feed was set on and when the electrochemical polarization was switched on. The sulphide concentrations shown in the figure as inserts (25 and 0 mg/l) were measured using the Chemetrics C-9510D-kit. In the stress-time -curve small serrations can be seen. These are due to the loading machine correcting the load level back to the preset target value of 541 N (the friction load of 59 N has here already been deducted from the actual set value of 600 N). The correction span limits were chosen in this run as ±3 N (±0.75 N/mm^2).

The elongation vs. time curve in Figure 5-14 shows clearly that the anodic polarization (to 1 mA/cm^2 for 60 minutes) produced a small increase in the elongation rate. On the other hand, stopping of the sulphide feed resulted in a much larger and continuous increase in the elongation rate.

The measured potential and calculated strain rate as well as the measured sulphide concentrations are shown in Figure 5-15 as a function of time. A detail of Figure 5-15 focusing on the period of the anodic polarization is shown in Figure 5-16. The sulphide concentration during the feed was measured at 7.8×10^{-4} M (25 mg/l) and was thus slightly below the target value of 10^{-3} M (32 mg/l).

During the first period (0 to 1 600 minutes), while the specimen was exposed to the buffer solution (static, no flow, nitrogen bubbling through the autoclave) without sulphide, the potential varied between −0.35 and −0.47 V_{SHE}, which was slightly higher than the value of about −0.50 V_{SHE} during the previous test (Figure 5-8, first 300 minutes). The specimen was loaded to 541 N at about t = 1 150 minutes, after which the strain rate was let to stabilize, resulting in a strain rate of about $\dot{\epsilon} \approx 5 \times 10^{-8}$ 1/s, very close to the value found in the previous run at this stage (Figure 5-8, t ≈ 300 minutes). Start of the sulphide feed resulted in a marked decrease of the strain rate, to a level of $\dot{\epsilon} \approx 4 \times 10^{-10}$ 1/s. The effect of sulphide in decreasing the strain rate is clear, although one could argue that the strain rate had not yet fully stabilized when the sulphide feed was started, and thus not the whole observed decrease (two orders of magnitude) could be attributed solely to the effect of sulphide. Start of the sulphide feed resulted in a decrease of the potential to the level of E = −0.55 V_{SHE} (note that in the time interval between t = 1 530 to 2 510 minutes the potential monitoring data was lost, and the value stated is based on the data measured for a period of 15 minutes before the onset of the anodic polarization).

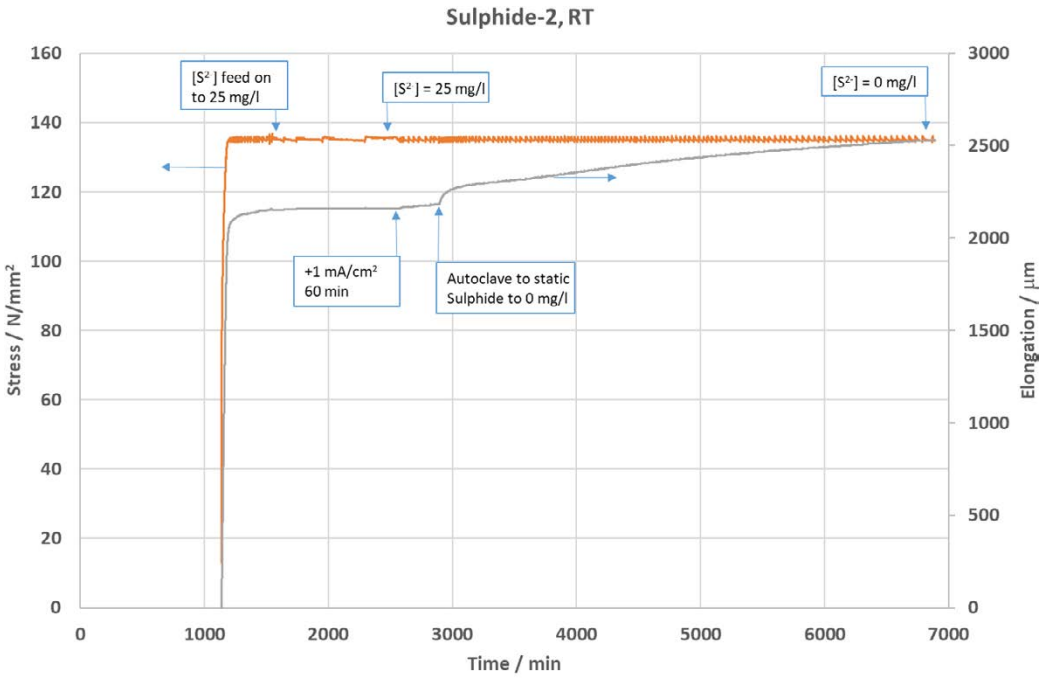

Figure 5-14. *Stress (N/mm^2) and elongation (µm) as a function of time.*

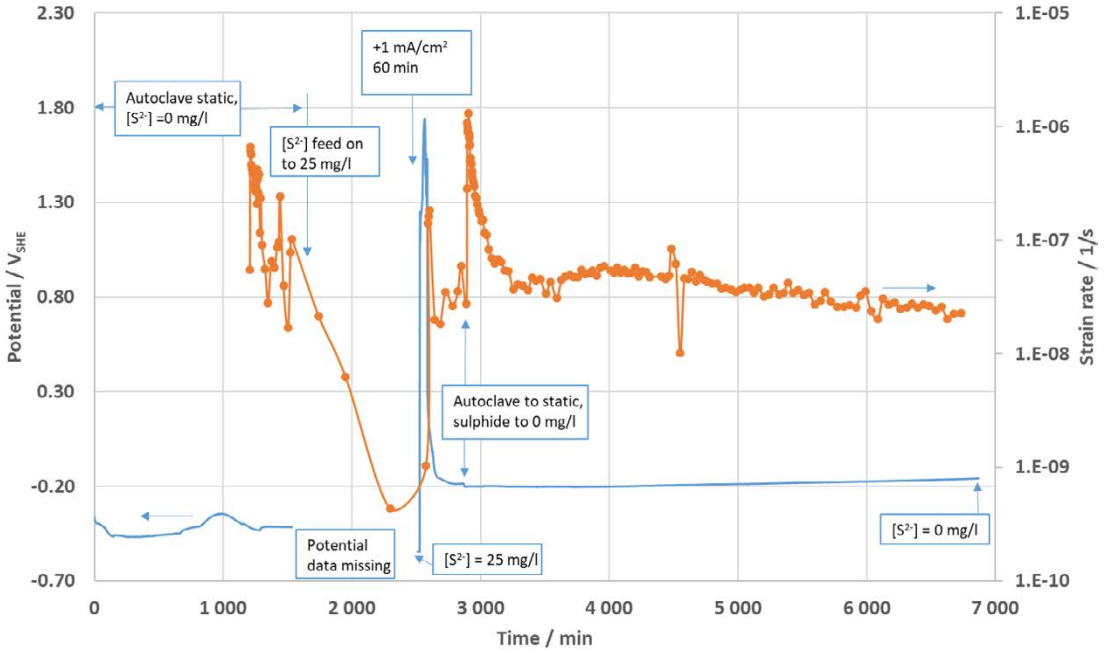

Figure 5-15. *Strain rate (1/s, right axis) and potential (V_{SHE}, left axis) as a function of time.*

Starting at t = 2 526 minutes, anodic polarization to i = 1 mA/cm^2 for 60 minutes was performed. During this period the potential increased to a very high level between E = +1.3 and +1.7 V_{SHE}, and the strain rate increased achieving a maximum of $\dot{\epsilon} \approx 2 \times 10^{-7}$ 1/s, Figure 5-15 and Figure 5-16. After the anodic polarization was terminated the potential rapidly decreased to a level of E = −0.19 V_{SHE}, and the strain rate decreased to a level of $\dot{\epsilon} \approx 2{-}3 \times 10^{-8}$ 1/s. At t = 2 870 minutes the sulphide feed was turned off, the autoclave was returned to static condition (no flow) and nitrogen bubbling through the autoclave was started again. The potential remained unchanged, while the strain rate increased very rapidly to a maximum of $\dot{\epsilon} \approx 1 \times 10^{-6}$ 1/s. During the final period of the test, lasting for about 4 000 minutes, the strain rate stabilized to a level of about $\dot{\epsilon} \approx 2{-}4 \times 10^{-8}$ 1/s, while the potential was almost stable, reaching a level of E = −0.16 V_{SHE} at the end of the test.

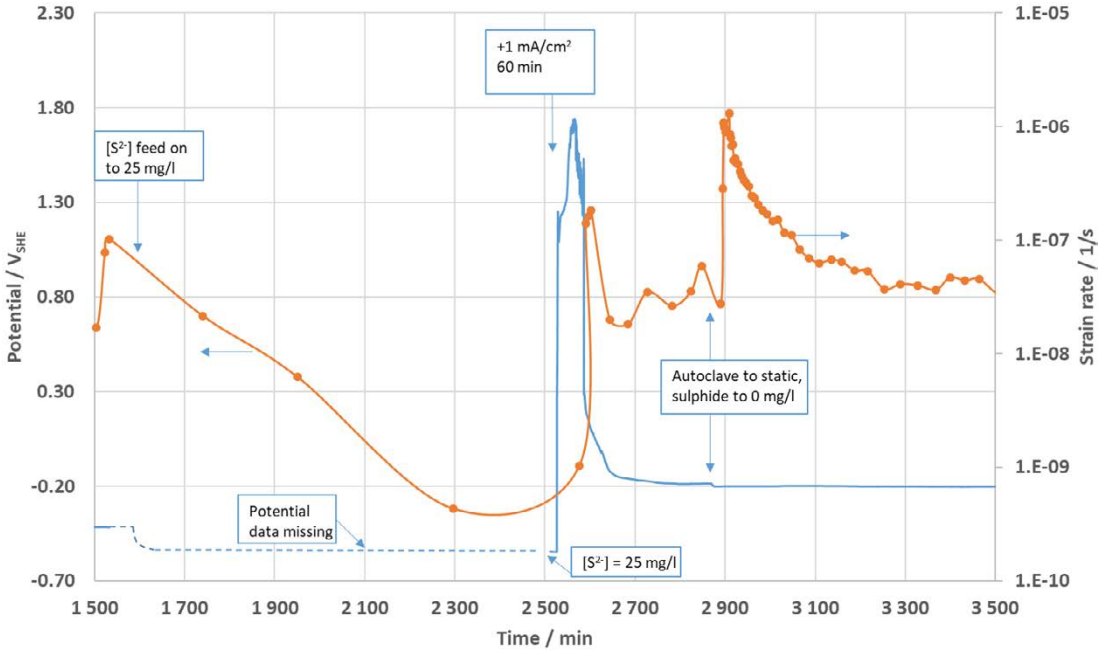

Figure 5-16. *Potential (E vs. SHE) and strain rate (1/s) as a function of time during the anodic polarization to i = 1 mA/cm^2 (detail of Figure 5-15).*

According to the Pourbaix-diagram, Figure 5-17, at the beginning (stage 0) of the test without sulphide (static, no flow, nitrogen bubbling through the autoclave), the corrosion potential was close to the hydrogen line, indicating the absence of oxygen. At stage 1, during the sulphide feed without polarization, the corrosion potential was clearly within the stability area of Cu_2S. At stage 2, during the anodic polarization to 1 mA/cm^2 for 60 minutes, the potential was very high in the area where the stable surface film is $Cu(OH)_2$. After switching off the anodic polarization, in stage 3, the corrosion potential did not return to the level of about E = −0.55 V_{SHE} characteristic of the sulphide level [HS^-] = 25 mg/l despite the continued sulphide feed, but remained at a higher level of about E = −0.19 V_{SHE} where metallic copper is the stable phase. Since during the final period of the test the corrosion potential remained within the stability area of metallic copper, the continuing creep is supposed to be related to purely mechanical phenomena, i.e. not to anodic dissolution. One could argue that the $Cu(OH)_2$ film formed during the previous anodic polarization should be slowly reducing at this stage, which might also contribute to the creep rate possibly through the reductive dissolution mechanism (dissolution introducing vacancies into the material). The reductive dissolution of a transition metal oxide occurs when dissolution is coupled to a redox event. The effects of redox processes are due predominantly to the variation of metal solubility with oxidation state. An example of such a process is e.g. the reductive dissolution of Fe(III) hydroxides by H_2S (dos Santos Afonso and Stumm 1992).

To study the possibility that the continuing creep during the final stage of the test would be caused by SCC microcracks initiated during the previous anodic polarization stage, the test was terminated and the specimen surface investigated with SEM. A number of line shaped openings were found, Figure 5-18 (a to d). The size of these correspond rather well with the grain size (≈100 µm) of the Cu-OFP material (Välimäki 2009). The inclination of the lines is often close to 45° to the tensile axis, and other inclinations also appear. These openings could be due to plastic deformation of the underlying Cu-OFP grains (slip planes) causing the surface film to break, or actual micro-cracks in the Cu-OFP material.

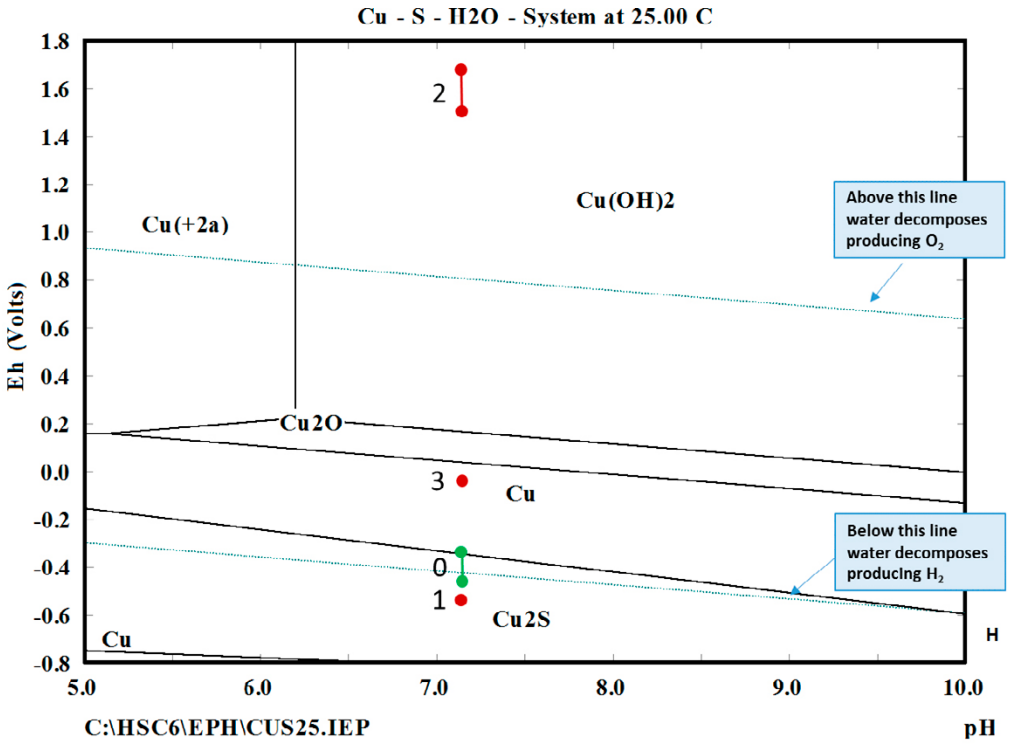

Figure 5-17. *Pourbaix-diagram of the Cu-S-H2O -system at T = 25 °C ([HS^-] = 10^{-3} M). The green dots (0 stage) show the potential at the beginning of the test, before the sulphide feed was turned on. The red dots depict the following stages: 1) corrosion potential during the sulphide feed, 2) potential during the anodic polarization to +1 mA/cm^2 for 60 minutes and 3) corrosion potential at the final stage (no flow, [HS^-] = 0 mg/l).*

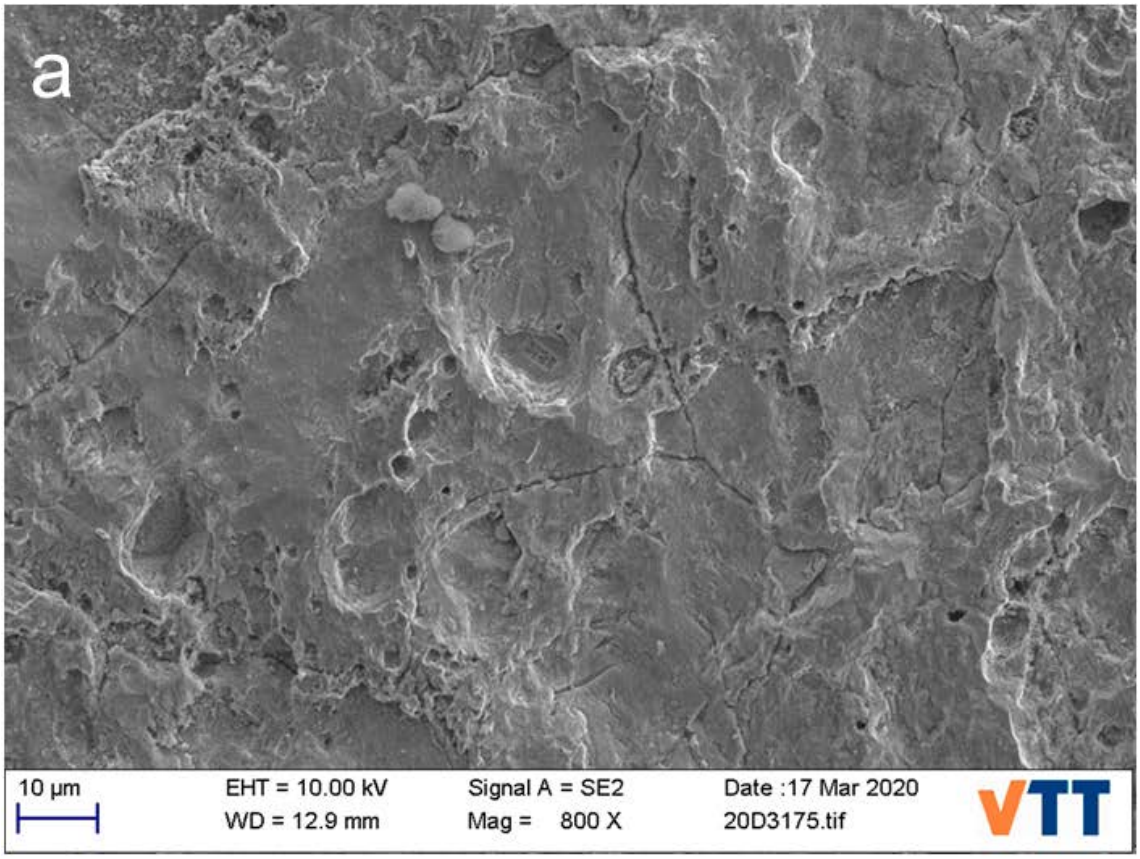

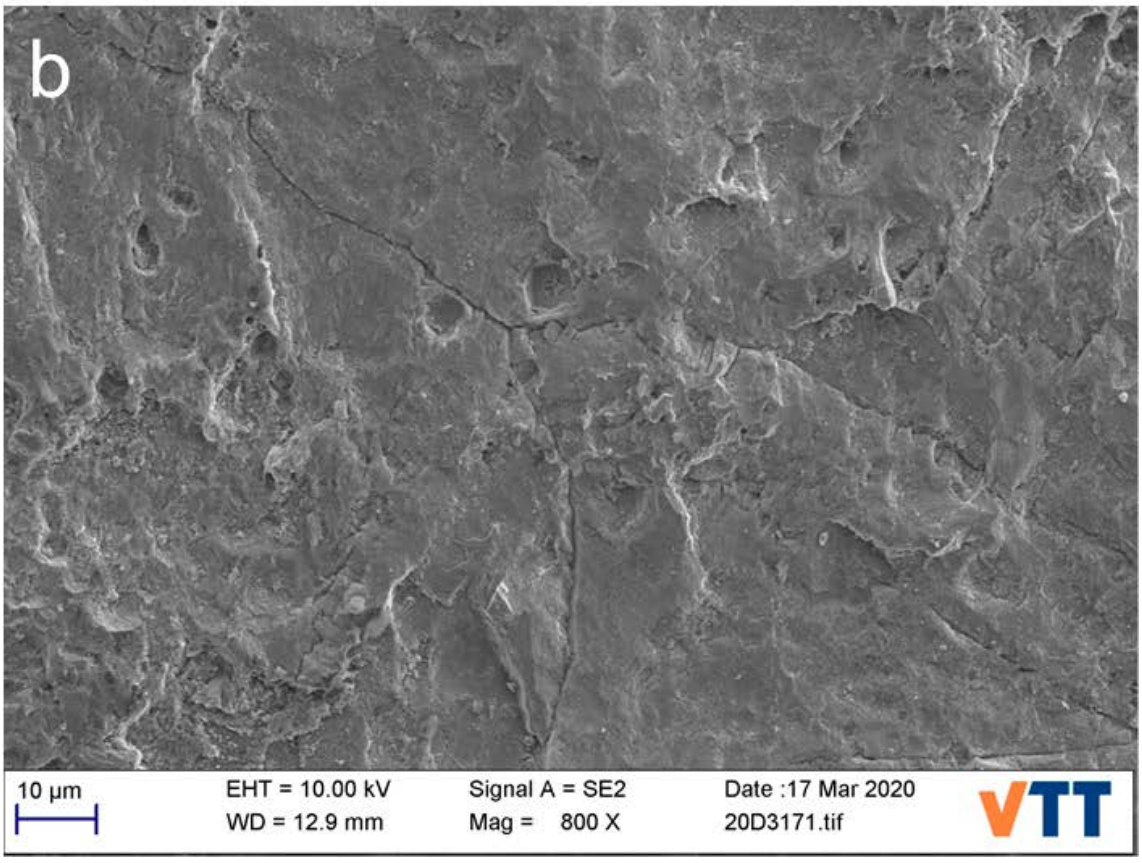

Figure 5-18. *SEM -pictures (a to d) of the specimen in Test 3 (25 mg/l sulphide). Here, the direction of tensile stress is vertical.*

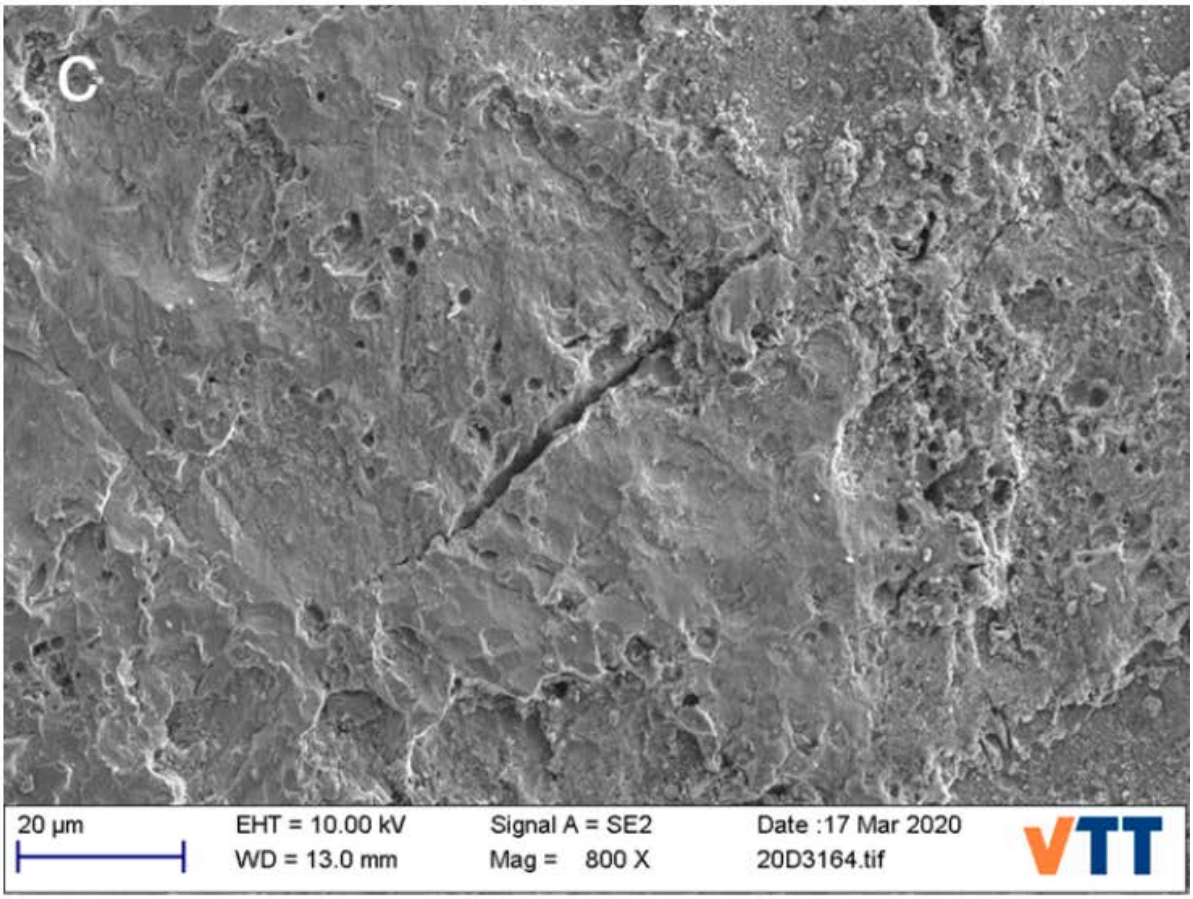

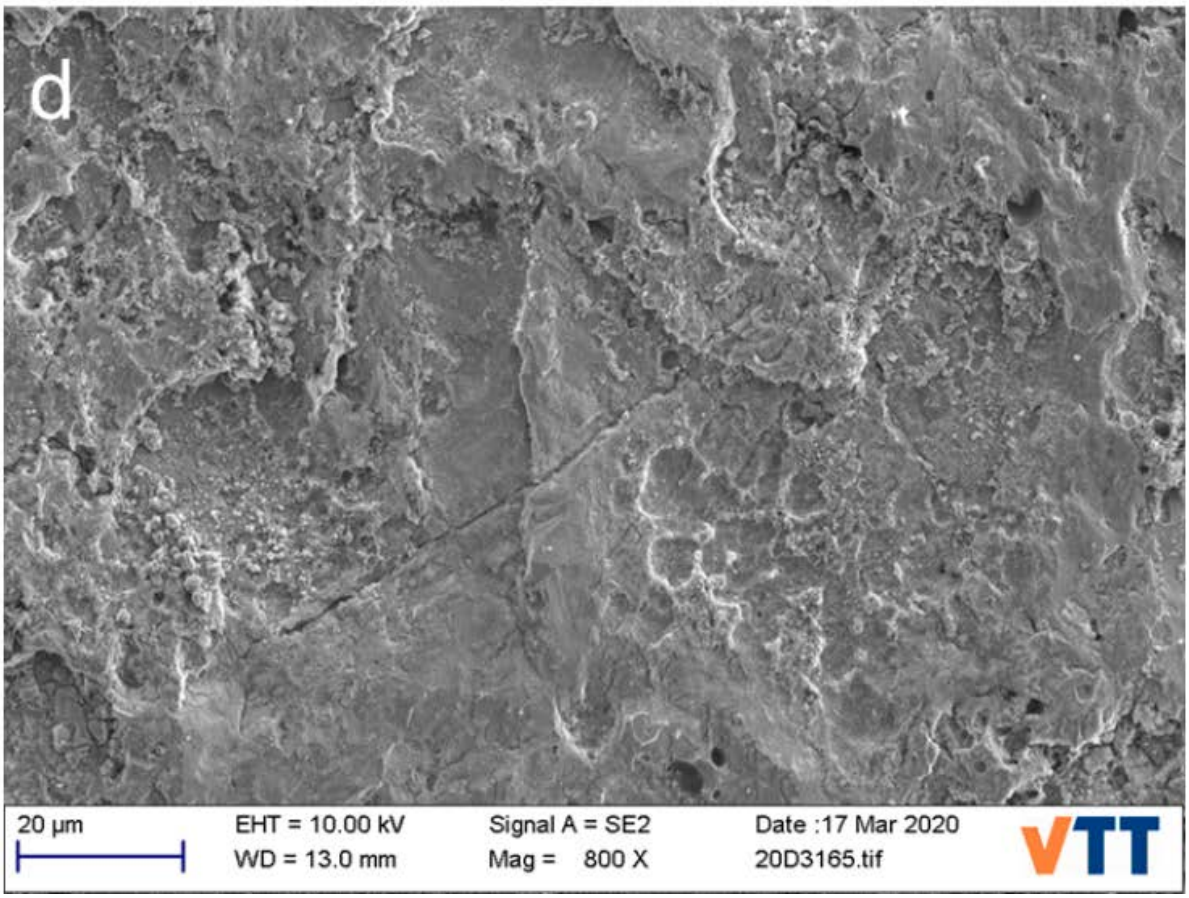

Figure 5-18. *Continued.*

5.1.4 Test 4 – strain rate in air and in water with target 10^{-3} M HS^-

The first part of the test was to measure the strain rate in air at room temperature, since that data was not available in the literature. This part was performed with two different test set ups, first with a standard conventional creep testing equipment (dead load) with a specimen geometry of square cross-section ($8.9 \times 8.9 = 79.2$ mm^2, l = 50 mm, material source Posiva plates X579-581). The specimen was manufactured using spark erosion to avoid deformation of the surface layers. The second test set up was the same that was used in the other tests in water (Figure 1). The result from this latter test in air is shown in Figure 5-19 and Figure 5-20. A comparison of the strain rates as a function of time in all the performed tests is shown in Figure 5-21. For the tests in water, the strain rates in Figure 5-21 represent the first part, during which no sulphide was present and no polarisation sequences were performed. In the standard creep test in air, the data sampling rate was 1/h, whereas in the other tests it was 1/10s. This may explain the larger scatter in the other tests (no data smoothing) when compared with the standard test. Based on these results one can argue that the specimen geometry used in this work gives reliable creep data.

After the strain rate measurement in air, the specimen load was reduced to 100 N (from 600 N), the autoclave was filled with the pH = 7.2 buffer solution, the loading system was placed inside the autoclave, the autoclave lid was tightened and nitrogen bubbling through the autoclave was started to remove dissolved oxygen from the water. Monitoring of the potential was started about 14 minutes after starting the nitrogen bubbling and continued for 54 hours, until start of the sulphide feed through the autoclave. The stress and elongation of the experiment are shown in Figure 5-22 and the potential and strain rate in Figure 5-23, as a function of time. Also shown are the measured sulphide concentrations (as mg/l in Figure 5-22 and as M in Figure 5-23).

It is worth noticing that the dependence of the strain rate on time during the first part of the test (before start of the sulphide feed) is almost identical to the previous test in air with the same specimen (Figure 5-21). The only change made was the unload/reload cycle, i.e. the load was reduced to 100 N before placing the loading system inside the autoclave and increased back to 600 N after stabilization of the specimen potential. This is a known phenomenon (Mannesson and Andersson-Östling 2016), and is suspected to result from dislocation re-arrangement due to the change in the loading.

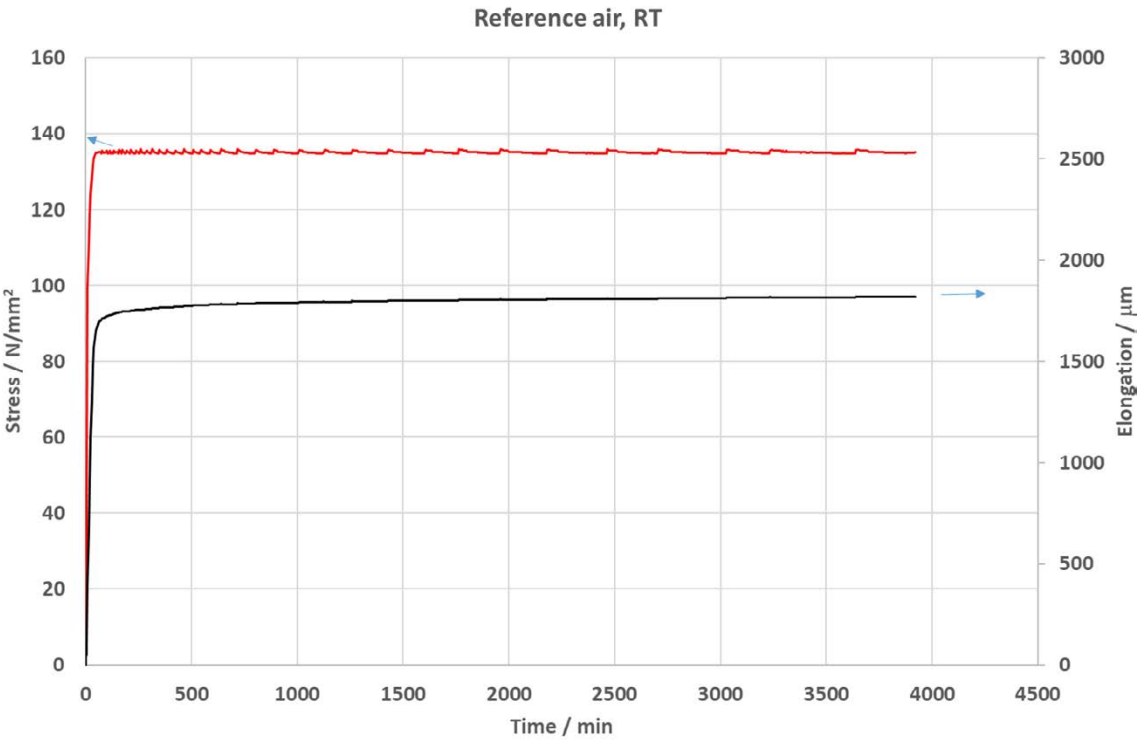

Figure 5-19. *Stress (N/mm^2) and elongation (µm) as a function of time, reference test in air with the specimen geometry shown in Figure 1.*

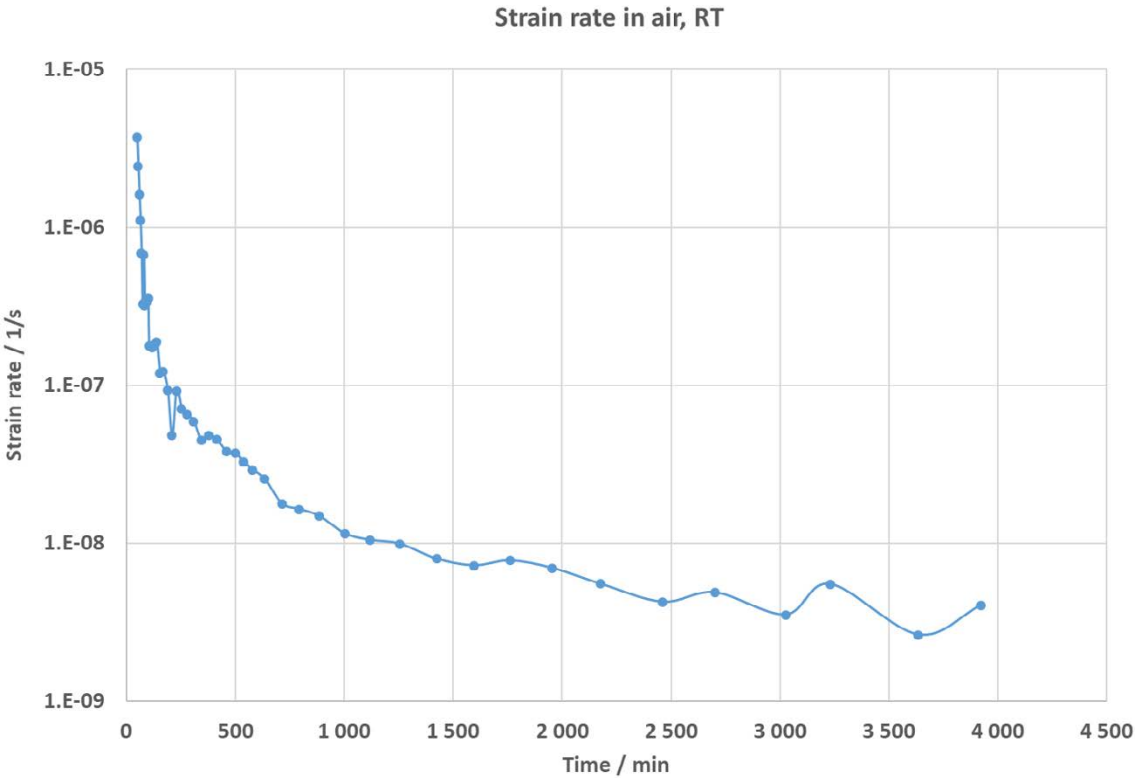

Figure 5-20. *Strain rate (1/s) as a function of time, reference test in air with the specimen geometry shown in Figure 1.*

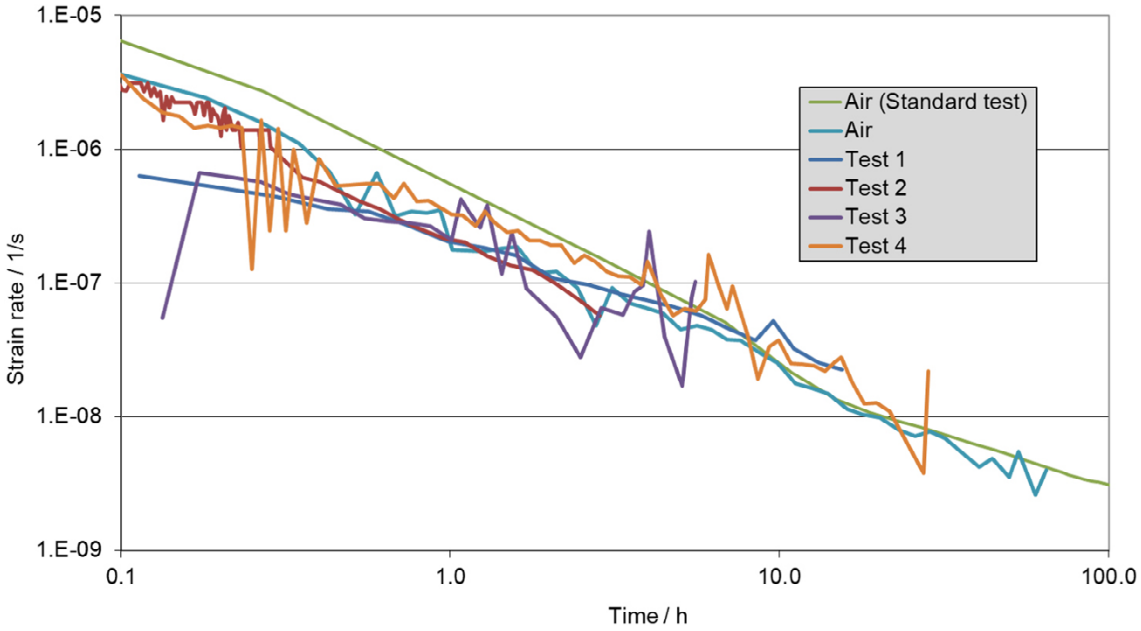

Figure 5-21. *Comparison of strain rates from standard test in air, air test with the specimen geometry shown in Figure 1 and strain rates in water (the first parts of the tests, during which no sulphide was present and no polarisation sequences were performed). Note that here the x-axis is in log scale.*

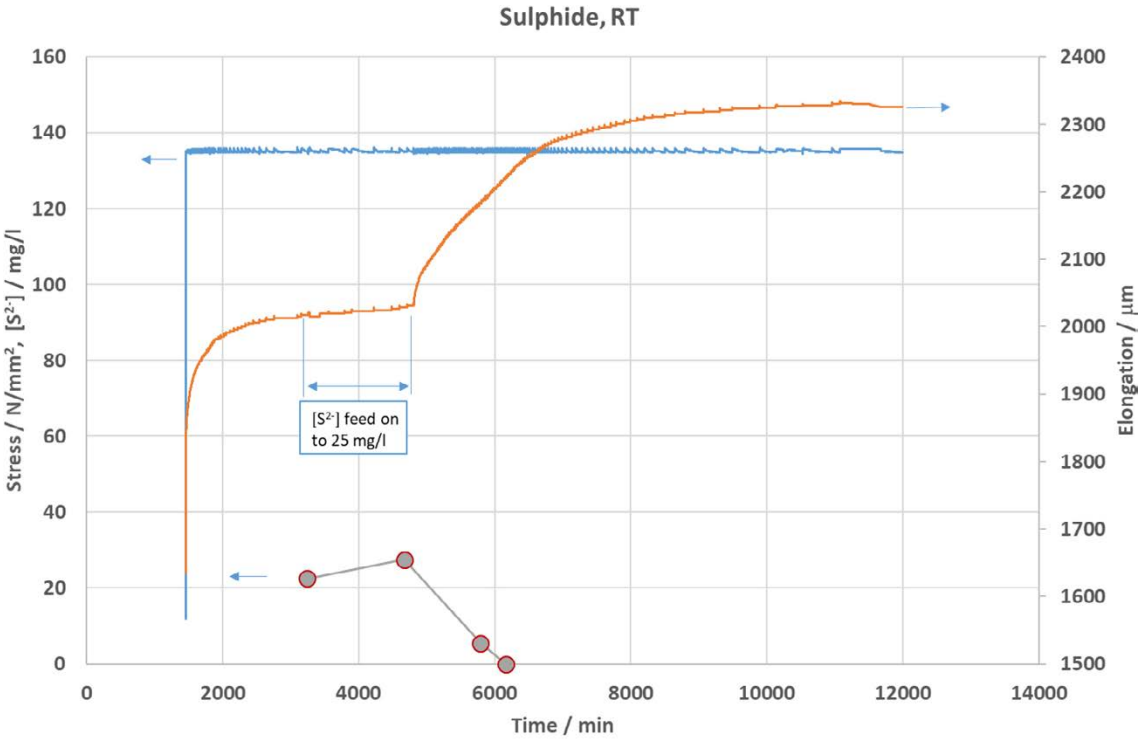

Figure 5-22. *Sulphide concentration (mg/l, left axis, grey circles), stress (N/mm², blue line) and elongation (µm, orange line) as a function of time.*

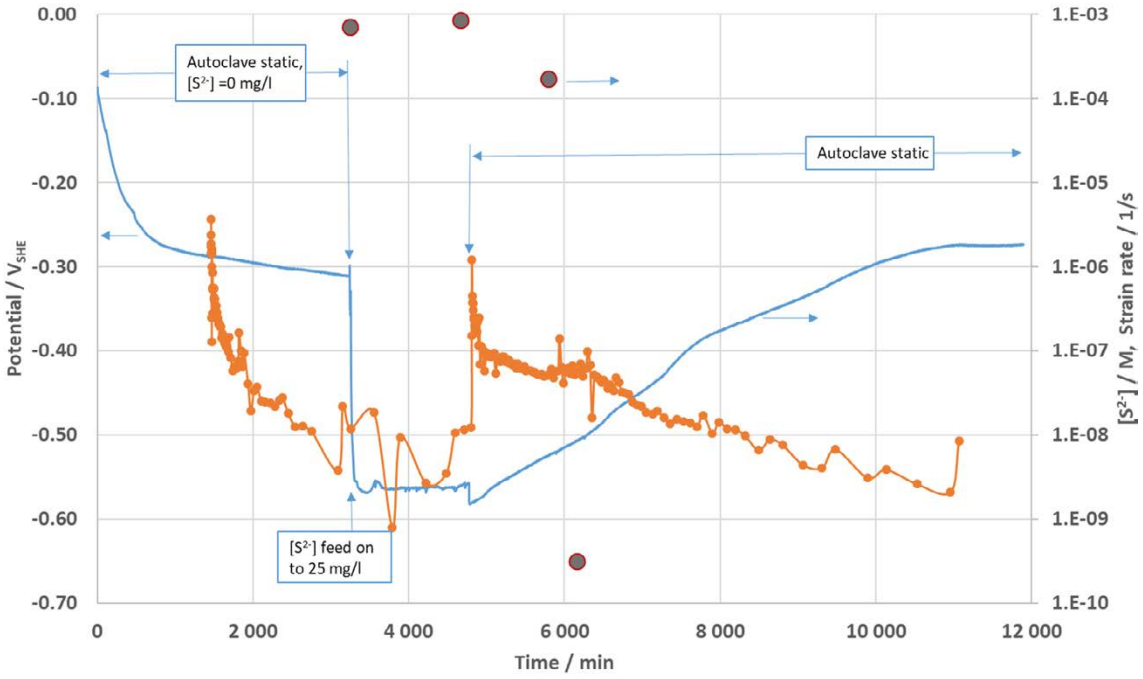

Figure 5-23. *Sulphide concentration (M, right axis, grey circles), strain rate (1/s, right axis, orange circles) and potential (V_{SHE}, left axis, blue line) as a function of time.*

The sulphide feed resulted in an almost instant decrease of the corrosion potential from −0.32 V_{SHE} to −0.56 V_{SHE}, almost exactly the same potential achieved in the previous test with the same sulphide concentration. No change in the strain rate was observed during the sulphide feed. However, almost immediately after stopping the sulphide feed, the strain rate increased by almost two orders of magnitude followed by a slower decrease, while the potential, after an initial small (about 0.02 V) decrease showed a more gradual increase lasting almost until the end of the experiment. The sulphide concentration decreased (after stopping the feed) to zero in about 48 hours.

When comparing the data from the current experiment and the previous one, both show a fast increase in strain rate (by almost two orders of magnitude) almost immediately (within 30 minutes) after stopping the sulphide feed (Figure 5-15 and Figure 5-23). The measured decrease in sulphide concentration after stopping the feed took place in a much slower rate, i.e. about 19 hours from 27.5 mg/l to 5.5 mg/l. The small (about 20 mV) decrease in potential immediately after stopping the sulphide feed, turning the autoclave static and starting the N_2 bubbling through the autoclave, seems to be repeatable (harder to notice in Figure 5-15 because of the larger scale in potential). One possibility for these almost instant effects of stopping the sulphide feed could be due to the sulphide feedline. The tube pump uses silicon tubes, which are known to be possibly slightly permeable to gases, i.e. air. Thus, ingress of oxygen through the silicon tube cannot be excluded. However, since the sulphide solution is of rather high concentration, small amounts of oxygen would be almost instantly consumed in reactions with the sulphide. Thus, because of the slow feed rate (5 ml/min into an 800 ml autoclave volume), it is assumed that no dissolved oxygen can reach the specimen location. On the other hand, the N_2 bubbling gas may contain 1 to 3 ppm of oxygen as an impurity. In the case of the sulphide feed solution, this would be almost immediately consumed in the feed solution glass vessel and not reach the autoclave. After turning the autoclave static, the N_2 bubbling gas is fed directly into the autoclave, where the oxygen impurity may be considered to possibly reach the specimen location within N_2 bubbles. However, this should result in an increase in the potential, in contradiction to the measured data. Based on these considerations we suggest to exclude the possibility of oxygen influence in the potential and strain rate data immediately after turning the autoclave static.

In Test 2, after stopping cathodic polarisations, an increase in strain rate was also observed (Figure 5-8), although not as strong as in the current Test 4. The latter cathodic polarisation (for 1 000 min), in which a more strong increase in strain rate was observed in Test 2, was performed without the presence of sulphide. When the sulphide film is forming (like in Test 3 and Test 4), hydrogen may be able to penetrate the surface layer of the sample and stay there for as long as the sulphide concentration is stable in the water near the specimen surface. One could argue that when the sulphide feed is stopped, hydrogen is then able to come out from the surface layer (because of lower “hydrogen pressure” on the water side) and causes an increase in strain rate (and possibly also the small initial decrease in potential). This hypothesis would explain also the observed effect of cathodic polarisation. An alternative hypothesis could be the reductive dissolution of the sulphide film, producing vacancies in the material and causing (transient) enhanced creep.

5.1.5 Test 5 – strain rate in water with cathodic polarization

In this test, the target was to study further the effect of cathodic polarization. In Test 2, after stopping cathodic polarisations, an increase in strain rate was observed (Figure 5-8). It is noteworthy that the cathodic polarisations during Test 2 were performed on a specimen that had seen sulphide before, i.e. presumably the surface film on the specimen was that of Cu_2S. In test 5 here, the whole testing period was performed in the buffer solution, without introducing sulphide at any point. At the pH = 7.2 used in this study, below the potential of about +0.04 V_{SHE} the stable phase is pure Cu, i.e. there is no film on the surface.

The stress and elongation of the first phase of the experiment are shown in Figure 5-24, and the potential and strain rate in Figure 5-25, as a function of time. The three cathodic polarisations performed during this phase are marked in the Figures. A human error was made just before the first cathodic polarisation in that for about one minute the polarisation was on as anodic one, i.e. a positive polarisation at +1.0 mA/cm^2 instead of the intended −1.0 mA/cm^2. Based on this, the small increase in strain rate visible in Figure 5-25 at about t = 4 100 min may well be a result from the anodic excursion. The second cathodic polarization was made for 2 hrs at about t = 4 500 min. Here the strain rate is observed to possibly show some increase, but the change is so small that no conclusion could be made based

on this result. The third cathodic polarization was made for 8 hrs at about t = 7 500 min. Here, a clear increase in strain rate (about ×5) can be noticed *during* the polarization (from 1.7×10^{-9} 1/s to 8.4×10^{-9} 1/s). During the cathodic polarizations the potential decreased down to about −1.1 V_{SHE}, and after the polarization is switched off, the open circuit potential rather quickly stabilizes at about −0.42 V_{SHE}, Figure 5-25. This potential is at the so-called hydrogen line (the equilibrium potential of H_2/H^+) at the pH of 7.2.

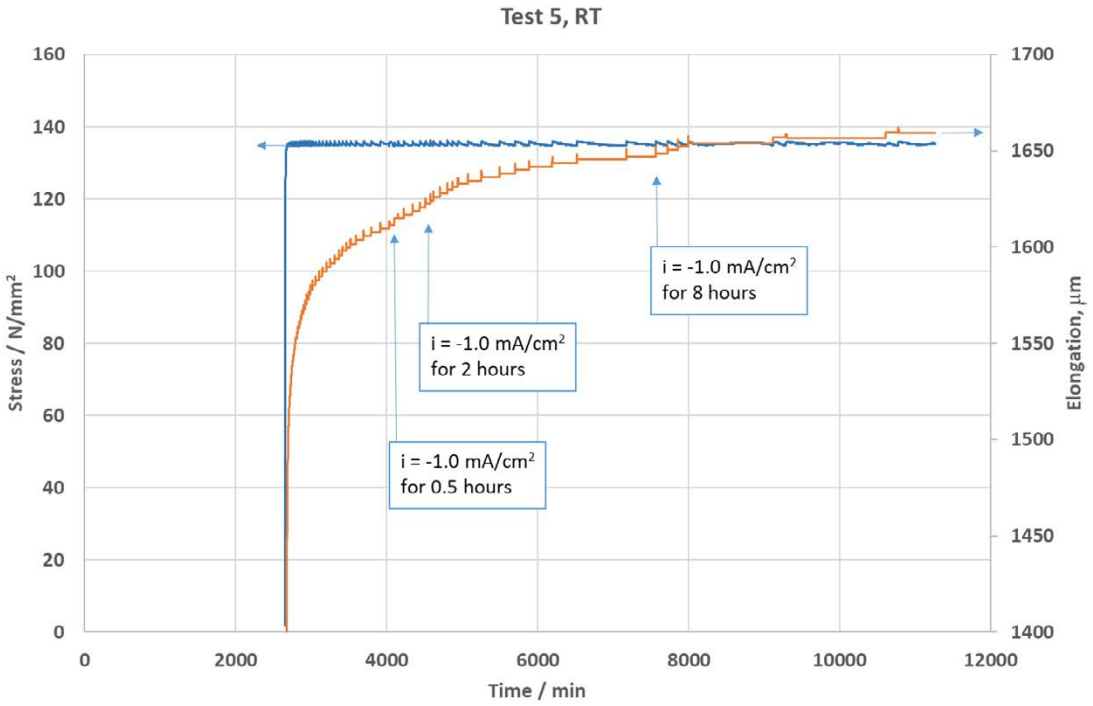

Figure 5-24. *Stress (N/mm², blue line) and elongation (µm, orange line) as a function of time, Phase 1.*

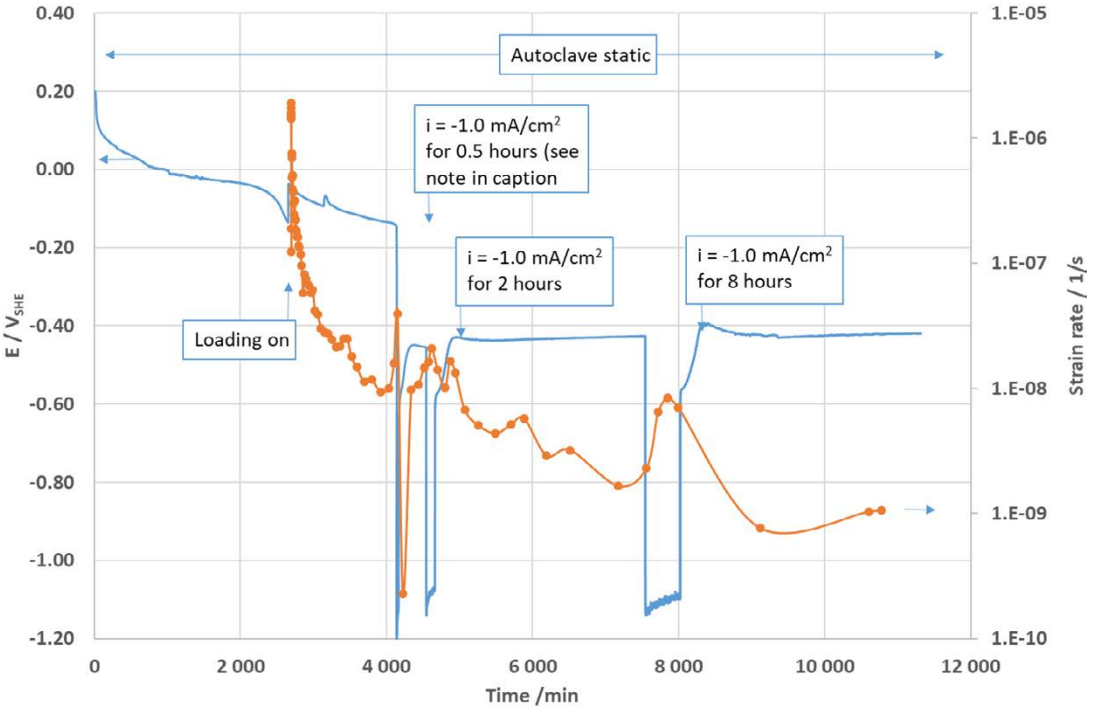

Figure 5-25. *Strain rate (1/s, right axis, orange circles) and potential (V_{SHE}, left axis, blue line) as a function of time, Phase 1. Note: anodic polarization to +1.0 mA/cm² was switched on for about one minute (by human error) just before starting the cathodic polarization.*

In Phase 2 of this experiment, a total of four cathodic polarizations were performed (−1.0 mA/cm^2 for 8 hours each, followed by an about 48 hours waiting period at open circuit). The stress and elongation during this phase are shown in Figure 5-26. No clear correlation of the cathodic polarizations and the elongation rate can be noticed. After the first two cathodic polarizations, since no increase in elongation rate was noticed, an unloading cycle was performed (at about t = 18 450 min) in an attempt to re-activate the dislocation structure, phenomenon seen in Test 4 and known based on the literature (see Mannesson and Andersson-Östling 2016). As seen in Figure 5-26, the unloading cycle did not result in a noticeable increase in the elongation rate. The two cathodic polarizations following the unloading cycle also did not result in a noticeable increase in the elongation rate. The potential is shown in Figure 5-27 as a function of time, and follows the trend found in Phase 1 (Figure 5-25). Since no correlation between the cathodic polarizations and the elongation rate were found, only an average strain rate over the whole period of Phase 2 was calculated, resulting in $\dot{\epsilon} \approx 1.2 \times 10^{-9}$ 1/s.

The reason why in the current Test 5 cathodic polarization was seen to have only a minor effect on the strain rate or no effect at all could be the role of sulphide film in the hydrogen charging process. Typically, when hydrogen charging is performed, a recombination poison ($NaAsO_2$ or As_2O_3 as in Leijon et al. 2018 and in Yagodzinsky et al. 2012) is added into the water. The role of the recombination poison is to prevent hydrogen ions on the metal surface from recombining into hydrogen gas (H_2) and escaping in gaseous form. Thus, hydrogen ions will tend to diffuse into the metal. It can be hypothesized that the sulphide film present in Test 2 (in which cathodic polarization was found to clearly increase the strain rate) played the role of the recombination poison. Since, presumably, in the current test there was no film at all on the surface, hydrogen produced by cathodic polarization would recombine easily to H_2 gas and escape into the autoclave volume, leaving a much smaller chance of hydrogen entering the material and affecting the creep rate.

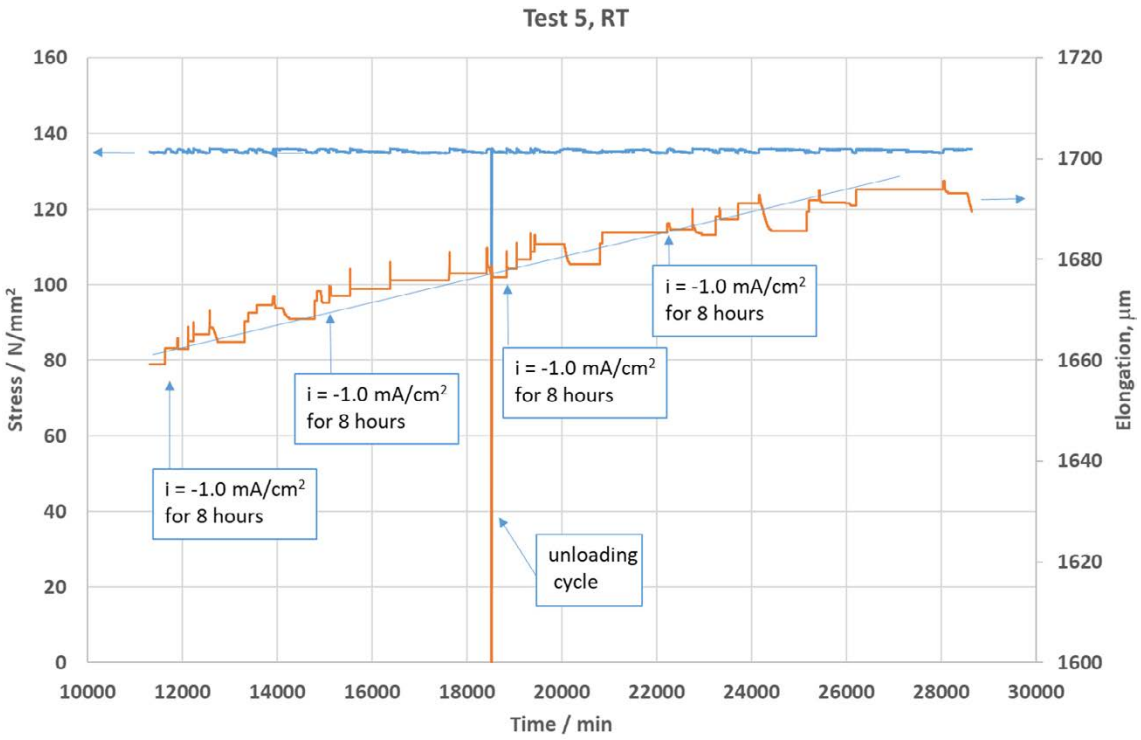

Figure 5-26. *Stress (N/mm^2, blue line) and elongation (µm, orange line) as a function of time, Phase 2.*

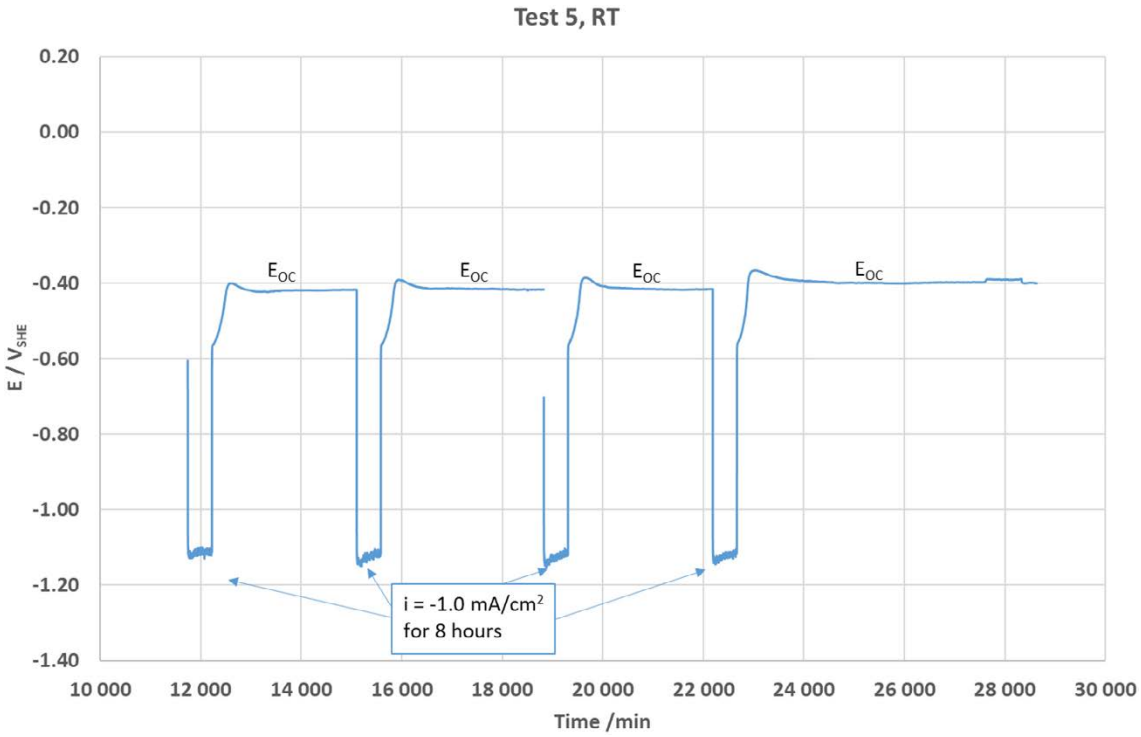

Figure 5-27. *Potential (V_{SHE}) as a function of time, Phase 2.*

5.1.6 Test 6 – strain rate in water with sulphide and cathodic polarization

In this test, the effect of sulphide feed and following three consecutive cathodic polarisations was studied, with a stabilisation period of about two days in between changes. Figure 5-28 shows the stress and elongation as a function of time and Figure 5-29 the potential and strain rate as a function of time. During the sulphide feed (about 25 mg/l, lasting for about 22 hours) the elongation rate followed the trend set previously, i.e. no change caused by the sulphide feed, Figure 5-28. However, about two hours after stopping the sulphide feed the elongation rate shows a marked (transient) increase, lasting for about 40 hours. The first cathodic polarisation (to a current density of −1 mA/cm^2 for 8 hours) at about t = 19 000 min also resulted in a marked increase in the elongation rate, whereas the two following similar cathodic polarisation caused no appreciable change in the elongation rate, Figure 5-28.

The sulphide feed resulted in the corrosion potential decrease from about −0.25 V_{SHE} to −0.57 V_{SHE}, Figure 5-29. Termination of the sulphide feed was followed by an increase of the strain rate by about one order of magnitude, whereas a roughly similar increase of strain rate was seen already *during* the first cathodic polarisation, Figure 5-29. The following two similar cathodic polarisations did not result in a clearly marked increase in the strain rate. Two previous studies on the effect of hydrogen charging on the creep of Cu-OFP (Leijon et al. 2018, Yagodzinsky et al. 2012) have shown a rather consistent increase of creep rate due to the continuous hydrogen charging. However, since these tests were performed in 1 M H_2SO_4 the pH of which is about pH = 1 and with an arsenic (As) containing hydrogen recombination poison, and at a very low cathodic potential of about −0.5 V_{SHE} at which the stable surface film is Cu_3As (and are thus of course not representative of the repository environment), the results cannot be directly compared with the current work.

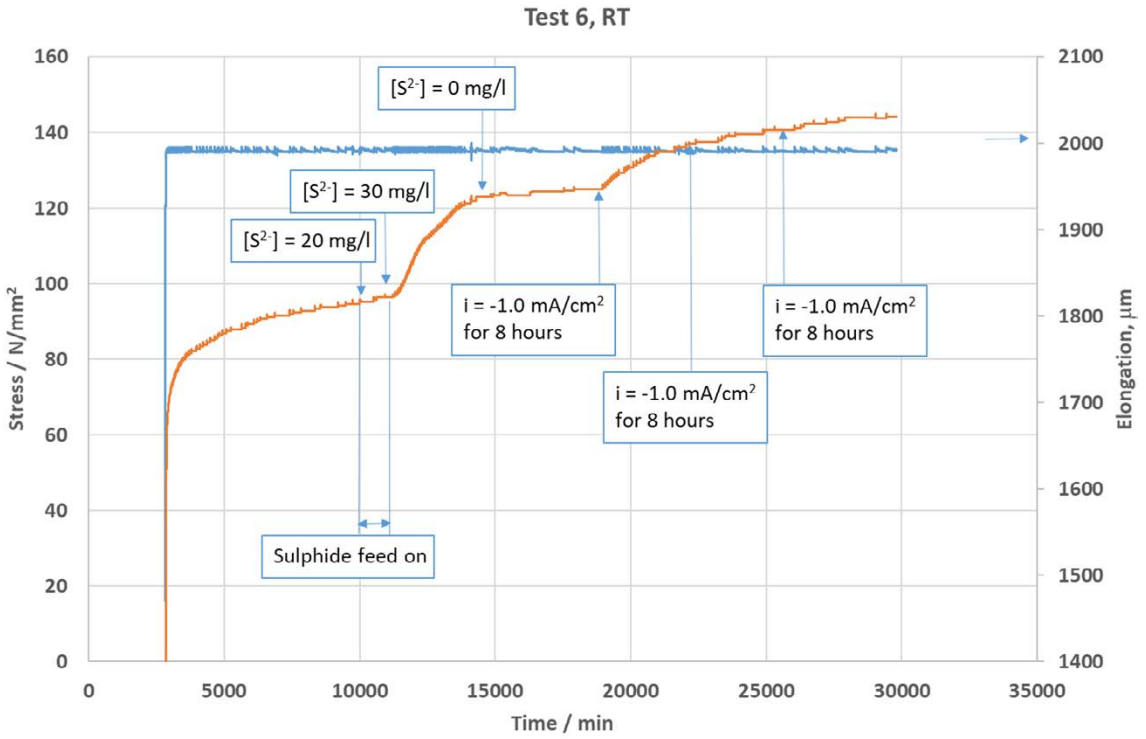

Figure 5-28. *Stress (N/mm², blue line, left axis) and elongation (µm, orange line, rigth axis) as a function of time.*

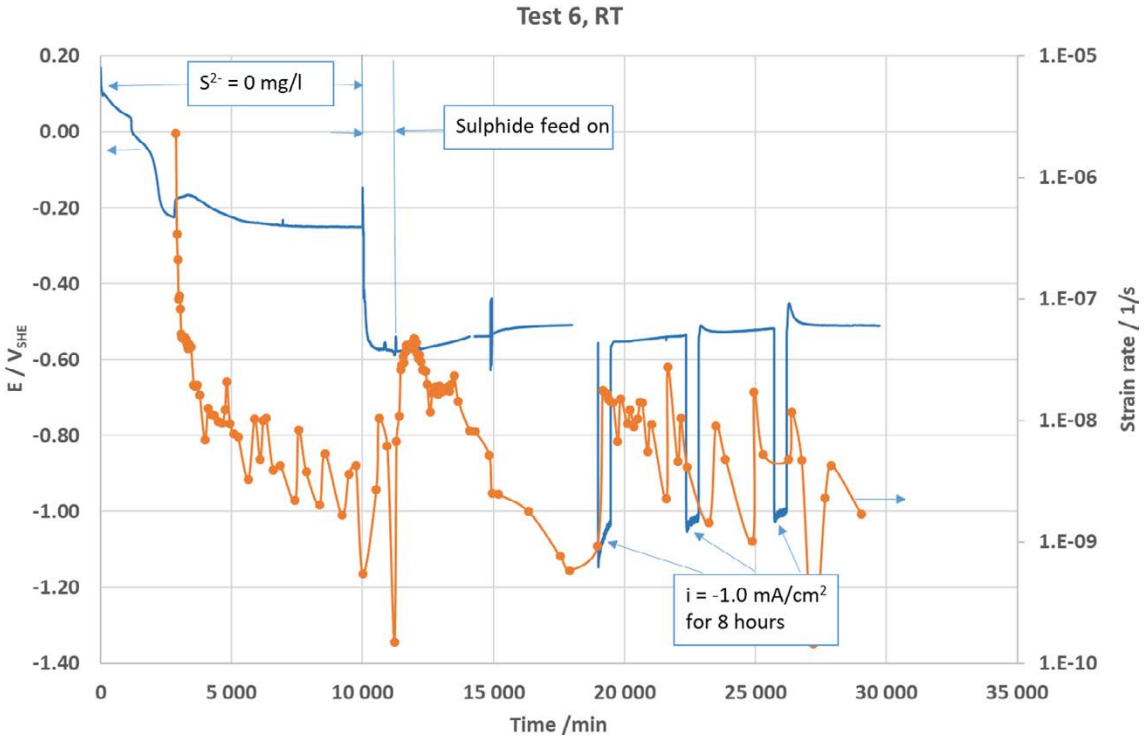

Figure 5-29. *Strain rate (1/s, right axis, orange circles) and potential (V_{SHE}, left axis, blue line) as a function of time.*

5.1.7 Test 7 – strain rate in water with cathodic and anodic polarization

This test was run to verify the effect of cathodic polarization on the creep rate, as well as to study the effect of forming a film on Cu-OFP at anodic potentials and then reducing the film with cathodic polarization. The hypothesis behind the anodic polarizations was to investigate whether the reduction of a film formed by anodic polarisation (to potentials either in the stability area of Cu_2O or $Cu(OH)_2$ would result in injection of vacancies into the material and thereby an increase in creep rate.

The stress and elongation curves as a function of time are shown in Figure 5-30 and the potential as a function of time in Figure 5-31. The first cathodic polarization resulted in a transient increase of strain rate (by a factor of about ×1.5), while the second one resulted in no increase. The first anodic polarisation (to +0.145 V_{SHE} for 60 min), followed by open circuit conditions (for 24 hours) showed no change in creep rate, while the second one, followed by immediate cathodic polarization, showed a moderate (transient) increase in the strain rate. Further anodic polarisations showed no clear increases in strain rate. Thus, it seems that either the reductive dissolution is not able to produce vacancies injected to the material, or, as an alternative explanation, the surface of the Cu-OFP material becomes saturated by some mechanism preventing further effects on creep rate.

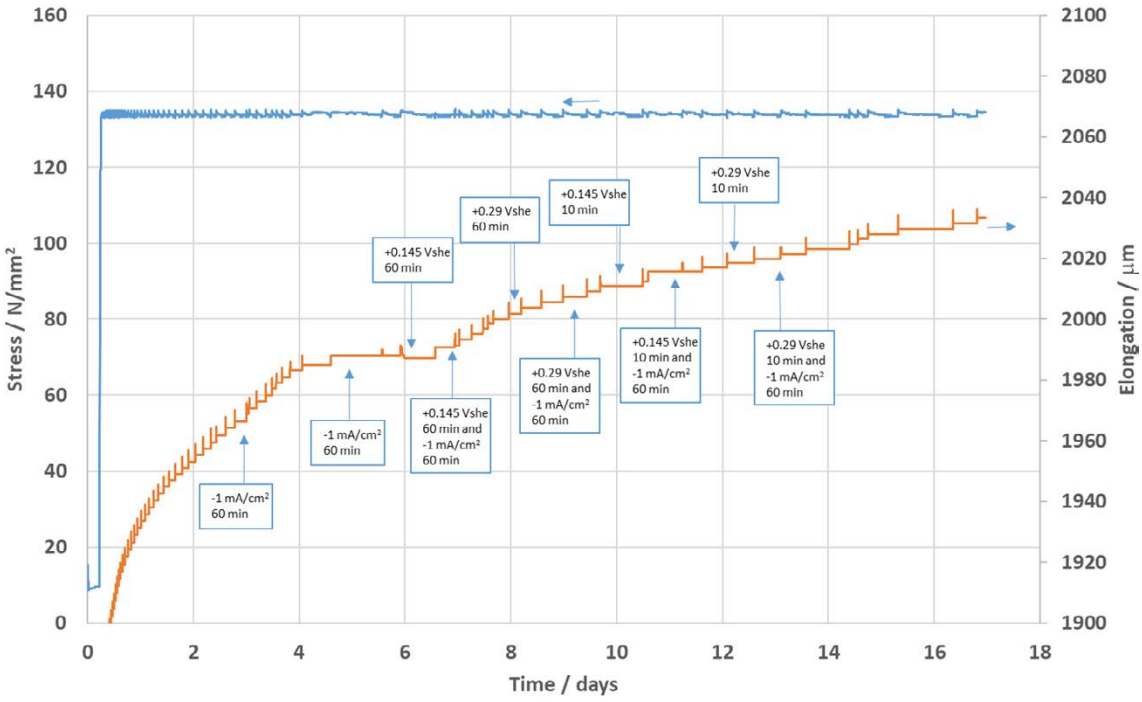

Figure 5-30. *Stress (N/mm², blue line, left axis) and elongation (µm, orange line, rigth axis) as a function of time.*

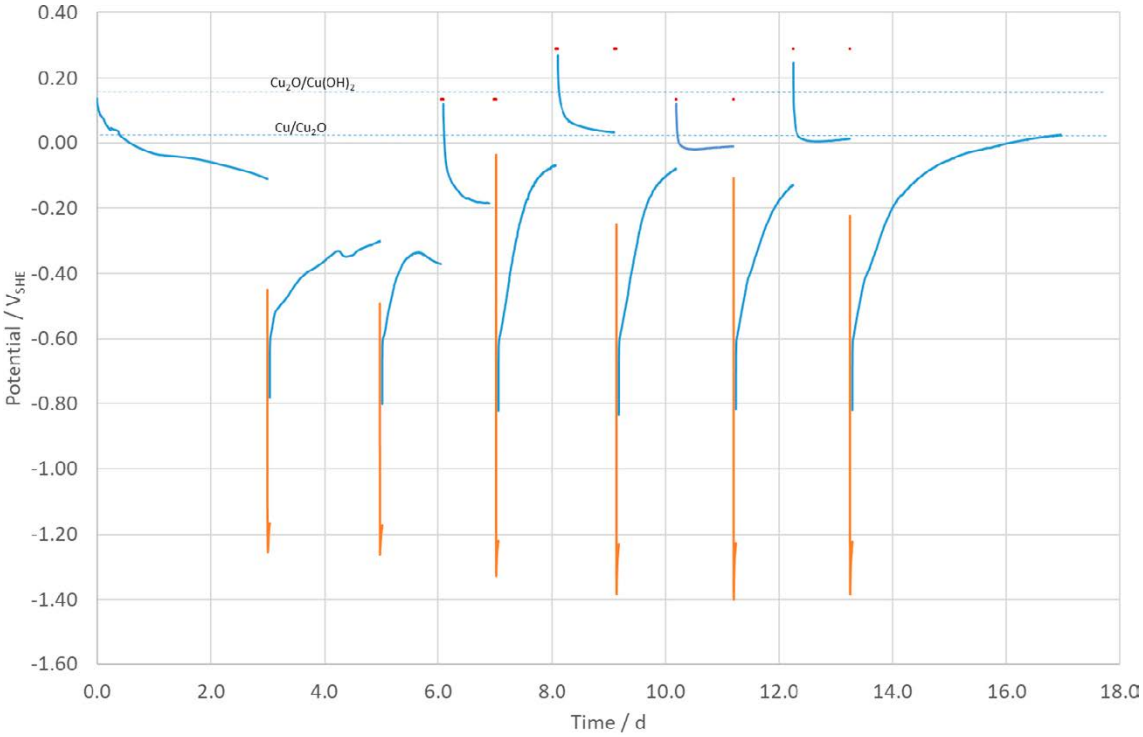

Figure 5-31. *Potential (V_{SHE}) as a function of time. Blue lines – open circuit, orange lines – cathodic polarization (−1.0 mA/cm^2 for 60 min), red dots – anodic polarization (to +0.145 V_{SHE} or +0.29 V_{SHE}, for 60 min (first four polarizations) and for 10 min (last four polarizations)).*

5.1.8 Summary of creep tests

A set of the creep tests were performed on Cu-OFP as shown in Table 5-1.

The purpose of Test 1 was to verify whether the experimental finding of Aaltonen et al. (2003) of Cu-OFP strain rate increasing due to large anodic polarization is repeatable. In this work, similar strain rates were achieved, despite some differences in the experimental conditions. However, the increase in strain rate was found to be transient in that when the anodic polarization was switched off, the creep rate was found to rapidly decrease to roughly the level preceding the anodic polarization, within a few hours of time. Cathodic polarization was found to also increase the strain rate, although much less. The fact that the specimen failed by SCC precludes further conclusions to be made, since it is unclear at which stage of the test the first micro-cracks had initiated, which certainly would be seen as an increase in the overall strain rate. Thus, the current results cannot be taken as conclusive evidence of the mechanism of vacancy injection increasing the strain rate, as proposed by Aaltonen et al. (2003).

Tests 2, 3, 4 and 6 were primarily performed to verify whether exposure to a sulphide containing environment would result in an enhanced strain rate in Cu-OFP. The results indicate a complex behaviour, in that introduction of sulphide per se did not increase the strain rate, whereas an increase in the strain rate was observed right after the sulphide feed was stopped. Two main hypotheses for the increase in strain rate after stopping the sulphide feed were presented, the first one involving introduction of hydrogen into the Cu-OFP material during the sulphide exposure and the second one involving reductive dissolution of the sulphide film. Anodic polarization during the sulphide feed was observed to increase the strain rate, although to a much smaller degree than in the $NaNO_2$-environment. Cathodic polarization was found to result in a moderate increase in strain rate in some cases studied.

Test 5 was performed to study the effect of cathodic polarization in the buffer solution without the presence of sulphide. Strain rate was found to increase moderately in some cases.

Test 7 was primarily performed in the buffer solution without sulphide to study the effect of preceding anodic polarization on the strain rate during the following cathodic polarization. Anodic polarization to the stability areas of Cu_2O and $Cu(OH)_2$ was performed to see whether there is a difference in the behaviour during cathodic polarization depending on the nature of the film formed during the anodic polarizations. The strain rate was found to increase moderately after the first anodic polarizations followed by immediate cathodic polarization. However, on repetition no clear increase in strain rate could be detected.

Test 8 was performed in air to provide a specimen for the AFM evaluation (see Section 5.2.1 Air tested specimen) and nanohardness measurements (see Section 5.2.2 Air tested specimen). The creep curve is shown as part of Figure 5-21 (blue line, marked as "Air").

The main findings were firstly that in 1 M $NaNO_2$ the strain rate of Cu-OFP increases due to a large anodic polarization, lending support to the vacancy-creep mechanism of creep proposed by Aaltonen et al. However, the effect was found to be of transient nature only. Secondly, exposure of Cu-OFP to a sulphide environment (up to 25 mg/l) did not increase the strain rate, although after stopping the sulphide feed a transient increase in strain rate was observed.

Table 5-1. Summary of creep tests.

Experiment	Anodic polarisation	Increase in $\dot{\epsilon}$	Cathodic polarisation	Increase in $\dot{\epsilon}$	HS^-	Increase in $\dot{\epsilon}$	Remarks
Test 1. 1M $NaNO_2$	60 min at +1 mA/cm^2	yes	30 min at −0.5 V_{SHE}	yes	0	-	Failed by SCC
	60 min at +0.1 mA/cm^2	~no	-	-	0	-	
Test 2. HS^-	60 min at +1 mA/cm^2	yes	1 000 min at −0.5 V_{SHE}	yes	10^{-4} M from start	-	
	60 min at +0.05 mA/cm^2	no	-	-	10^{-4} M from start	-	
Test 3. HS^-	60 min at +1 mA/cm^2	yes	-	-	10^{-3} M	no	Increase in $\dot{\epsilon}$ after stopping HS^- feed
Test 4. HS^-	-	-	-	-	10^{-3} M	no	Increase in $\dot{\epsilon}$ after stopping HS^- feed
Test 5. no HS^-	-	-	several, −1 mA/cm^2 for 0.5 to 8 hours	yes, in some	0	-	
Test 6. HS^-	-	-	several, −1 mA/cm^2 for 8 hours	yes, in some	10^{-3} M	no	Increase in $\dot{\epsilon}$ after stopping HS^- feed
Test 7. No HS^-	+0.145 or +0.29 V_{SHE} 10 or 60 min	yes, in first	several, −1 mA/cm^2 for 60 min	yes, in first	0	-	
Experiment	**Anodic polarisation**	**Increase in $\dot{\epsilon}$**	**Cathodic polarisation**	**Increase in $\dot{\epsilon}$**	**HS^-**	**Increase in $\dot{\epsilon}$**	**Remarks**
Test 8. Air	-	-	-	-	-	-	Ref. test

5.2 AFM and nanohardness measurements

Topographic characterization of as prepared and tested specimens was performed via atomic force microscopy (AFM) in tapping mode. In addition, post-AFM surface observations using stereo and scanning electron microscope techniques were performed. After the microscopic investigations, cross sections were prepared and nanohardness measurements were performed to characterize the hardness profile starting inwards from the surface.

Characterizations were performed on three specimens:

1. polished and non-tested,
2. polished and tested in air (Test 8 in Table 5-1), and
3. polished and tested for 48 h in a sulphur-containing environment.

Three relative locations were measured within each specimen's gauge length as shown in Figure 5-32. As indicated in the figure, the measurement locations will be referred to as mid-mid, quarter-mid and mid-quarter from this point forward.

5.2.1 AFM measurements

As-polished specimen

Visualization of the specimen in the AFM revealed dark, crate/pit -like features. AFM measurements were performed on 10 µm × 10 µm locations, avoiding the crater/pit-like features. The as-polished mid-mid, quarter-mid and mid-quarter locations were measured and the results can be seen in Figure 5-33, as contour maps, and Figure 5-34, as 3D visualizations. The grinding and polishing markings are clearly visible in the mid-mid and quarter-mid locations. Polishing markings are less visible mid-quarter location and the general surface topography appears different.

Information such as maximum profile height (S_Z, the maximum height of the profile which indicates the absolute vertical distance between the maximum profile peak height and the maximum profile valley depth along the sampling length), projected surface area (SA_P, the geometrical area scanned, i.e. the nominal sample surface area), measured/covered surface area (SA_{CA}, the real surface area) and volume of the covered area (V_{CA}) were extracted from the AFM data and are presented in Table 5-2. In the case of the air tested and sulphide tested specimens only an area of 10 µm × 2.5 µm could be used for each measurement. For this reason, additional parameters (normalized surface area (SA_N = SA_{CA}/ S_{AP}) and relative volume[2] (V_{REL})) are also given in Table 5-2 to ease comparison. The extracted data for as-polished mid-mid and quarter-mid locations is very similar, and confirmed by their appearance (Figure 5-33 and Figure 5-34), while the mid-quarter location is very different. It may be presumed that this is a very local variation in surface finish and may not fully represent the specimen as a whole.

Table 5-2. The maximum profile height (S_Z), projected surface area (SA_P), covered surface area (SA_{CA}), dimensionless surface area ($SA_N = SA_{CA}/SA_P$)), volume (V_{CA}, integral of the surface height over the covered area) and relative volume (V_{REL}, for a smaller covered area – 10 µm × 2.5 µm) for the as-polished specimen.

Location	Sz (µm)	SA_P (µm²)	SA_{CA} (µm²)	SA_N (dimensionless)	V_{CA} (µm³)	V_{REL} (µm³)
mid-mid	0.60908	100.000	111.188	1.11	22.7123	5.68
quarter-mid	0.53687	100.000	106.558	1.07	20.1472	5.04
mid-quarter	1.00255	100.000	109.264	1.09	50.2014	12.55

[2] The relative volume (calculated for an area of 10 µm × 2.5 µm) can be compared to the AFM data extracted from the measurements performed on the tested specimens.

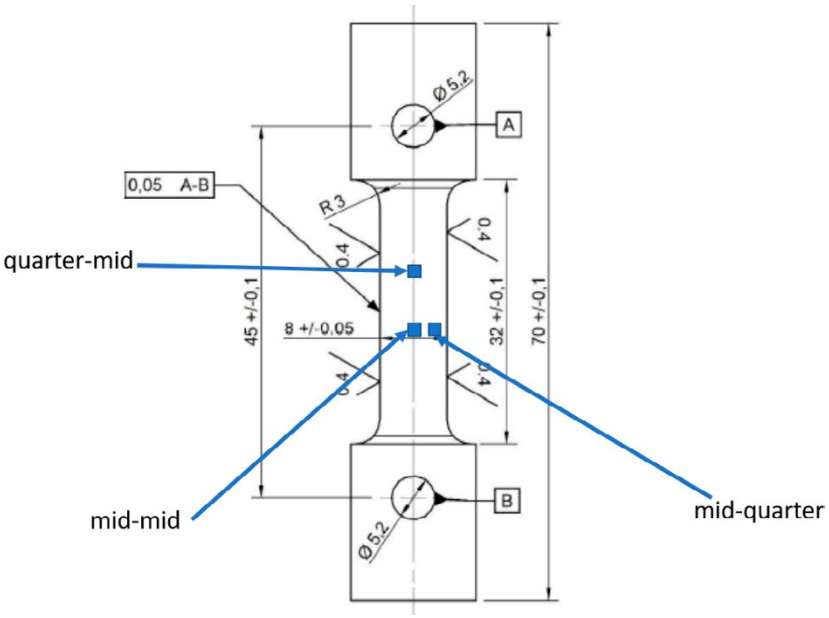

Figure 5-32. *Relative locations of AFM measurements. The AFM measurement zones (i.e. blue boxes) are not shown to scale.*

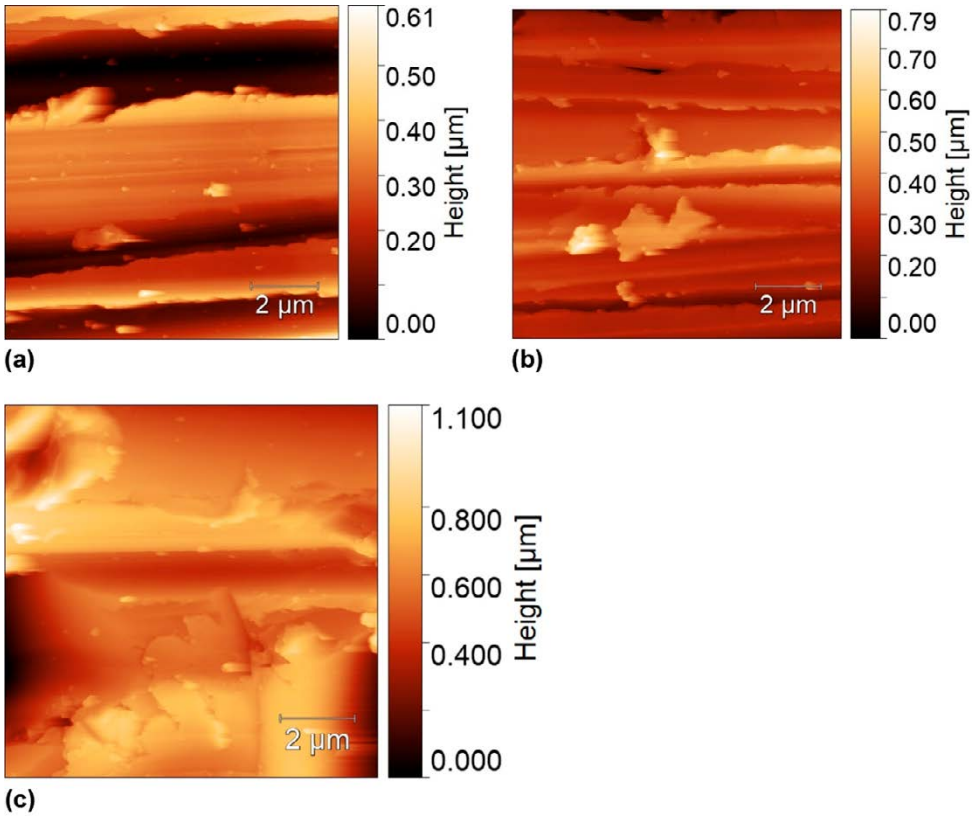

Figure 5-33. *AFM contour maps of the as-polished specimen at (a) mid-mid, (b) quarter-mid and (c) mid-quarter locations.*

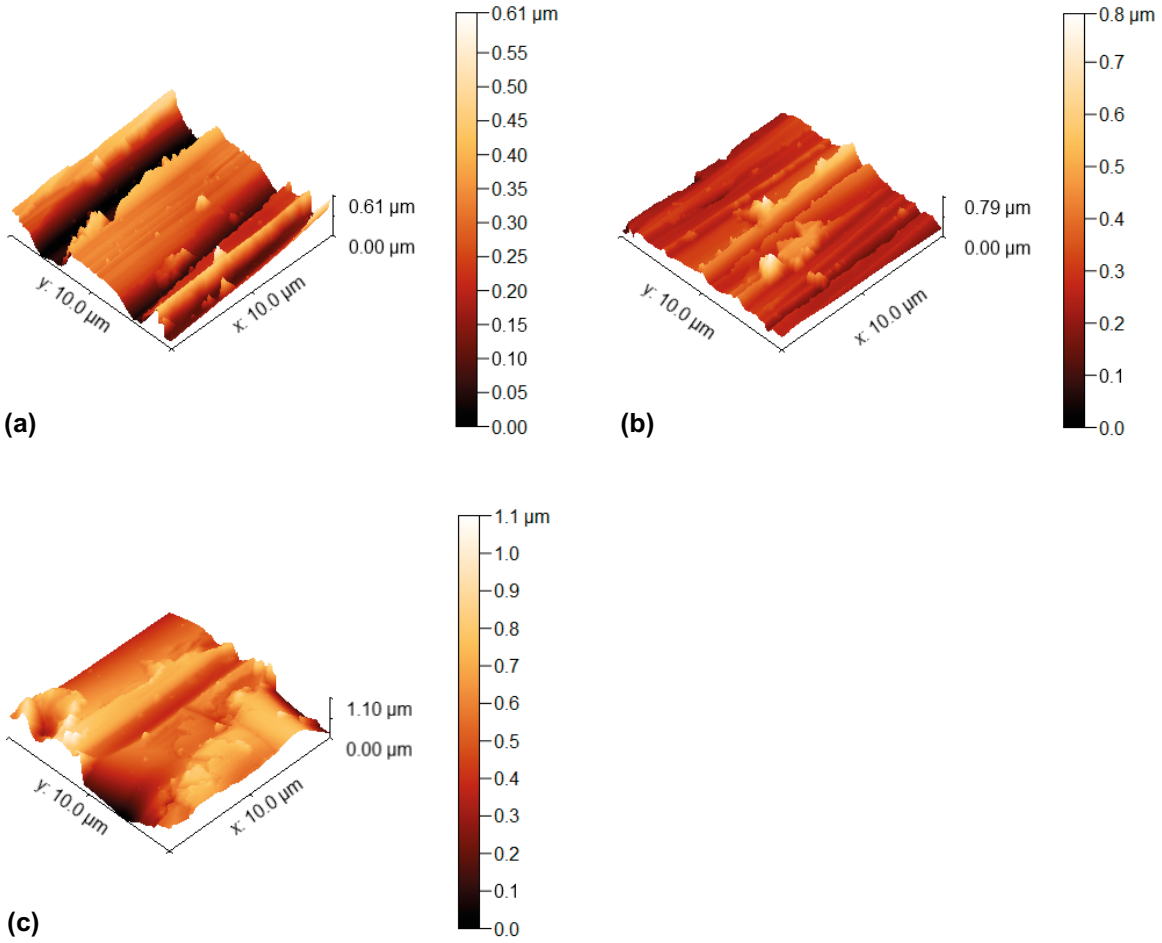

Figure 5-34. *3D AFM mapping of the as-polished specimen at (a) mid-mid, (b) quarter-mid and (c) mid-quarter locations.*

Air tested specimen

After testing in air (for 66 hrs, up to a strain of about 8 %) and removing the sample from the loading frame, the air tested specimen was slightly deformed. This resulted in significant difficulties in fixing the specimen to the measurement stage and, moreover, due to the sloping and irregular surface, measurements areas were restricted to 10 µm × 2.5 µm, unlike for the as-polished specimen where 10 µm × 10 µm areas were mapped. AFM contour maps of the air tested specimen can be seen in Figure 5-35 for the (a) mid-mid, (b) quarter-mid and (c) mid-quarter locations. In Figure 5-36, 3D visualisations of the surface can be seen. Comparing the extracted parameters of the un-tested (Table 5-2) and the air tested (Table 5-3) specimens, no clear differences can be observed.

Table 5-3. The maximum profile height (Sz), projected surface area (SA_P), covered surface area (SA_{CA}), dimensionless surface area ($SA_N = SA_{CA}/SA_P$)) and volume (V_{CA}, integral of the surface height over the covered area) after testing in a room temperature air environment.

Location	Sz (µm)	SA_P (µm²)	SA_{CA} (µm²)	SA_N (dimensionless)	V_{CA} (µm³)
mid-mid	0.5690	25.0000	30.0094	1.20	6.97437
quarter-mid	0.5067	25.0000	27.5742	1.10	4.82053
mid-quarter	0.8256	25.0000	28.3394	1.13	8.06349

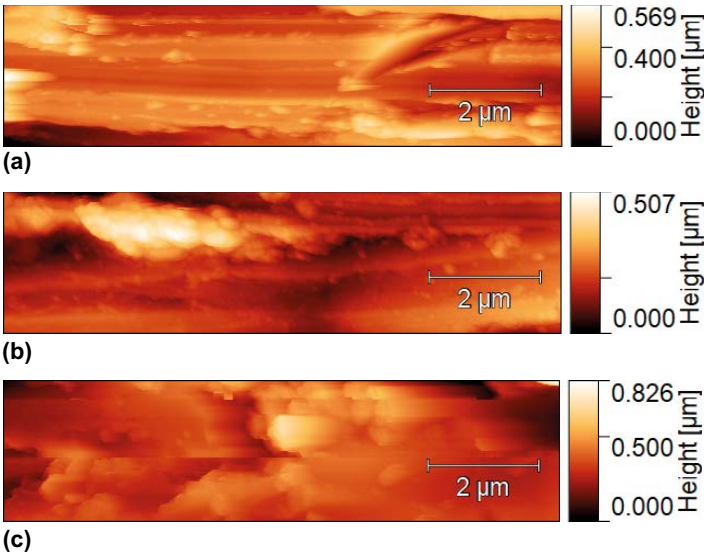

Figure 5-35. *AFM contour maps of the specimen tested in a room temperature air environment at (a) mid-mid, (b) quarter-mid and (c) mid-quarter locations.*

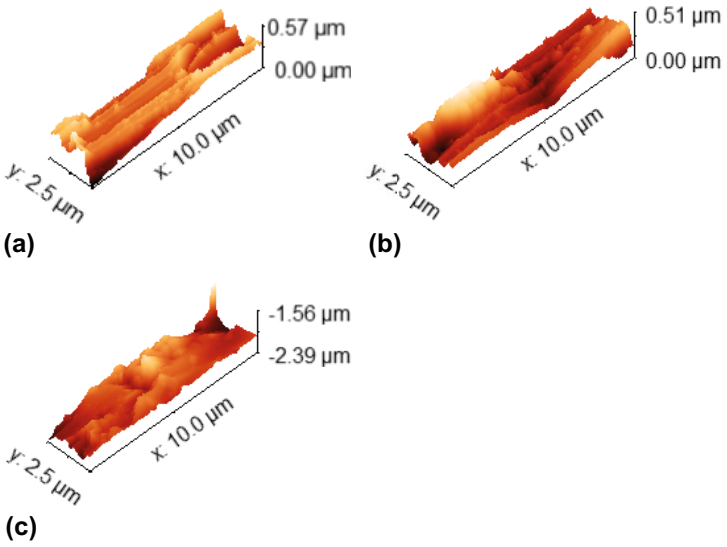

Figure 5-36. *3D AFM mapping of the specimen tested in a room temperature air environment (a) mid-mid, (b) quarter-mid and (c) mid-quarter locations.*

Sulphur-containing environment tested specimen

After testing in a sulphide-containing environment (target 25 mg/l, for 48 hrs, up to a strain of about 8 %) and removing the sample from the loading frame, the specimen was slightly deformed. This resulted in significant difficulties in fixing the specimen to the measurement stage and, moreover, due to the sloping and irregular surface, measurements areas were restricted to 10 µm × 2.5 µm, unlike for the as-polished specimen where 10 µm × 10 µm areas were mapped. Contour maps and 3D visualization of the (a) mid-mid, (b) quarter-mid and (c) mid-quarter locations can be found in Figure 5-37 and Figure 5-38, respectively. The Cu_2S crystallites are visible in these maps. The crystallites range in diameter from several hundred nanometres to approximately 2 µm. In Table 5-4 the extracted parameters from the measurements are presented. The maximum profile height (Sz), covered surface area (SA_{CA}), dimensionless surface area ($SA_N = SA_{CA}/SA_P$)) and volume (V_{CA}, integral of the surface height over the covered area) are all much higher than those measured for the un-tested and air tested samples. This is clearly due to the rather thick sulphide film forming on sulphide tested specimens (6–9 µm for the two samples studied in cross-section by SEM, see 5.3 below).

No significant differences were observed in the three locations. This would indicate that although there is some variation in the surface condition of the as-polished condition, it does not seem to have any significant effect on the crystallite formation during exposure to a sulphur-containing environment.

Table 5-4. The maximum profile height (Sz), projected surface area (SA_P), covered surface area (SA_{CA}), dimensionless surface area ($SA_N = SA_{CA}/SA_P$)) and volume (V_{CA}, integral of the surface height over the covered area) after testing in a sulphur-containing environment.

Location	Sz (µm)	SA_P (µm²)	SA_{CA} (µm²)	SA_N (dimensionless)	V_{CA} (µm³)
mid-mid	1.45595	25.0000	36.0710	1.44	15.8690
quarter-mid	1.23137	25.000	31.1957	1.25	16.1088
mid-quarter	1.73177	25.0000	37.1851	1.49	23.0726

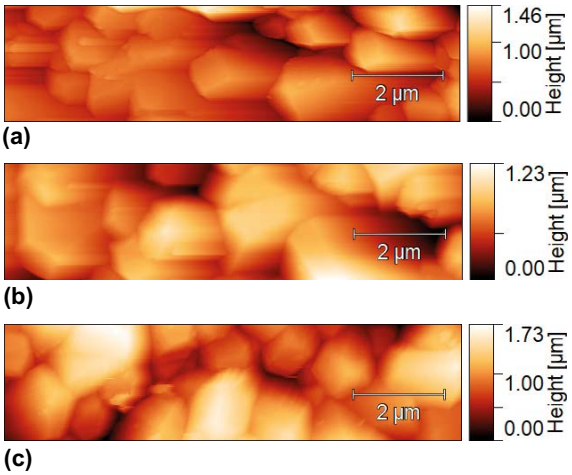

Figure 5-37. *AFM contour maps from the specimen tested in a sulphur-containing environment at (a) mid-mid, (b) quarter-mid and (c) mid-quarter locations.*

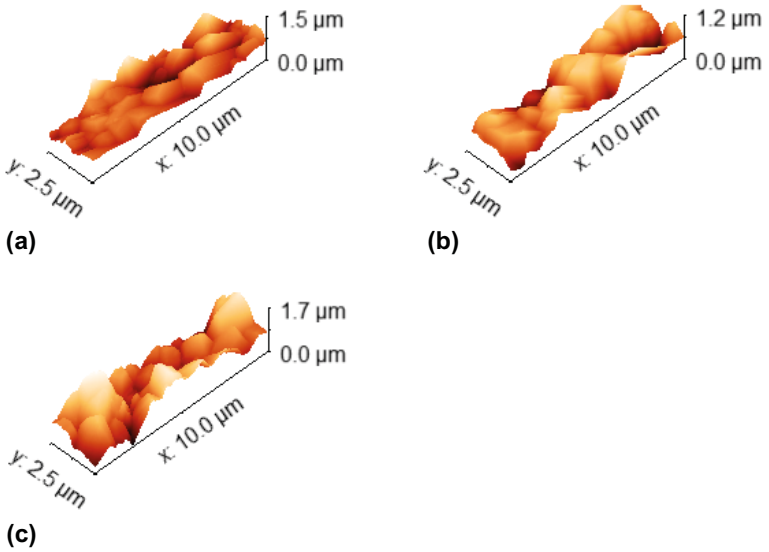

Figure 5-38. *3D AFM mapping of the specimen after exposure to a sulphur-containing environment at (a) mid-mid, (b) quarter-mid and (c) mid-quarter locations.*

5.2.2 Stereo and SEM observations

As-polished specimen

Stereo microscope observations of the as-polished specimen confirmed the presence of both grinding and polishing markings, from polishing to 1200 grit SiC paper, along with crater/pit-like dark features, see Figure 5-39. Grinding/polishing markings are present primarily lengthwise in the gauge length (i.e. parallel to the would-be loading direction). The crater/pit-like features were distributed across the entire gauge length of the specimen. The sample surface and crater/pit-like features were also observed by SEM, see Figure 5-40. The crater/pit-like features can be on the order of tens of µm in diameter and are several µm deep and are relatively homogeneously distributed across the sample's surface. The origin of these features is possibly from the specimen manufacturing phase by EDM, and an insufficient final polishing/removal of the surface layer.

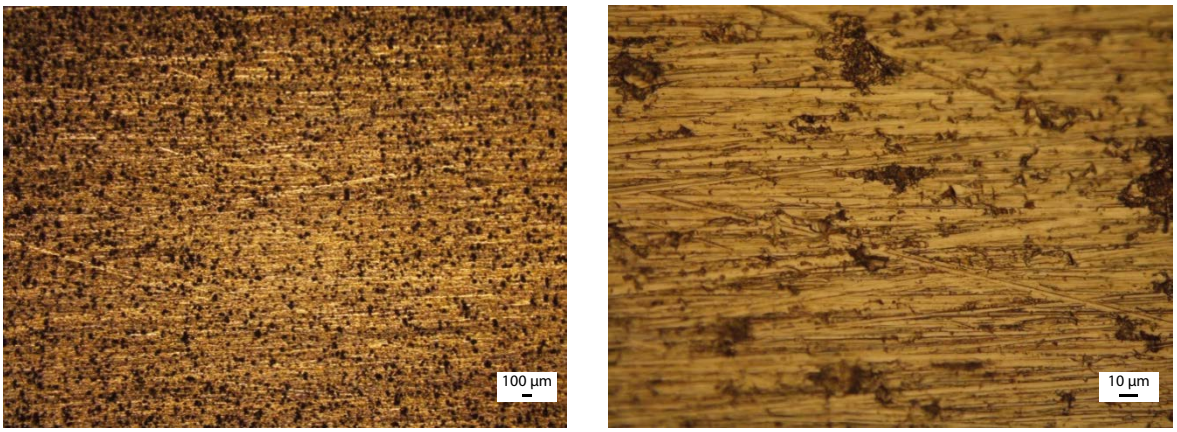

(a) (b)

Figure 5-39. *Stereo microscope images of the as-polished surface. In addition to grinding and polishing marking (1200 grit SiC), dark crater/pit-like features can be observed.*

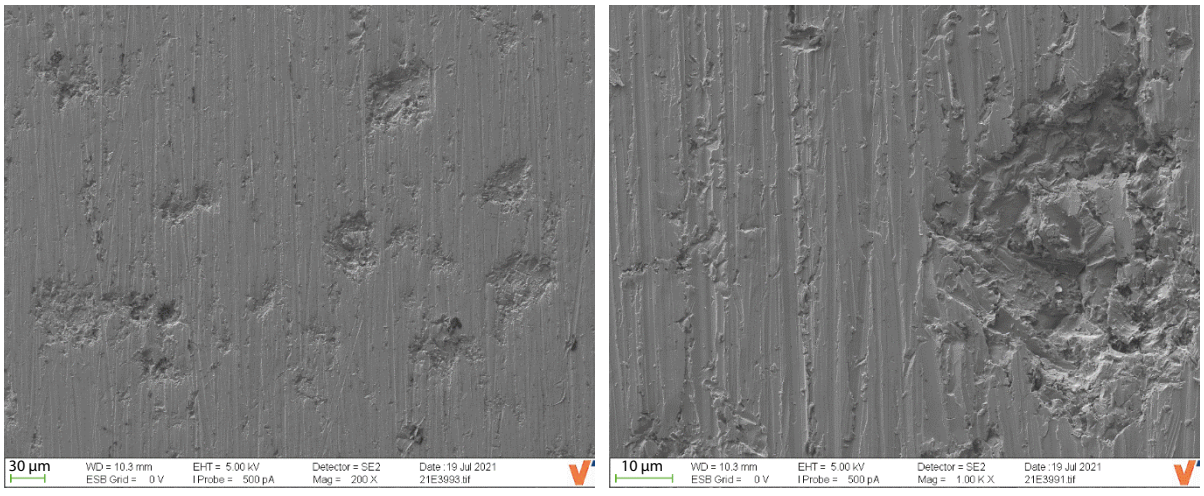

(a) (b)

Figure 5-40. *Secondary electron SEM micrographs of the as-polished surface. In addition to grinding and polishing markings, crater/pit-like features are observed.*

Air tested specimen

Like the as-polished specimen, the air tested specimen's gauge length was covered in crater/pit-like features, see Figure 5-41. Testing in air did not result in any significant visual changes to the sample surface. Grinding/polishing markings are present primarily lengthwise in the gauge length (i.e. parallel to the loading direction). This sample surface was also observed by SEM, see Figure 5-42. The crater/pit-like features appear to be quite homogeneously distributed across the sample's surface and are on the order of tens of µm in diameter and several µm deep. Moreover, there appears to be crack-like indications extending from the crater/pit-like features perpendicular to the loading direction (some examples marked with circles in Figure 5-42). These observations may suggest that these crater/pit-like features could act as preferential crack initiation sites during testing and environmental exposures.

Sulphide-containing environment tested specimen

After testing in a sulphide-containing environment, the specimen was covered in a grey deposit/scale, see Figure 5-43. Nonetheless, there seems to be possibly some indication of craters/pit-like features on the sample surface (see Figure 5-43(b)). In addition, the grinding and polishing markings are still somewhat visible. Grinding/polishing markings are present primarily lengthwise in the gauge length (i.e. parallel to the loading direction). This sample surface was also observed by scanning electron microscopy, Figure 5-44 and Figure 5-45. The surface is covered in a homogeneous layer of crystallites ranging from approximately several hundreds of nanometres to 1–2 µm, Figure 5-45. These crystallites were identified by semi-quantitative SEM energy-dispersive X-ray spectroscopy (SEM-EDS) as likely Cu_2S crystallites, see Figure 5-46. Moreover, the morphology of these crystallites is in agreement with what is reported in the literature for Cu_2S (see Chen et al. 2017).

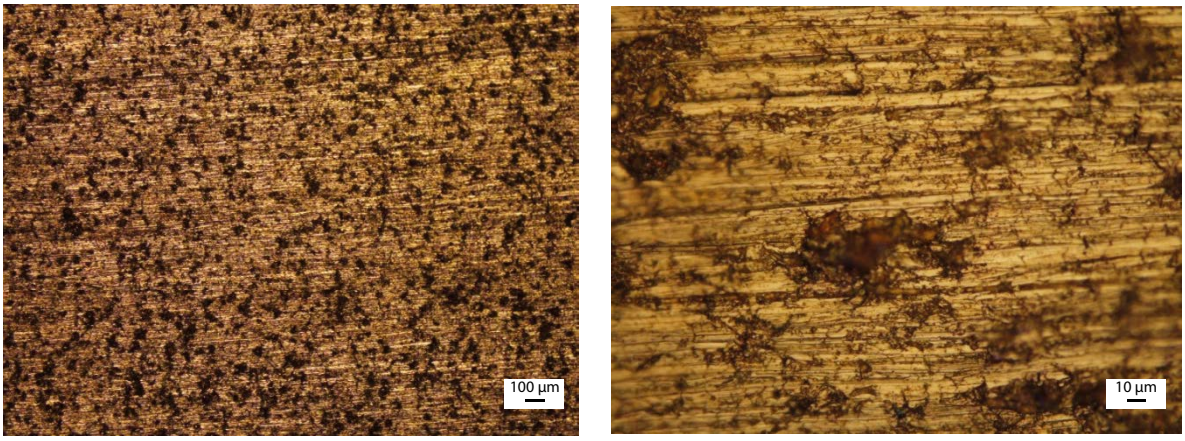

(a) **(b)**

Figure 5-41. *Stereo microscope images of the sample surface after testing in air. In addition to grinding and polishing marking (1200 grit SiC), dark crater/pit-like features can be observed.*

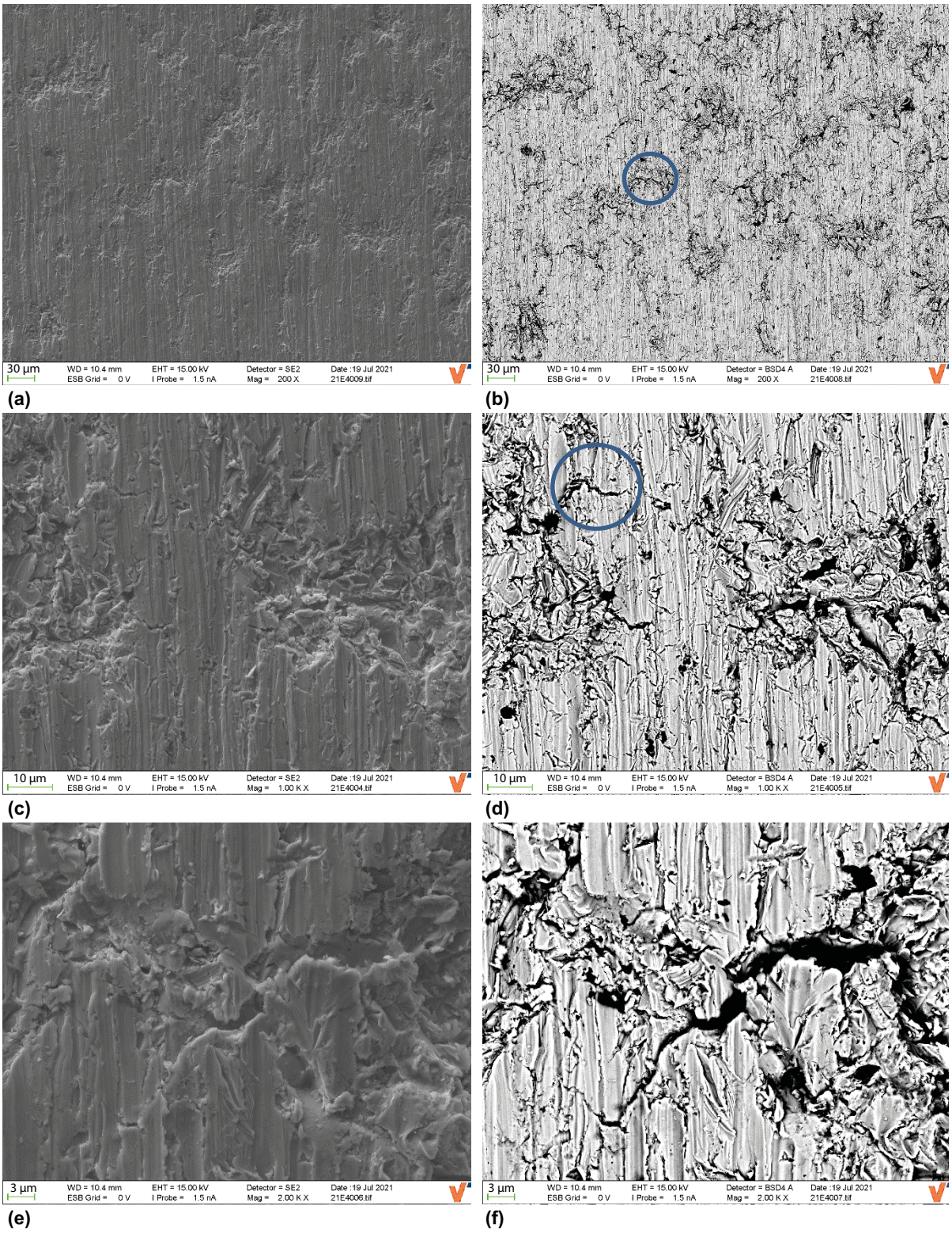

Figure 5-42. *Matching pairs of (a,c,e) secondary electron and (b,d,f) backscatter electron (topography) SEM micrography of the sample surface after testing in air. In addition to grinding and polishing marking (1200 grit SiC), crater/pit-like features can be observed. Backscatter electron (topography) imaging mode reveals what appear to be crack like features, perpendicular to the loading direction, extending from the crater/pit-like features.*

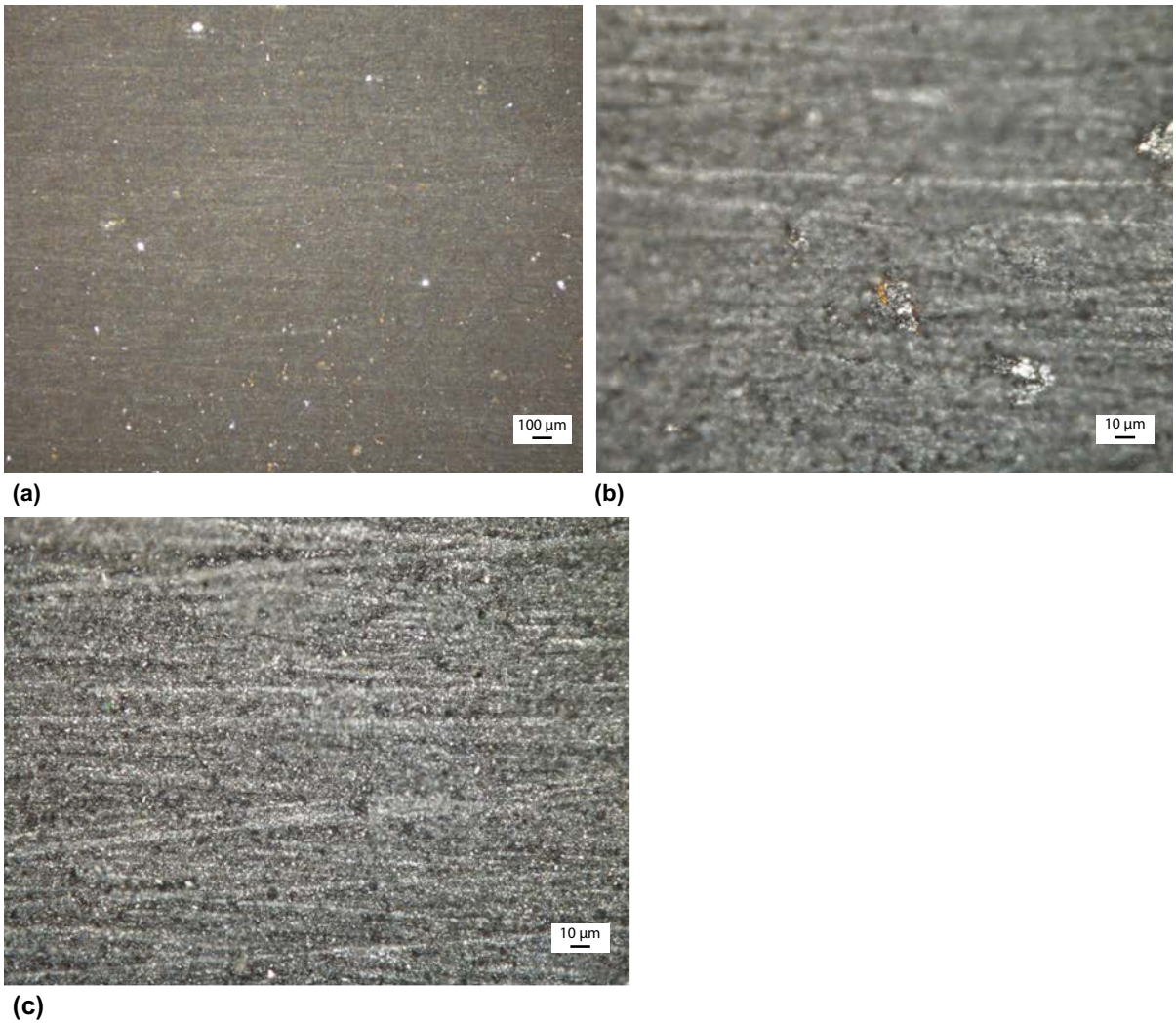

Figure 5-43. *Stereo microscope images of the sample surface after testing in environment. In addition to grinding and polishing markings (1200 grit SiC), some crater/pit-like features can be observed.*

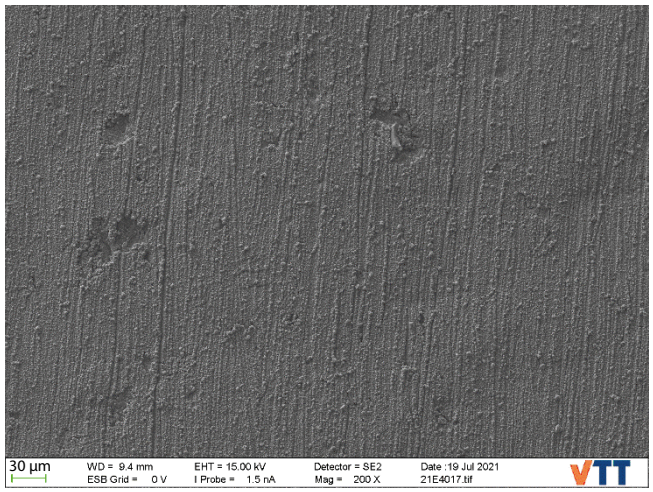

(a)

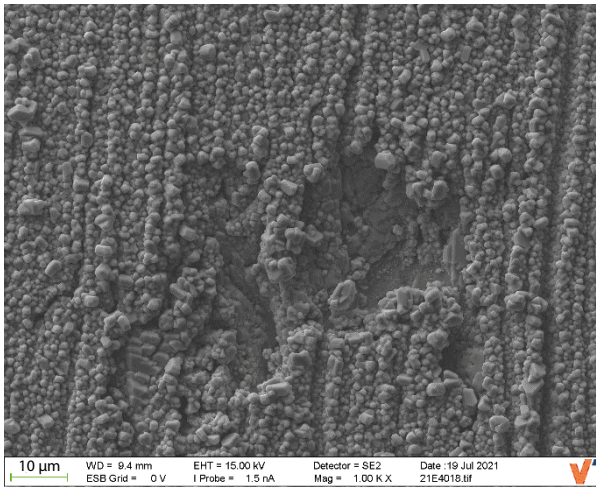

(b)

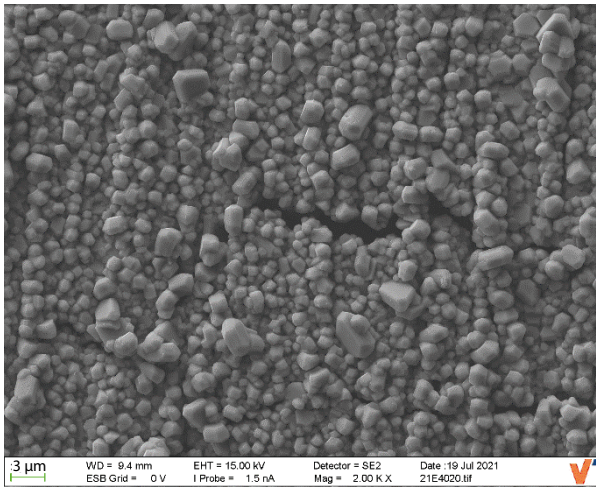

(c)

Figure 5-44. *Secondary electron SEM micrographs of the surface of the specimen tested in a sulphur containing environment. The surface is covered in a layer of crystallites. Nonetheless, indications of the grinding and polishing markings and direction are still visible. Several crater/pit-like features were observed on the surface. A higher magnification image of one of these features is shown in (b). In addition, several crack-like features were observed like shown in (c).*

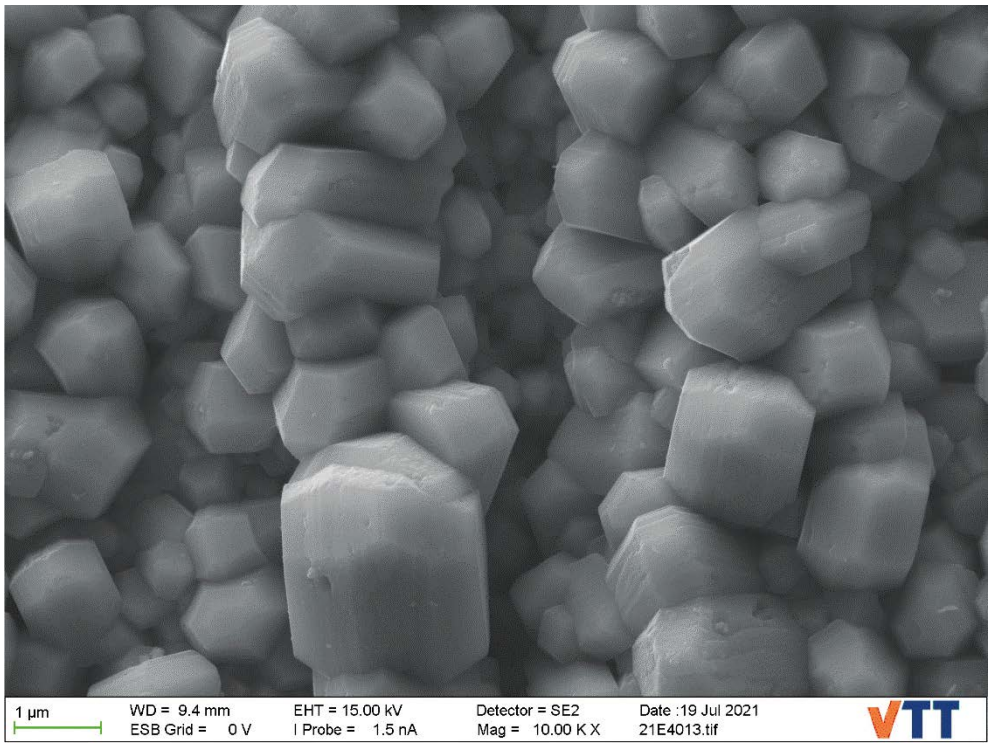

Figure 5-45. *Secondary electron SEM micrograph of the crystallites present on the surface of the specimen. Crystallite sizes range on the order on hundreds of nanometres to approximately 1–2 µm.*

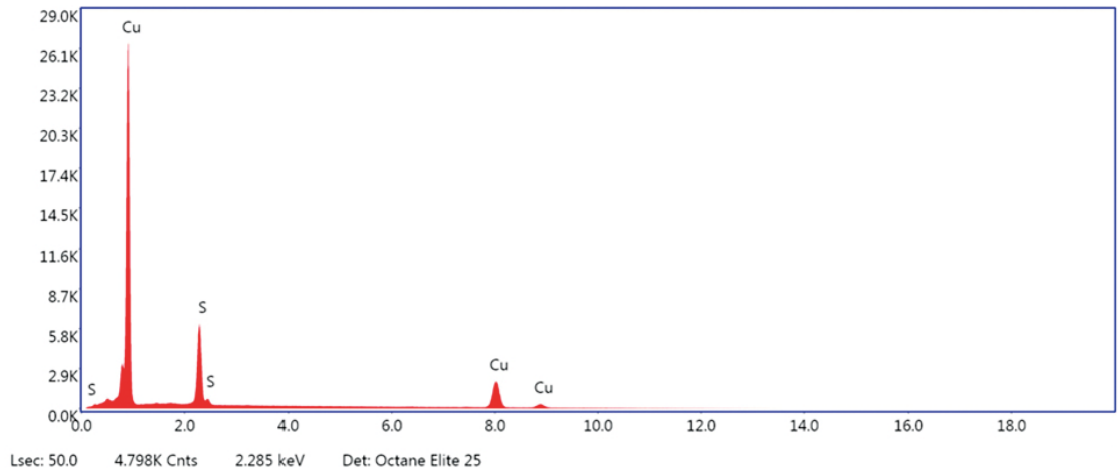

Element	Weight %	Atomic %
O	1.15	3.82
S	19.05	31.34
Cu	80.38	66.76

Figure 5-46. *Representative semi-quantitative SEM-EDS spectra the copper and sulphur rich scale on the surface of the specimen tested in a sulphur containing environment.*

5.2.3 Nanohardness measurements

Nanohardness was measured on cross-sections of three samples, one untested, one tested in air for 72 hrs (to a strain of about 8 %) and one tested in water with sulphide (25 mg/l) for about 46 hrs (to a strain of about 8 %). Three hardness profiles were measured on each specimen, with 4µm spacing (from the surface), Figure 5-47. The hardness profiles are shown in Figure 5-48. All samples showed a hardened surface up to about 20 µm distance from the surface. No clear differences between the three conditions could be observed (Figure 5-48).

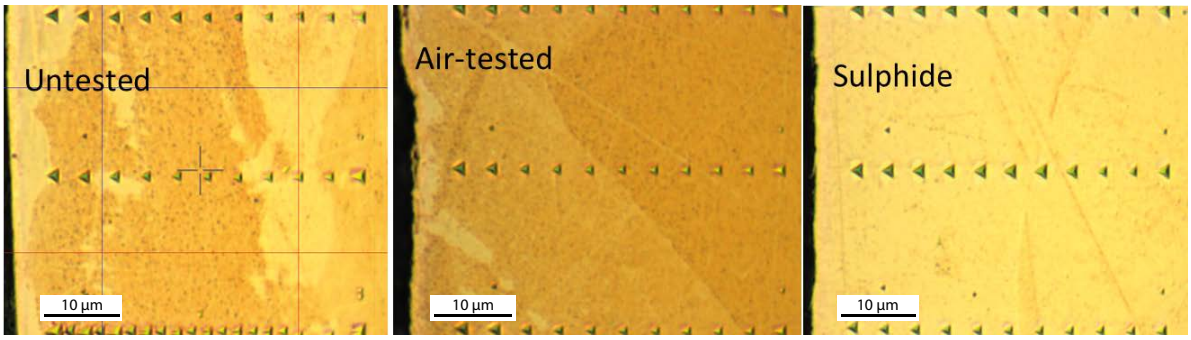

Figure 5-47. *Nano-indentation marks on the sample surfaces, three sequences on each sample, 4 µm spacing. Note that the first point was located not exactly at 4 µm distance from the surface (due to the curviness of the surface).*

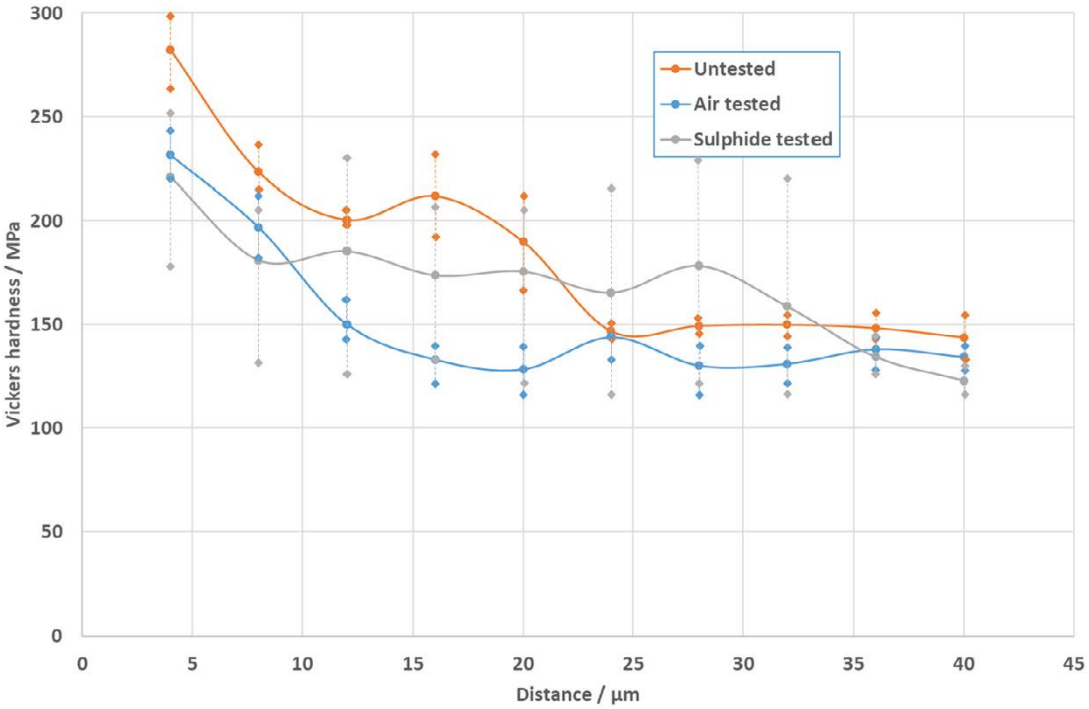

Figure 5-48. *Vickers hardness as a function of distance from the sample surface (4 µm steps), average of three measurements.*

5.2.4 Summary of surface characterizations with AFM, SEM and nanohardness

Characterization of the surface condition of three representative specimens (i) as-polished, (ii) after testing in room temperature air and (iii) after testing in a sulphide containing environment were performed via complementary techniques, including AFM, SEM and nanohardness.

Observations of the sample surface revealed a high density of crater/pit-like features that were tens of μm in diameter and several μm deep. These pits are likely formed during the EDM machining of samples. In the case of these three specimens, they do not appear to have been removed by polishing, however, it does not appear that these crater/pit like features are always present in prepared specimens; for example these features were not observed in earlier specimens, like that shown in Figure 5-49 (4b) below. Nonetheless, in the air tested specimen observed in this part of the work, cracks were observed extending from these features, which may indicate that the crater/pit-like features can act as preferential initiation sites of cracking. This highlights that it would be important to ensure that the majority of EDM defects are properly removed before testing the manufactured specimens, in addition prior to testing stereo microscopy observations should be observed to ensure a suitable surface condition.

AFM characterizations highlighted some differences in the surface conditions, particularly in between the specimen tested in a sulphur-containing environment as compared to as-polished or air tested specimens. The normalized surface area increases after testing in a sulphur-containing environment. This is due to the development of the Cu_2S crystallite scale on the sample surface. The Cu_2S crystallite scale forms over the entire exposed surface, and some evidence of the underlying polishing striations can be observed (in the form of a general waviness of the scale). Crystallite diameters range from on the order of several hundred nanometres to several μm.

Nanohardness measurements showed a hardened surface up to about 20 μm depth. No clear differences between the three conditions could be observed

5.3 SEM imaging of creep specimens

The samples studied are described in Table 5-5 below. Here “Creep test Nr” refers to the sample code in Section 5.1 above.

5.3.1 SEM of surfaces prior to sulphide film removal

Table 5-5. The SEM samples studied.

Number	History
1	Creep test Nr 1; 1 M NaNO2, creep stabilisation (to about 8 % strain) followed by a series of polarisations, fractured (during open circuit monitoring) by SCC after about 31 hrs from initial loading
2	Creep test Nr 3; creep stabilisation in water (to about 8 % strain), sulphide exposure at 25–30 mg/l for 29 hrs (anodic polarisation for 1 hr to +1 mA/cm^2 at about 19–20 hrs into the sulphide feed), test continued without sulphide feed for about 60 hrs
3	Creep test Nr 4; creep stabilisation in water (to about 8 % strain), sulphide exposure at 25–30 mg/l for 25 hrs, test continued without sulphide feed for about 120 hrs
4	Creep test Nr 8. Tested in air until creep stabilisation (to about 8 % strain). T = 21±1 °C, RH = 28 to 35 %. Never exposed to water.
5	Creep test Nr 7; creep stabilisation in water, cathodic polarizations, anodic oxidations in the stability areas of Cu_2O and $Cu(OH)_2$

Surface appearance of the shoulder and body areas

The shoulder areas (which are supposed to be without plastic deformation) of the studied samples are shown in Figure 5-49 and the body parts in Figure 5-50. At the shoulder area outer surface of all specimens, machining marks with occasional surface defects were observed. The surface defect

on the specimen number 4 (creep test sample 8, which was only tested in air) was particularly clear (Figure 5-49; Picture 4b).

The surface appearance of the body areas (which were plastically deformed up to about 8 % strain) are shown in Figure 5-50. SCC cracks were observed on the body part of the SEM sample 1, exposed to 1M $NaNO_2$. There is a radical difference in the surface appearance of SEM samples 2 and 3 at the body part. SEM shows a very different surface appearance with lots of apparently deposited crystals in case of SEM sample 3 and no such crystals in case of SEM sample 2. The difference is most likely due to the anodic polarisation (dissolution) towards the end of sulphide exposure part of creep experiment 2. For SEM specimen 4, similar clear surface defects can be observed at the body part as in the shoulder area.

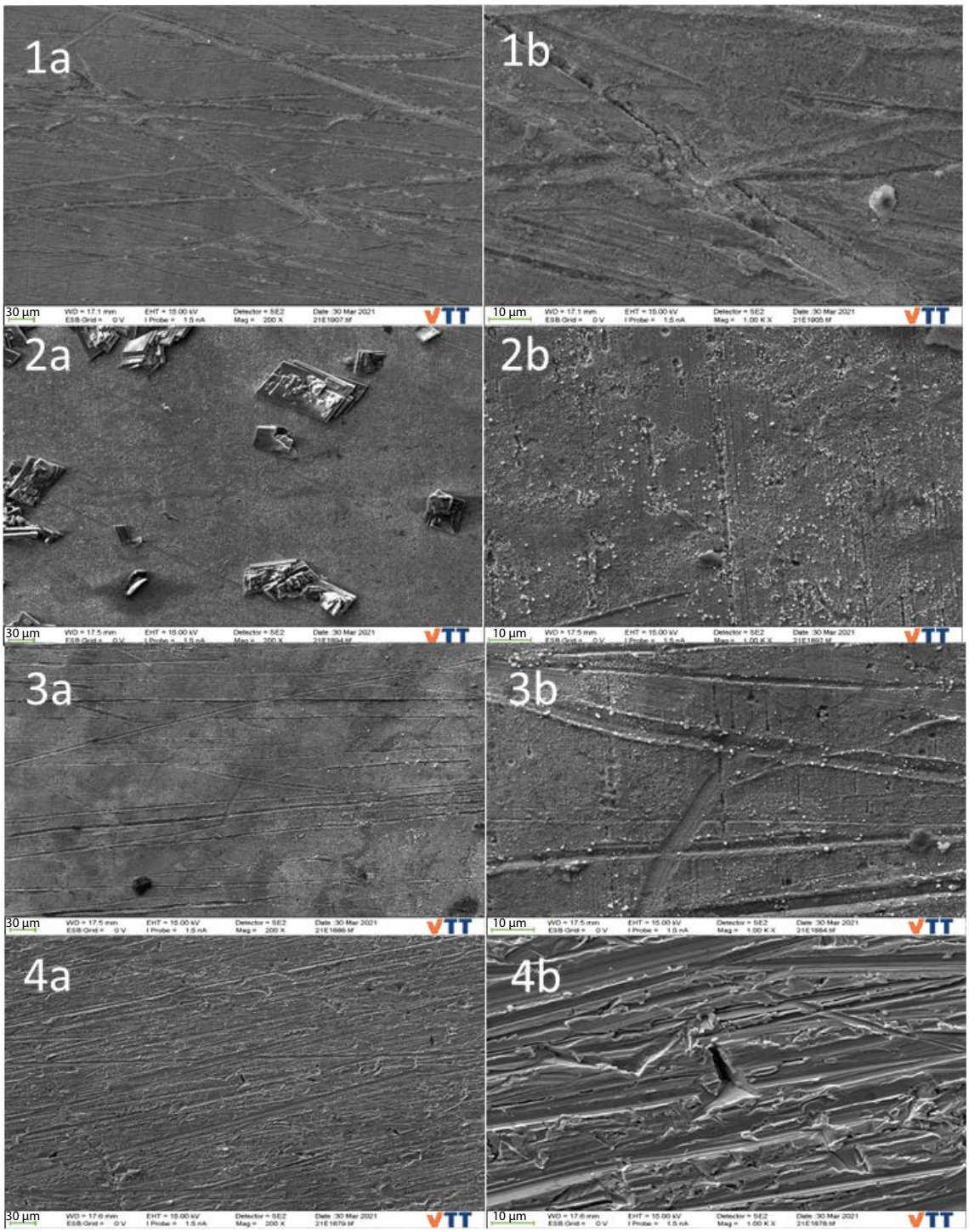

Figure 5-49. *Surface appearance of the shoulder area of SEM samples 1 to 4. The green scale line at the lower corner is 30 µm for pictures 1a to 4a and 10 µm for pictures 1b to 4b.*

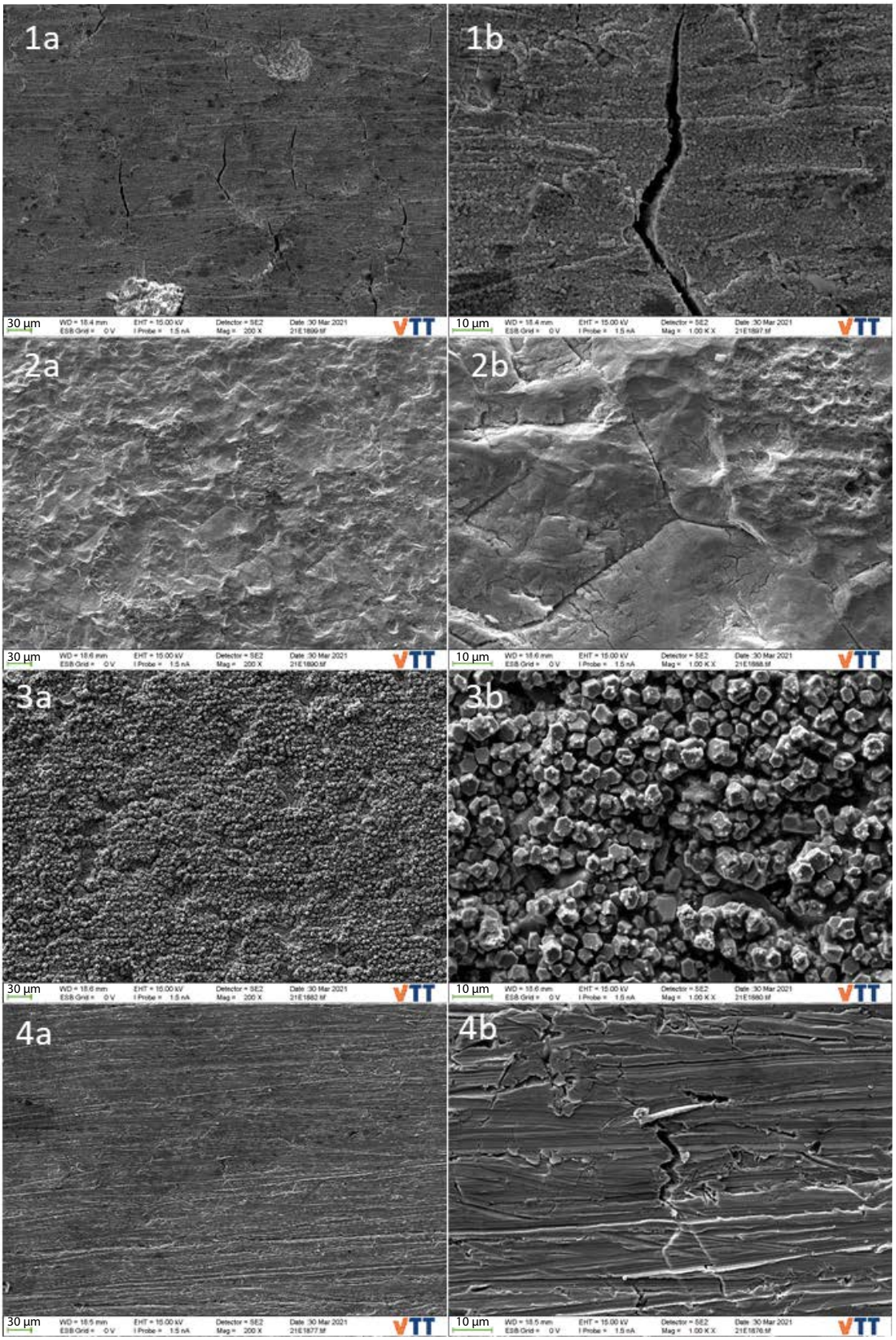

Figure 5-50. *Surface appearance of the body area of SEM samples 1 to 4. The green scale line at the lower corner is 30 µm for pictures 1a to 4a and 10 µm for pictures 1b to 4b.*

SEM sample 1 (creep experiment 1, 1 M $NaNO_2$)

No further EDS – studies of the external surfaces were considered necessary for this sample at this point.

SEM sample 2 (creep experiment 3, sulphide with anodic polarisation)

The general EDS surface area analysis (Figure 5-51) detected mostly Cu and O, with only about 7 a% S. Phosphorus (P), found at a concentration of about 1.5 a%, most likely originates from the buffer solution used. Note that the expected percentage of S in Cu_2S is 33 a%. The distribution of elements seems to be rather even.

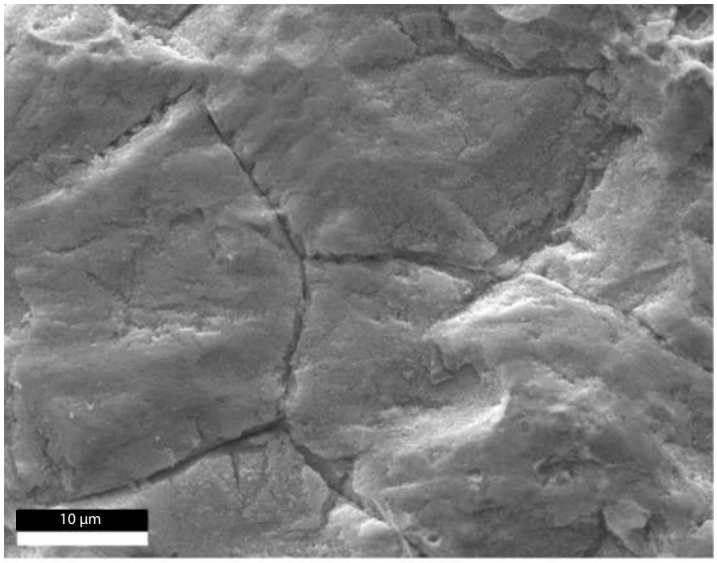

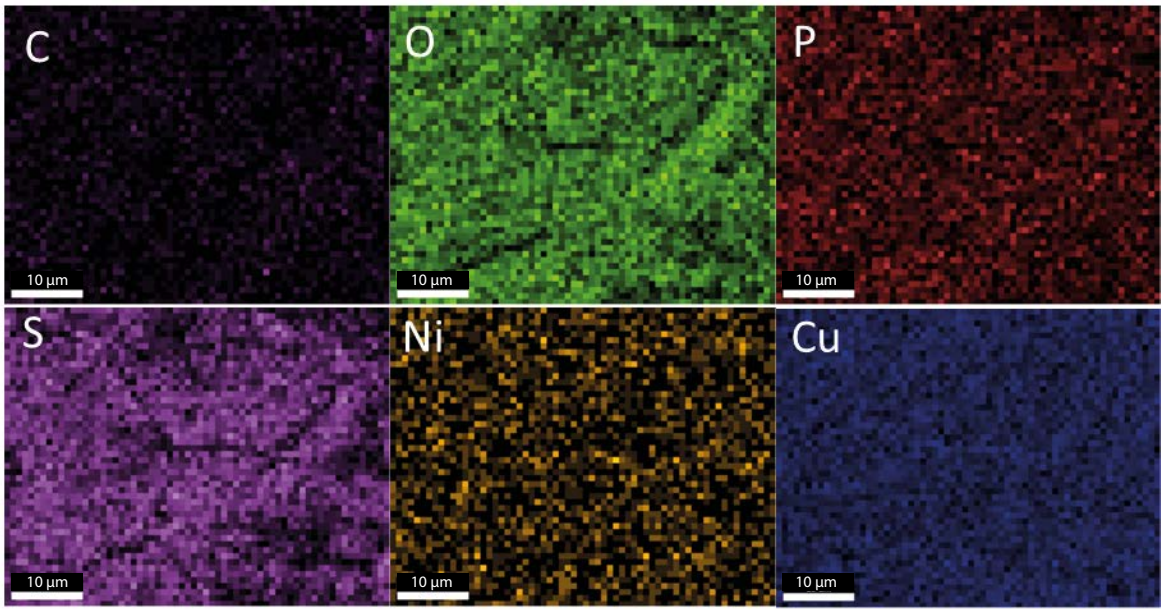

Element	Weight %	Atomic %
C	0.36	1.56
O	5.29	17.15
P	0.90	1.50
S	4.34	7.02
Ni	0.62	0.55
Cu	88.49	72.22

Figure 5-51. *EDS area analyses of the surface of the body of SEM sample 2.*

EDS spot analysis 1–3 (Figure 5-52) on the body part outer surface show very similar chemical compositions, mainly Cu and O, with some S (~9 a%) and a trace of P (~1.5 a%). Potential grain boundary attack was also observed.

EDS spot analysis 1–3 (Figure 5-53) on the particles at the potential grain boundary attack location show very similar chemical compositions, mainly Cu and O, with S (~20 a%) and P (~4 a%). The atomic percentage of S and P at such locations were much higher than that on the general outer surface.

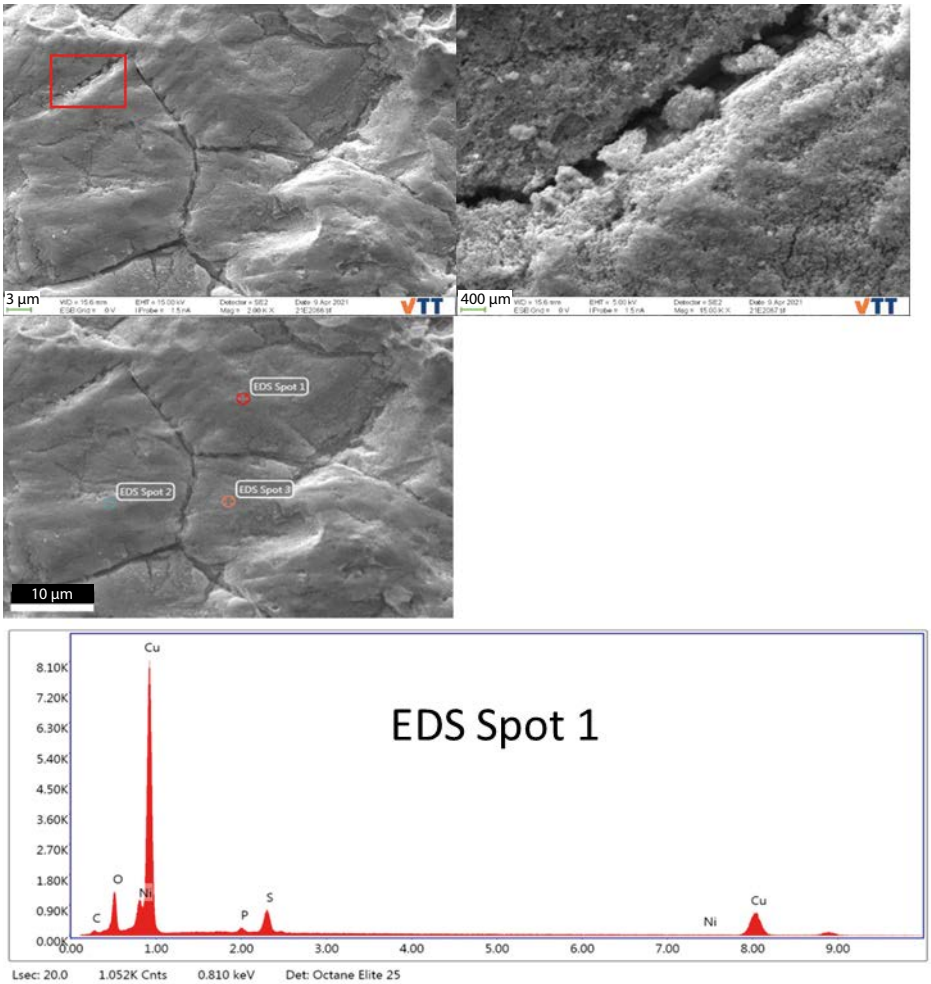

Element	Weight %	Atomic %
C	1.39	5.37
O	8.30	24.00
Ni	4.47	3.52
P	1.20	1.79
S	5.19	7.49
Cu	79.45	57.84

Figure 5-52. *EDS spot analyses of the surface of the body of SEM sample 2. Note: the additional (not marked) small peak at about 8.9 keV is due to Cu-Kβ, which is so close to Os-Lα that sometimes EDS is not able to discern between the two peaks.*

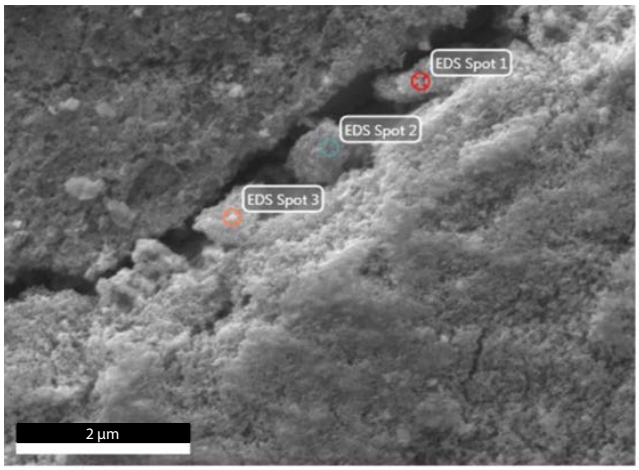

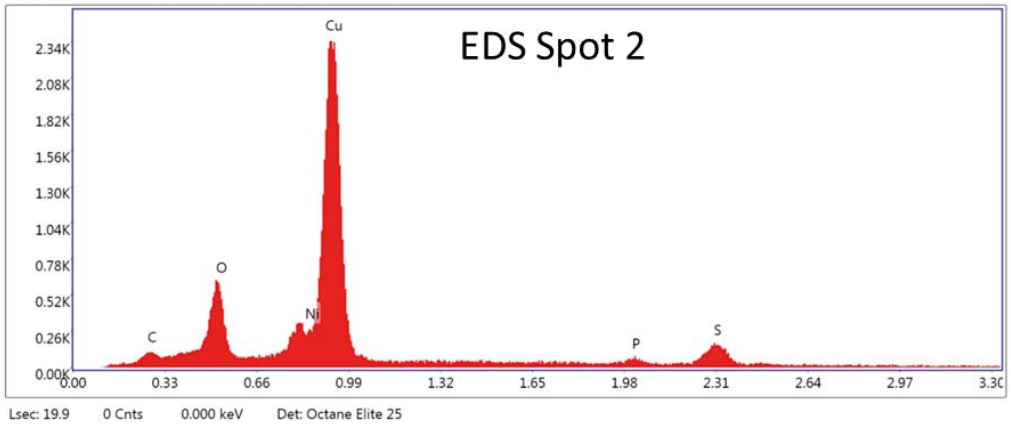

Element	Weight %	Atomic %
C	1.40	5.03
O	7.76	20.90
P	3.04	4.23
S	15.14	20.35
Ni	3.66	2.69
Cu	69.00	46.80

Figure 5-53. *EDS spot analyses of a particle (EDS Spot 2) located in the potential boundary attack location on the surface of the body of SEM sample 2.*

SEM sample 3 (creep experiment 4, sulphide)

Figure 5-54 shows low and high kV SEM images of the same area on SEM sample 3 (body part). High voltage mode is more sensitive to chemical composition difference (chemical contrast) while low voltage mode is more sensitive to surface layer topography (surface morphology contrast). The surface film consists of hexagonal crystals (probably deposited) and amorphous-like structure on the bottom.

The hexagonal crystals mainly consist of Cu-S-O and the amorphous-like crystals mainly consist of Na-P-O (Figure 5-55). The sulphur concentration of the surface area on average is almost 30 a%. The buffer solution used is obviously the source of Na. Confirmation with EDS at higher magnification is shown in Figure 5-56. The hexagonal crystals seem to be almost exclusively of Cu and S (probably Cu_2S), with only a small amount of O.

The difference in the film morphology and structure between SEM samples 2 and 3 most probably stems from the anodic dissolution (+1 mA/cm^2) during the sulphide feed of creep experimen 2, which has led to the dissolution and reduction of the deposited crystals.

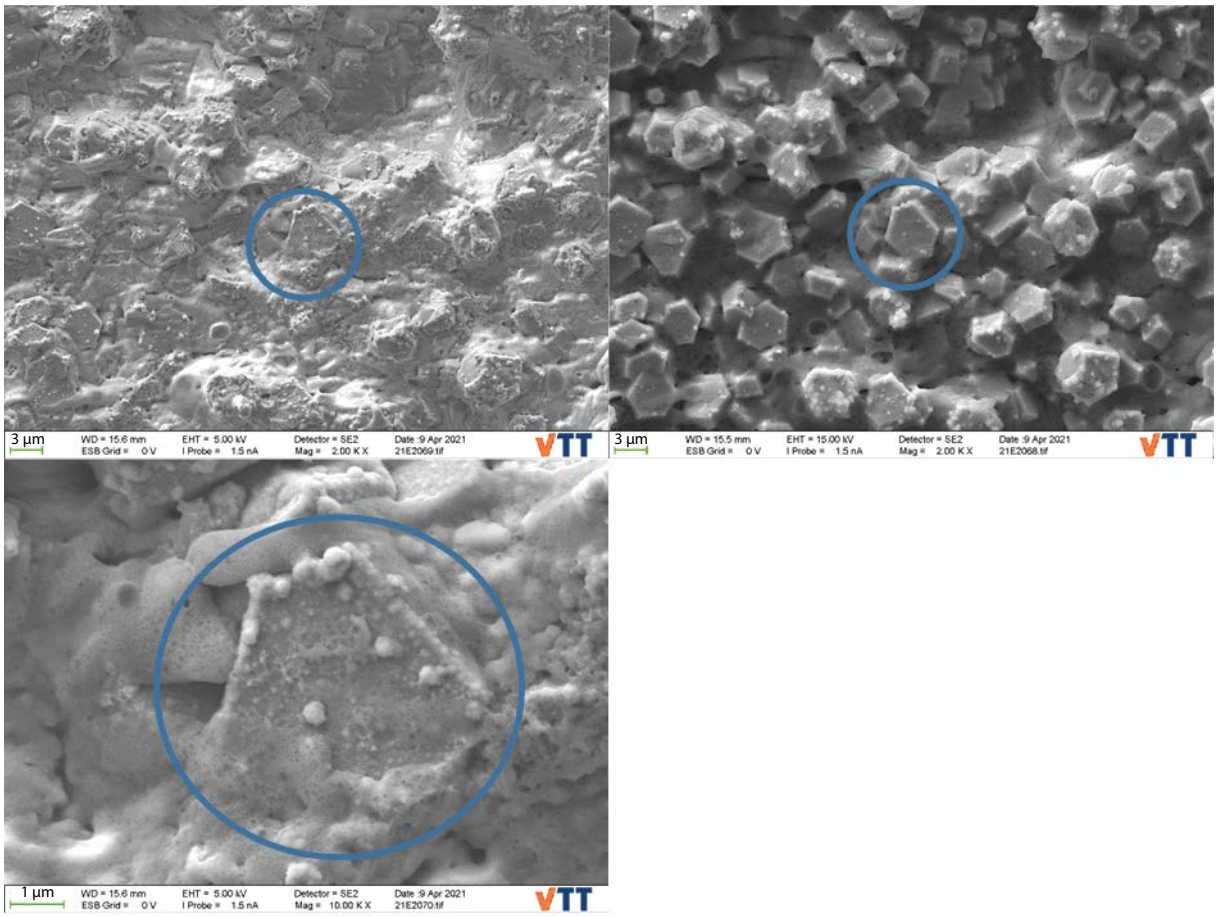

Figure 5-54. *Surface morphology of SEM sample 3. Upper left 5 kV and upper right 15 kV SEM picture of the same area. The blue circles depict one hexagonal crystal which was further analysed (Figure 5-56).*

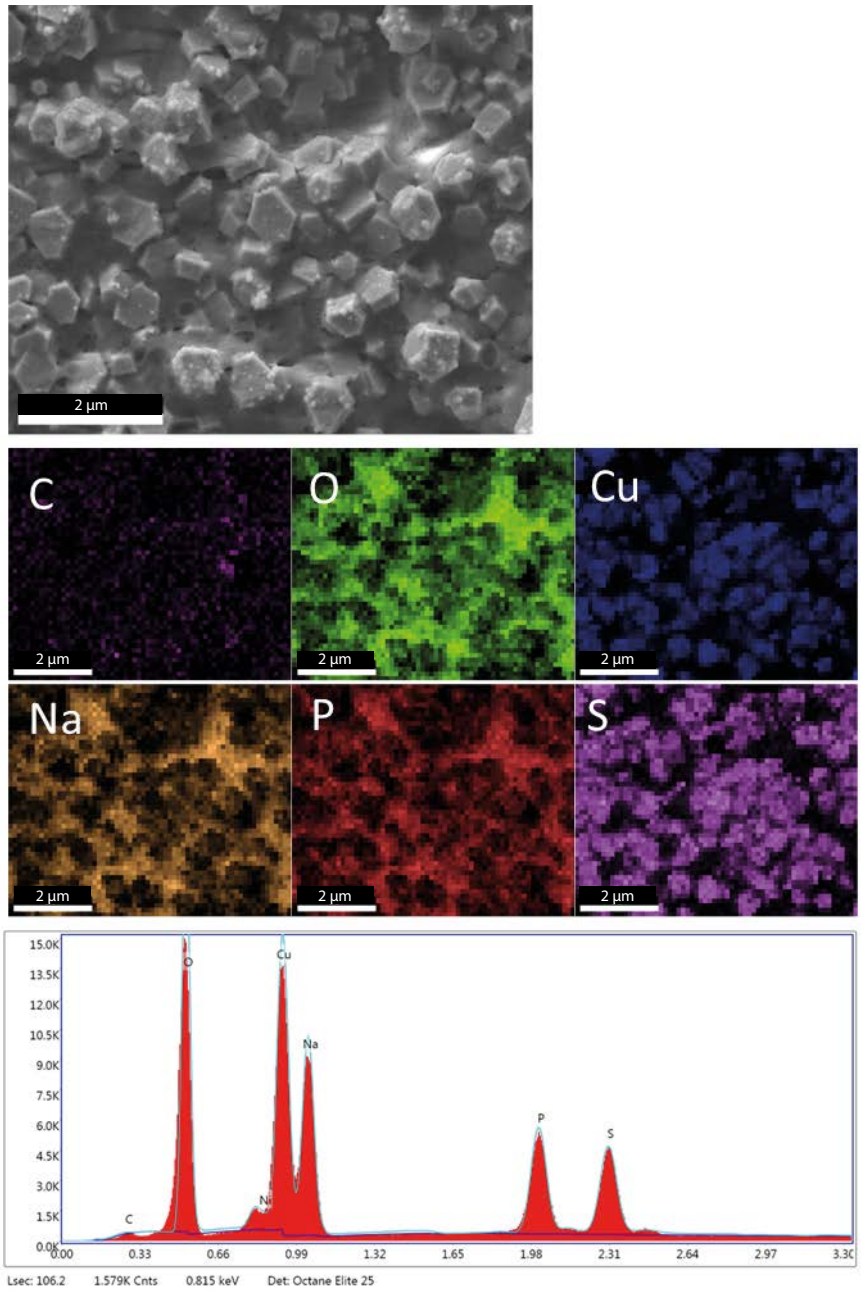

Element	Weight %	Atomic %
C	0.48	1.16
O	11.52	20.72
P	29.49	27.40
S	33.14	29.74
Cu	13.48	6.11
Na	11.88	14.87

Figure 5-55. *EDS surface area analysis of SEM sample 3.*

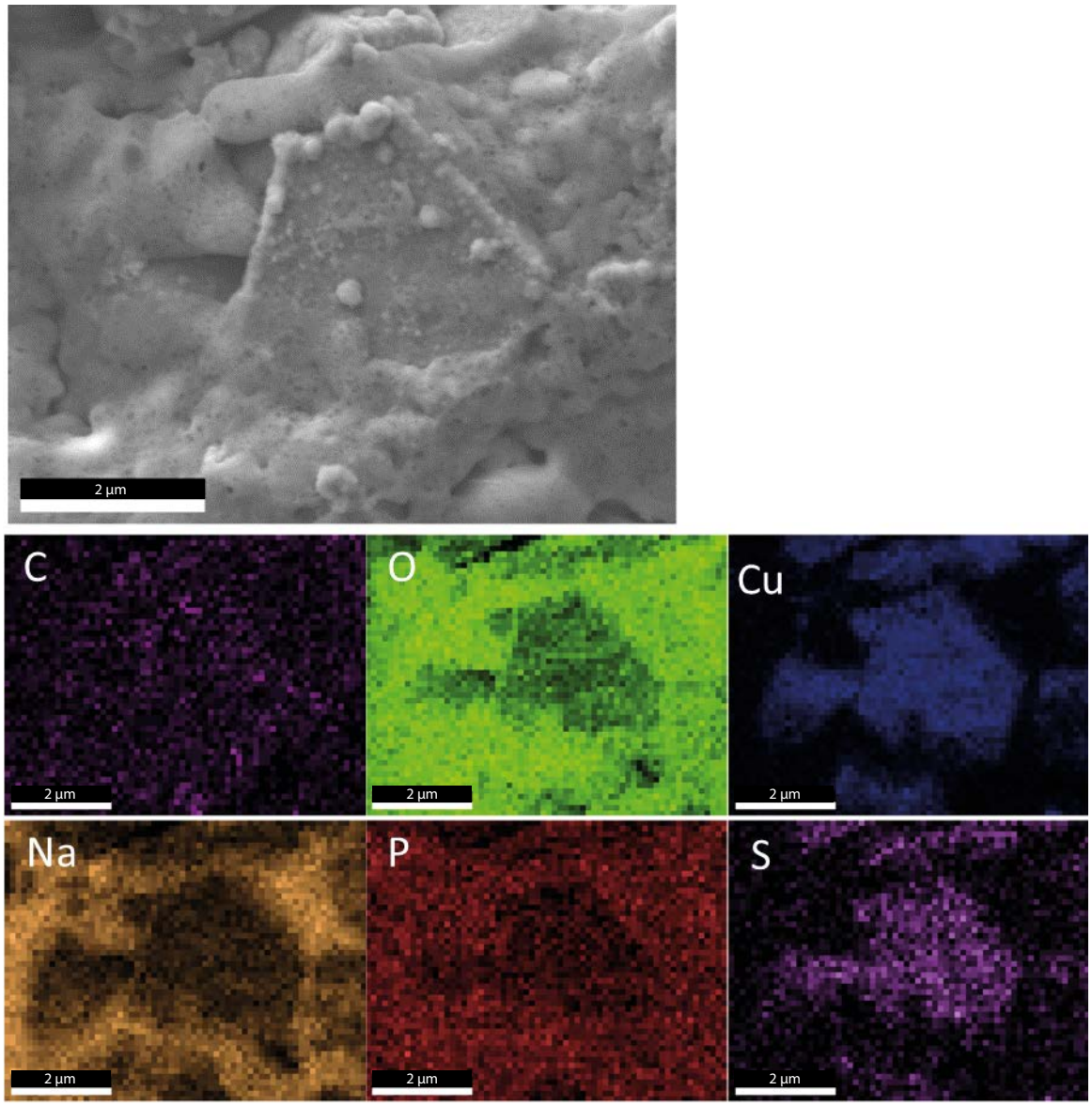

Figure 5-56. *EDS surface area analysis of sample 3, focused on one hexagonal crystal.*

SEM sample 4 (creep experiment Nr 8 tested in air)

No further EDS – studies of the external surfaces were considered necessary for this sample at this point.

5.3.2 SEM cross sections prior to sulphide film removal

The shoulder areas only revealed some machining marks without significant defects (Figure 5-57).

SEM sample 1 (creep experiment 1, 1 M $NaNO_2$)

Numerous cracks were found in the cross section, Figure 5-58. Clear matrix dissolution and oxidation along the SCC cracking path was observed. There are SCC cracks in both TG and IG mode (BSE images), which are in accordance with the fracture surface observation (Figure 5-59). The oxygen content in the oxide layer has a depletion area in the middle of the oxide layer and an enriched oxygen layer, which can be seen at the boundary of surface oxide layer and the base material. The enriched oxygen layer at the lower bound can be clearly observed as oxides in the low-kV SE images. These oxides were not from the polishing suspension since no Si signal was detected.

The oxygen enriched layer at the oxide-base metal interface showed that particles in this area comprise mainly of Cu and O with also some S, Figure 5-61. The enriched oxygen layer at the interface between the matrix and the oxide film was analyzed with the low-kV SE images and low kV EDS points analysis, which indicate the enriched O layer was formed by Cu-O-S crystallites with dimensions of 100–300 nm, Figure 5-62. The presence of these crystallites within a specified region suggests involvement of a diffusion process facilitated by the electrochemical activity at the nearby surface. Since the autoclave had not previously ever been used for studies with sulphide, the source of sulphur could not be the autoclave. Likewise, the source could not be the buffer solution used. The chemical analysis shown in Table 3-2 suggests 5.4 ppm of sulphur in the base metal. Thus, at least in principle the source of sulphur could be the base metal. It is also noteworthy here that although a similar oxygen enriched layer was seen in the specimens tested in sulphide containing environments, see e.g. Figure 5-67, no sulphur was detected in those layers. This may be because the electrolyte is different, resulting in different electrochemical reactions for the sulphide containing environments, not facilitating the formation of sulphur including crystallites. The EDS line analysis performed through the oxide layer is shown in Figure 5-63, and indicates that the oxygen depletion layer has some oxygen in it, although much less than on either sides of the depletion layer.

The surface film thickness is estimated at about 14 µm, when the oxygen enriched layer at the oxide-base metal interface is taken as the extent of the total oxide layer.

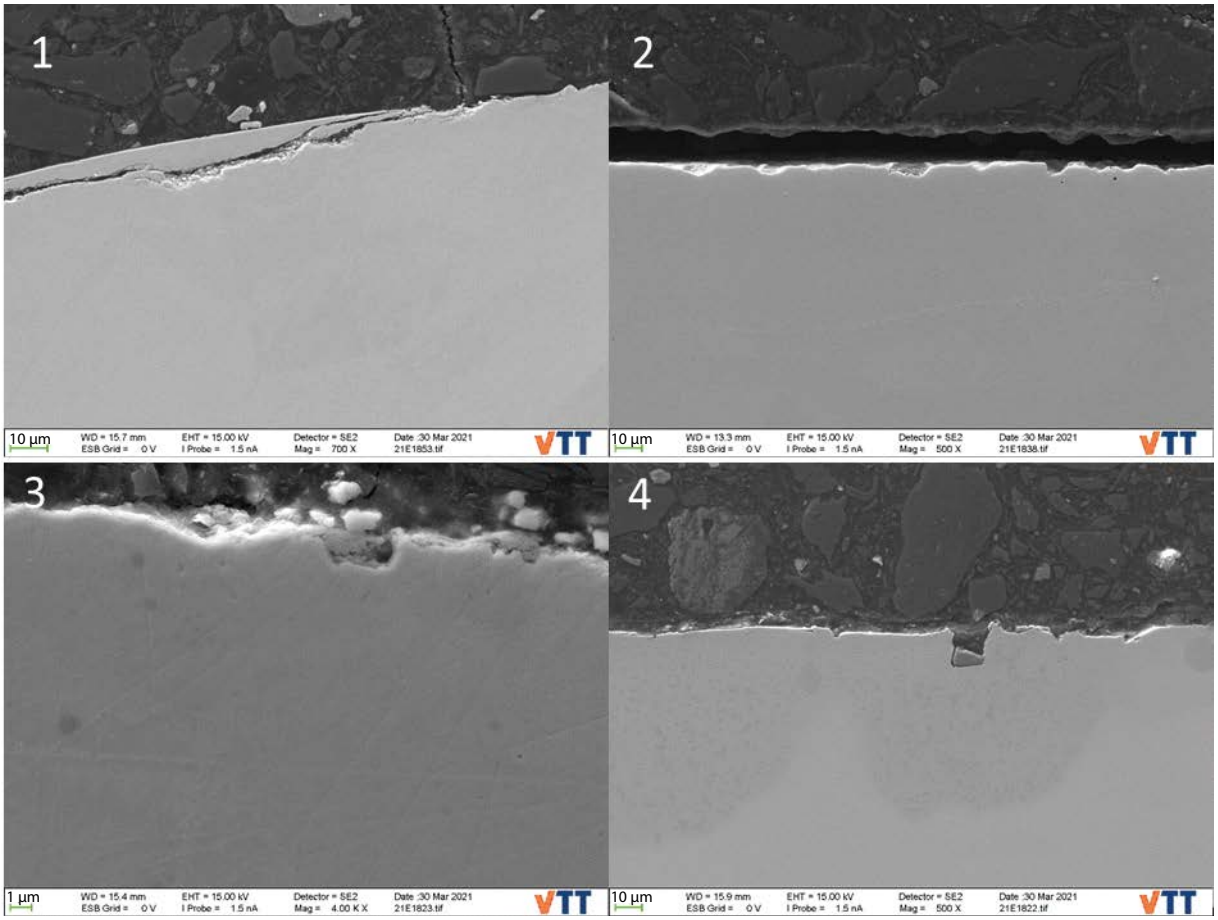

Figure 5-57. *Cross sections of the shoulder areas of SEM samples 1 to 4. Note that the scale bar on the picture of sample 3 is 1 µm, while the others are 10 µm.*

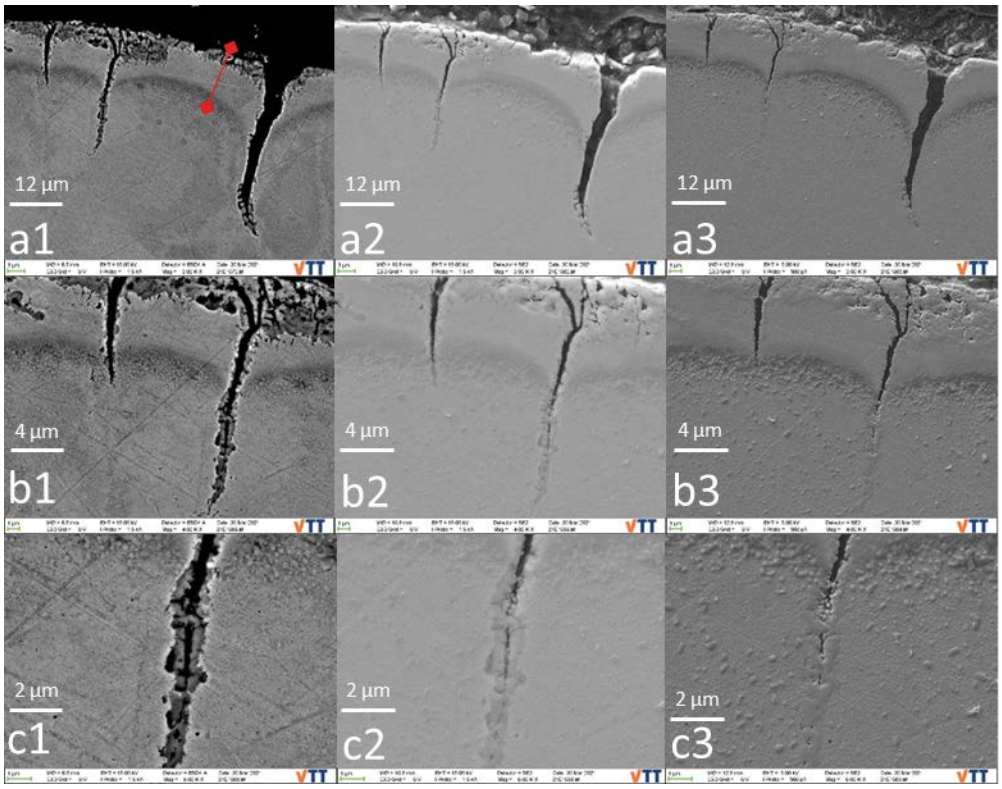

Figure 5-58. *Body part cross section from SEM sample 1: a1, b1 and c1 = BSE, a2, b2 and c2 = High voltage SE, a3, b3 and c3 = Low voltage SE. The white scale bars in the images are 3 µm. The red line depicts the oxide thickness.*

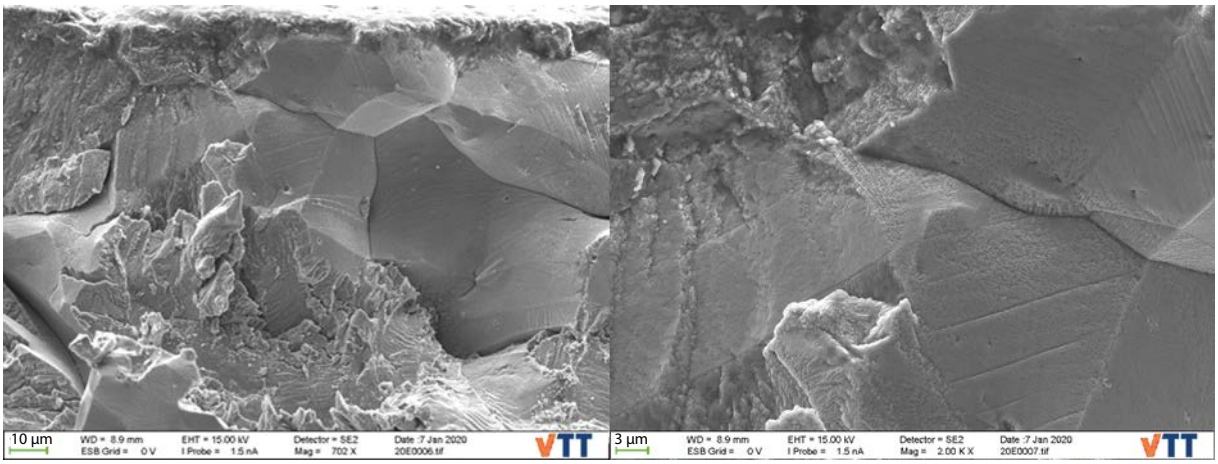

Figure 5-59. *Fracture surface appearance of SEM sample 1, both TG and IG modes of fracture are evident.*

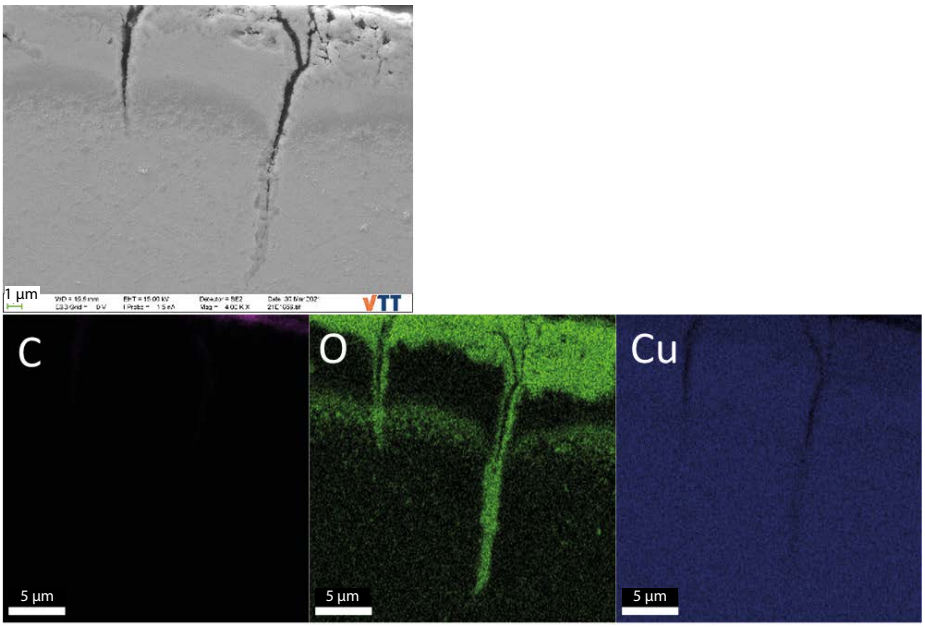

Figure 5-60. *EDS area analysis of SEM sample 1 cross section.*

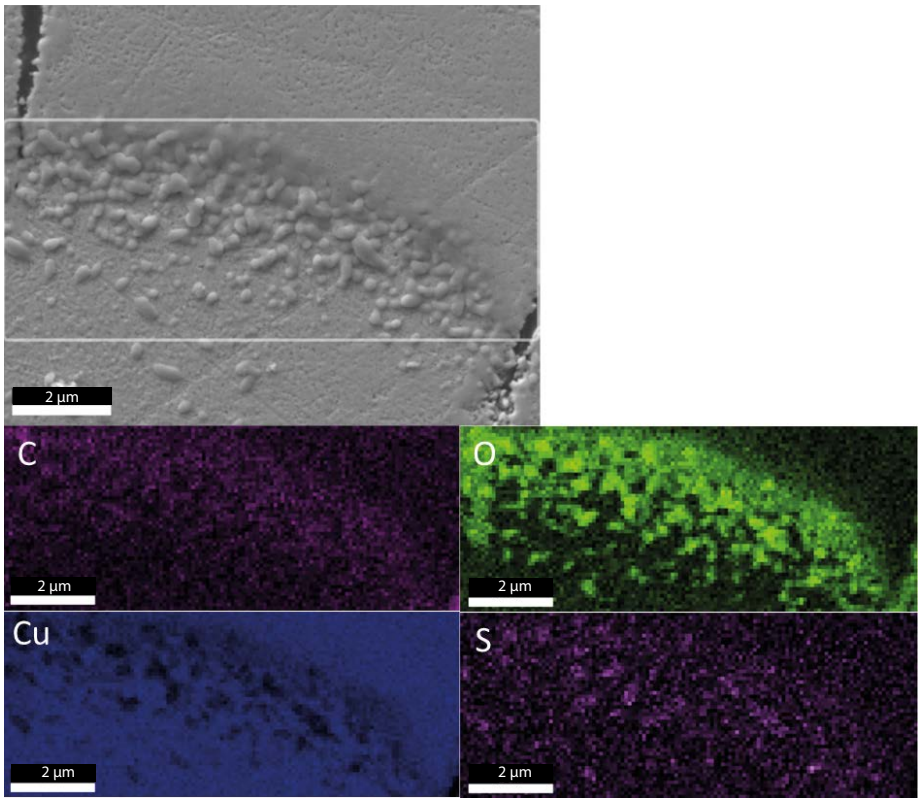

Figure 5-61. *EDS area analysis of the surface film–base metal interface. The enriched oxygen layer is formed by Cu-O-S crystals with dimension of 100–300 nm.*

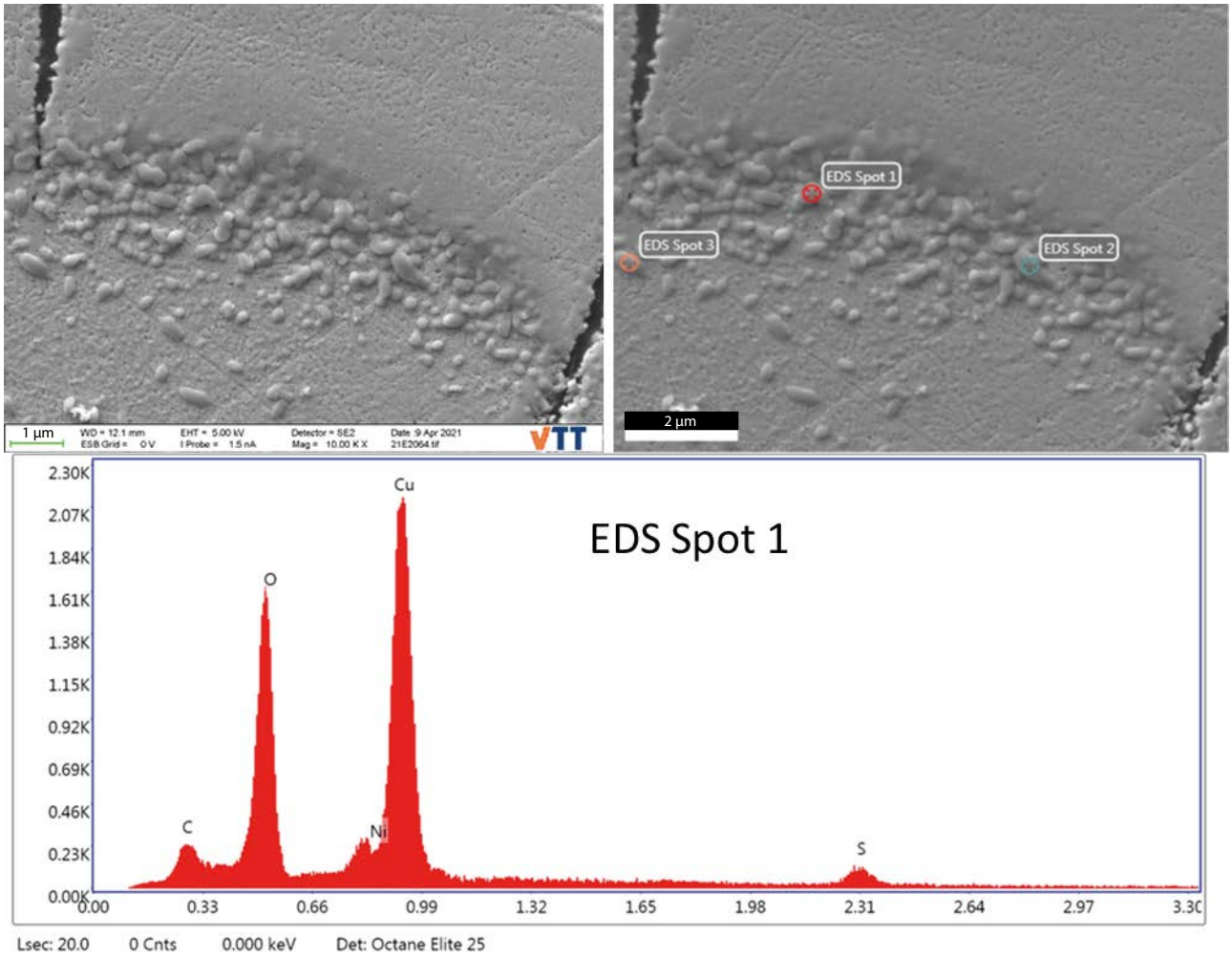

Element	Weight %	Atomic %
C	4.71	13.00
O	21.00	43.54
S	9.04	9.35
Ni	1.14	0.65
Cu	64.11	33.47

Figure 5-62. *EDS point analysis of the particles at the surface film–base metal interface.*

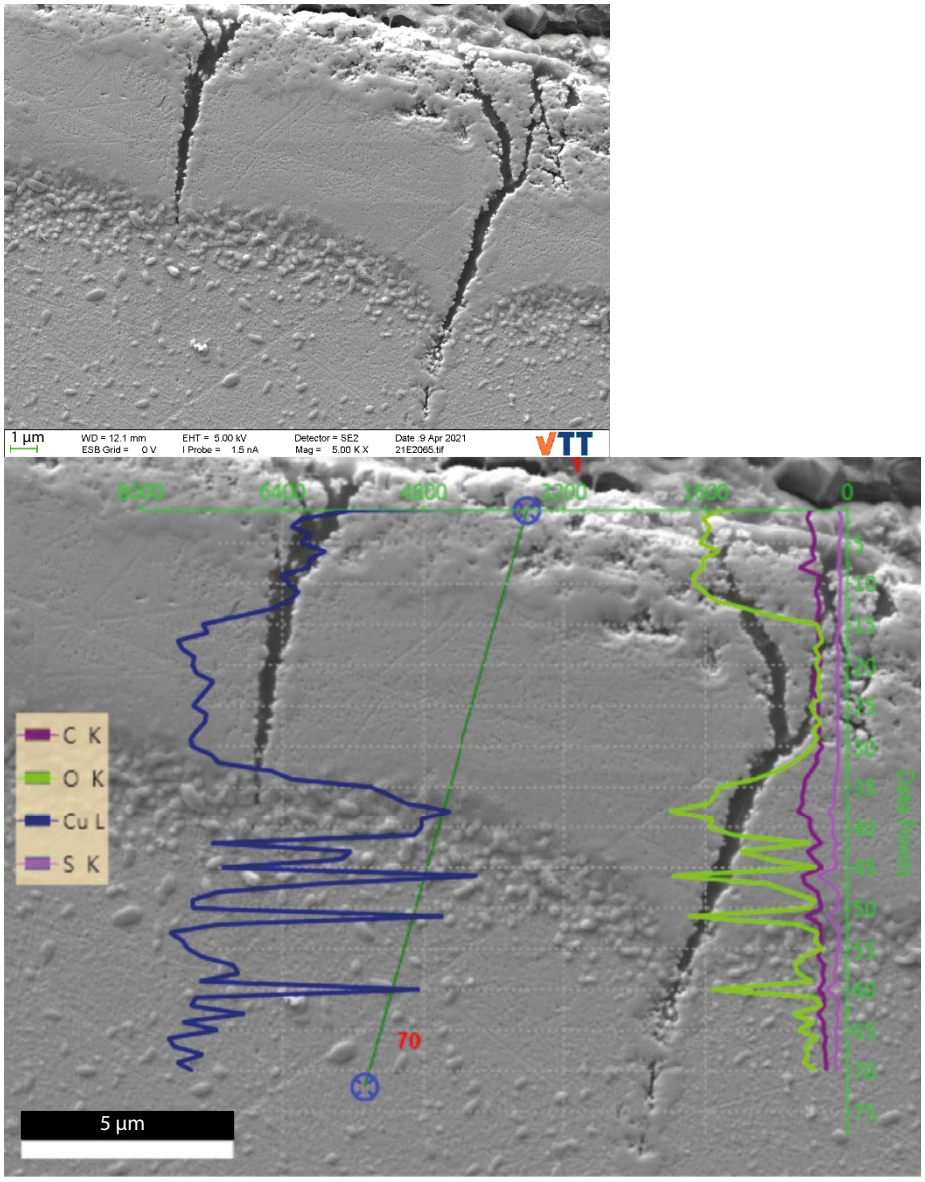

Figure 5-63. *The EDS line measurement through the surface film.*

SEM sample 2 (creep experiment 3, sulphide with anodic polarisation)

There were no surface defects extending to the base material, Figure 5-64. The defect marks detected on the surface, Figure 5-51, seem to be grooves within the surface film (such as shown in Figure 5-64). Notably, no sulphur was detected on the cross section, Figure 5-65. There seems to be a similar oxygen depleted layer within the surface film as in SEM sample 1, although not as clearly seen. The surface film thickness was estimated at 9 µm.

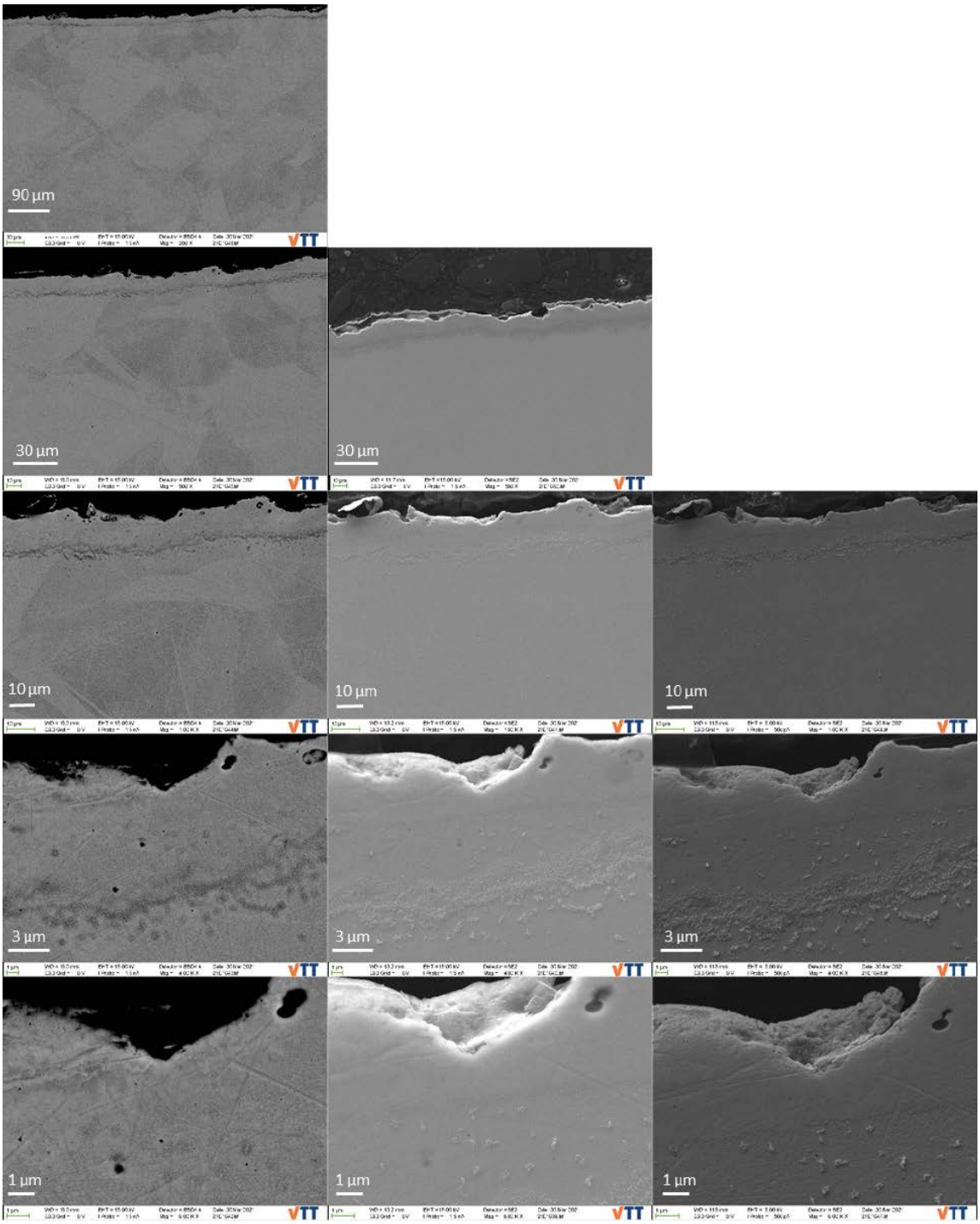

Figure 5-64. *Body part cross section of sample 2: (BSE – High voltage SE – Low voltage SE). The green scale bars: 30 µm – 10 µm – 10 µm – 1 µm – 1 µm in rows 1 to 5, respectively.*

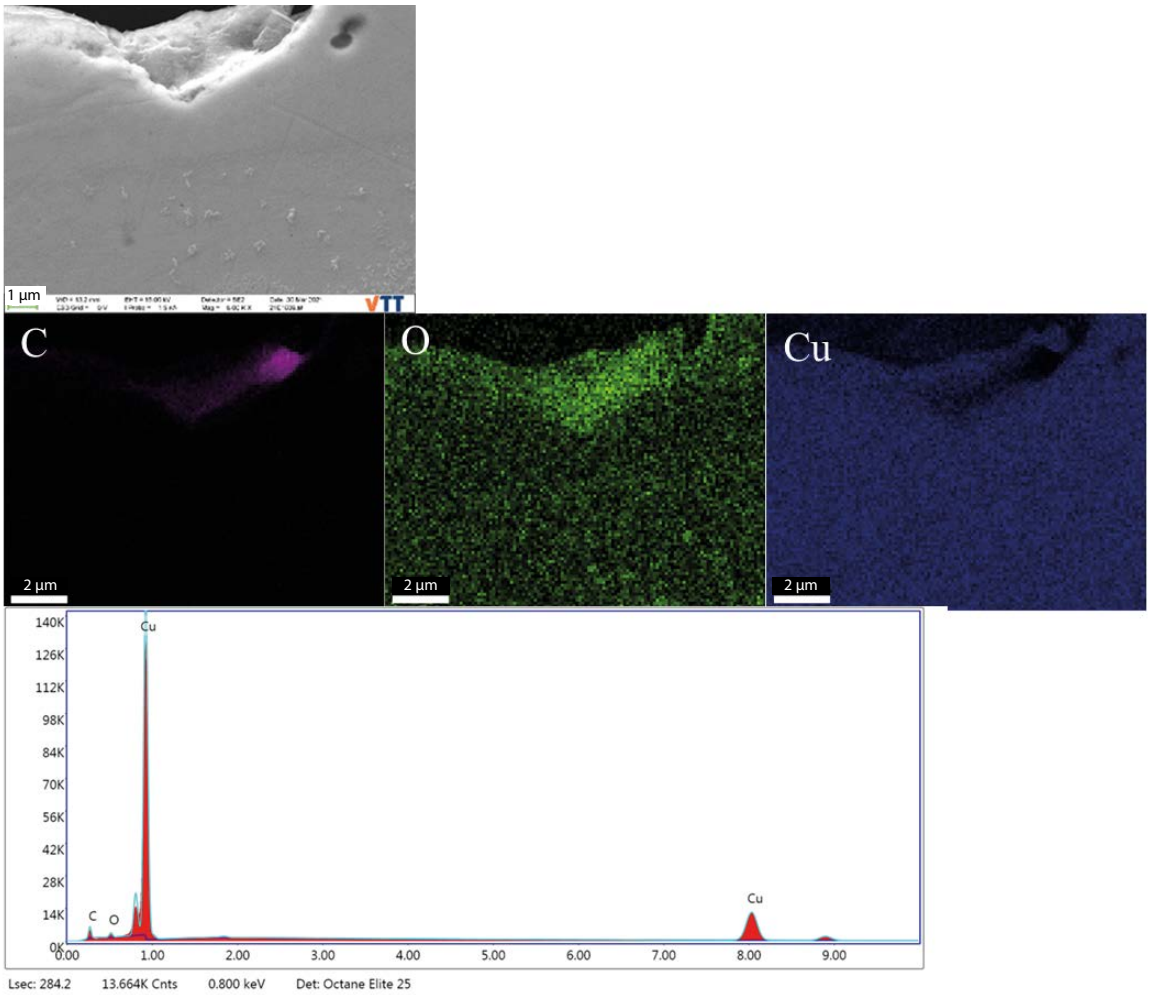

Element	Weight %	Atomic %
C	6.29	25.70
O	0.82	2.51
Cu	92.89	71.78

Figure 5-65. *EDS area analyses of the cross section of SEM sample 2.*

SEM sample 3 (creep experiment Nr 4, sulphide)

Similarly to Sample 2, there were no surface defects extending to the base material, Figure 5-66. The surface film thickness of SEM sample 3 is around 6 µm. The thickness of the surface film varied locally.

Again, EDS detected no sulphur in the surface film, Figure 5-67. This indicates that the hexagonal crystals seen on the surface (Figure 5-55, Figure 5-56), consisting of mainly Cu and S, have completely detached from the surface during preparation of the cross-section sample. The O content in the oxide layer has a depletion in the middle of the oxide layer and an enriched O layer can be seen at the boundary of surface oxide layer and the base material. The enriched O layer at the lower bound can be clearly observed as oxides in the low-kV SE images. These oxides were not from the polishing suspension since no Si signal was detected.

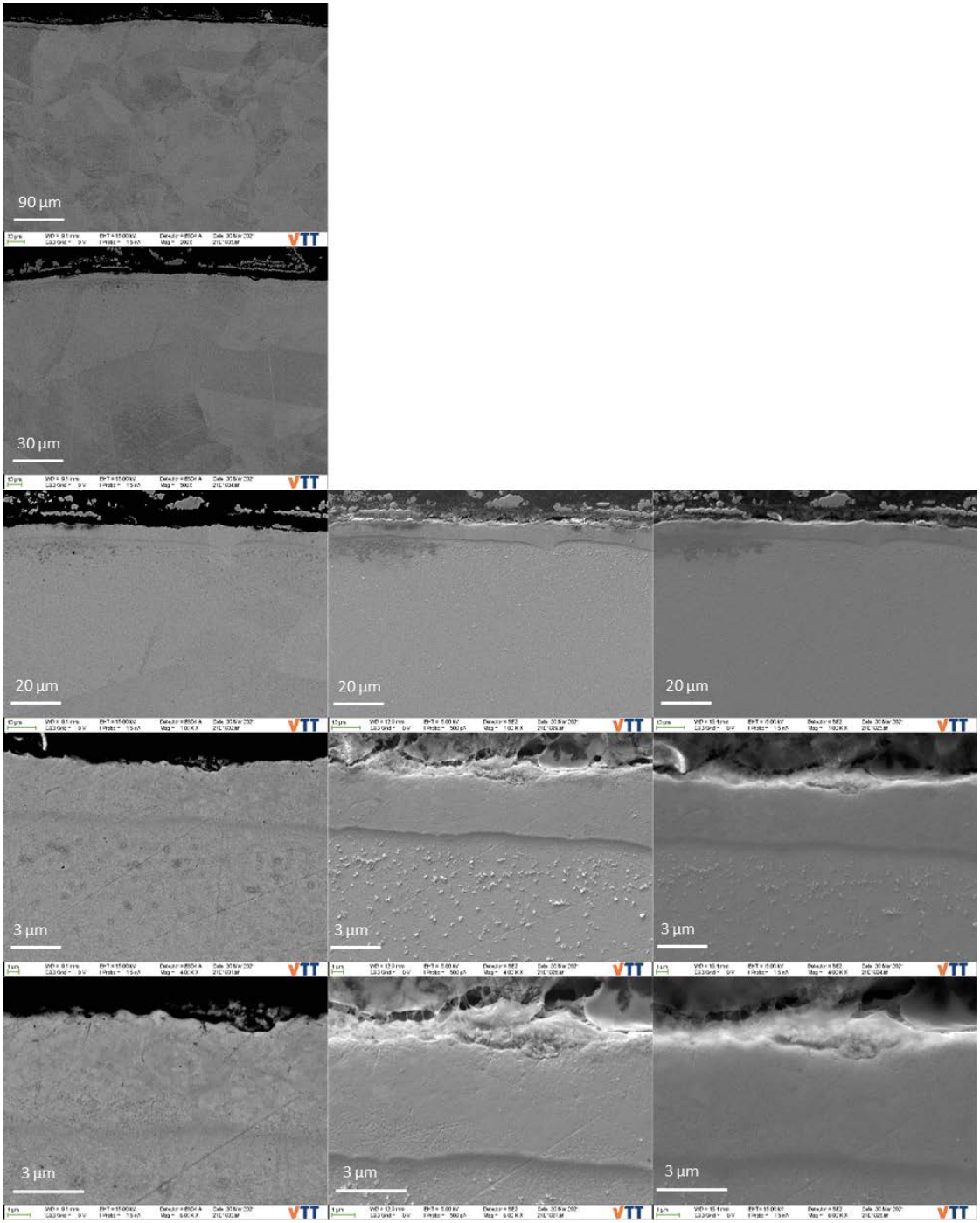

Figure 5-66. *Body part cross section of sample 3: (BSE – High voltage SE – Low voltage SE). The green scale bars: 30 µm – 10 µm – 10 µm – 1 µm – 1 µm in rows 1 to 5, respectively.*

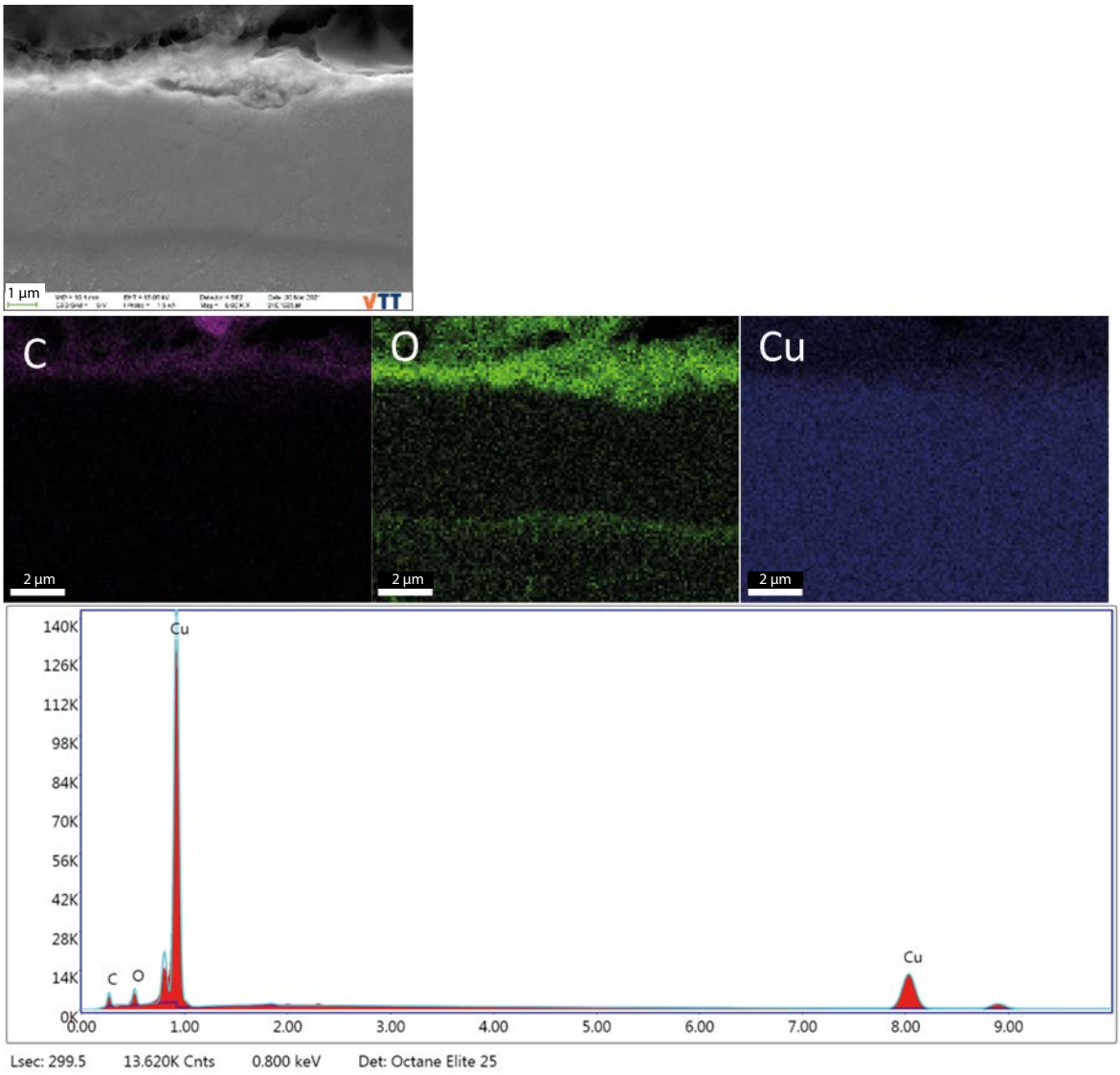

Element	Weight %	Atomic %
C	5.75	23.19
O	2.17	6.58
Cu	92.08	70.23

Figure 5-67. *EDS area analyses of cross section of SEM sample 3.*

SEM sample 4 (creep experiment Nr 8 tested in air)

The surface defects detected on SEM sample 4 (Figure 5-49, Figure 5-50) were found to extend to the base material, (Figure 5-68), in some cases showing branching of the tip. The observed small oxide particles were analysed to be SiO_2 (Figure 5-69), originating most likely from the polishing suspension.

A few inclusions were also found in the surface layer, Figure 5-70. These Si-containing inclusions are lacking of oxygen, are not SiO_2, and thus not likely coming from the polishing or surface preparation process. No surface film could be detected on SEM sample 4.

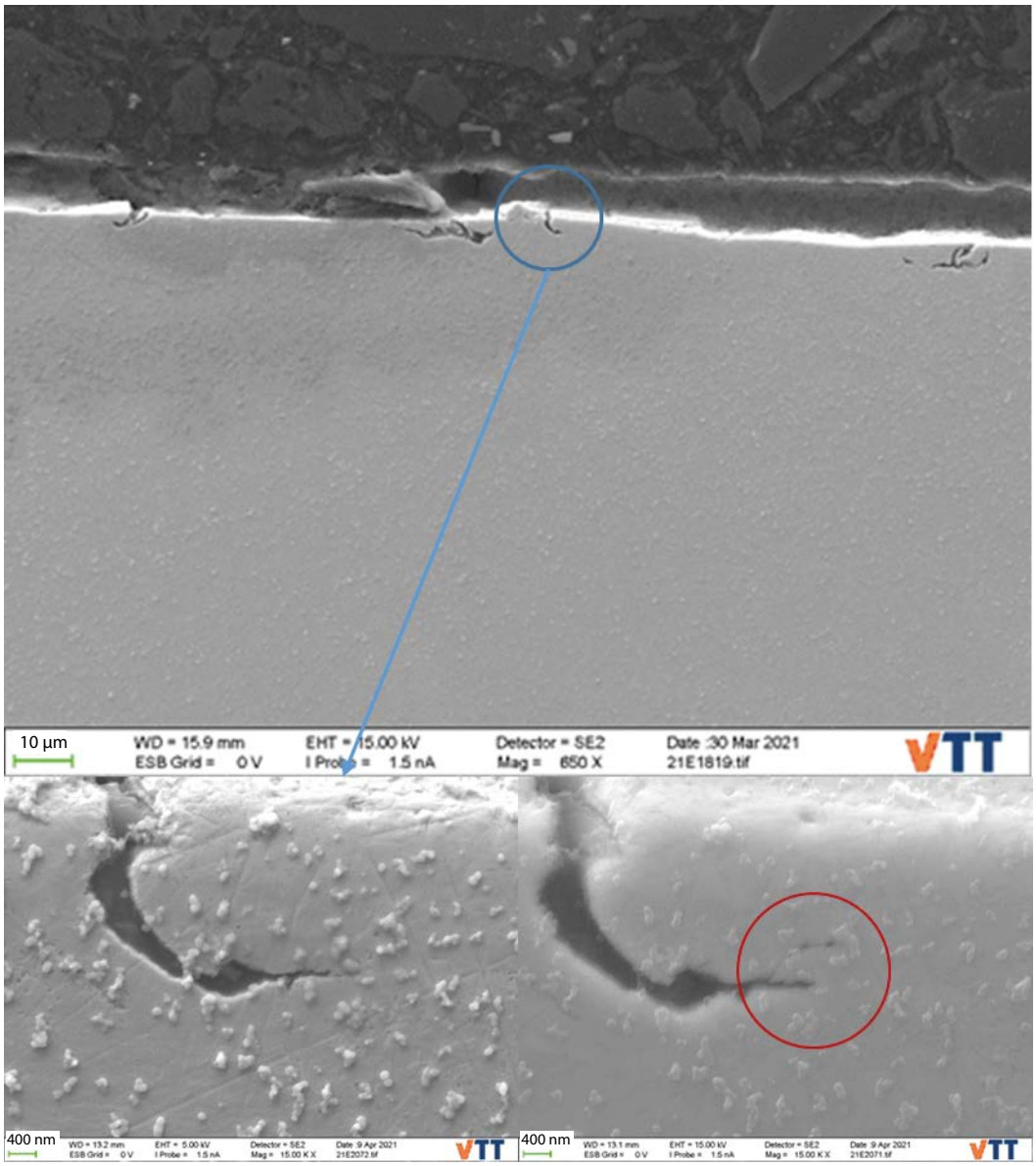

Figure 5-68. *Cross section of SEM sample 4 (creep experiment 8) tested in air. Scale 400 nm. Lower left 5 kV, lower right 15 kV. The red circle depicts the branching of the tip (better discerned with 15 kV).*

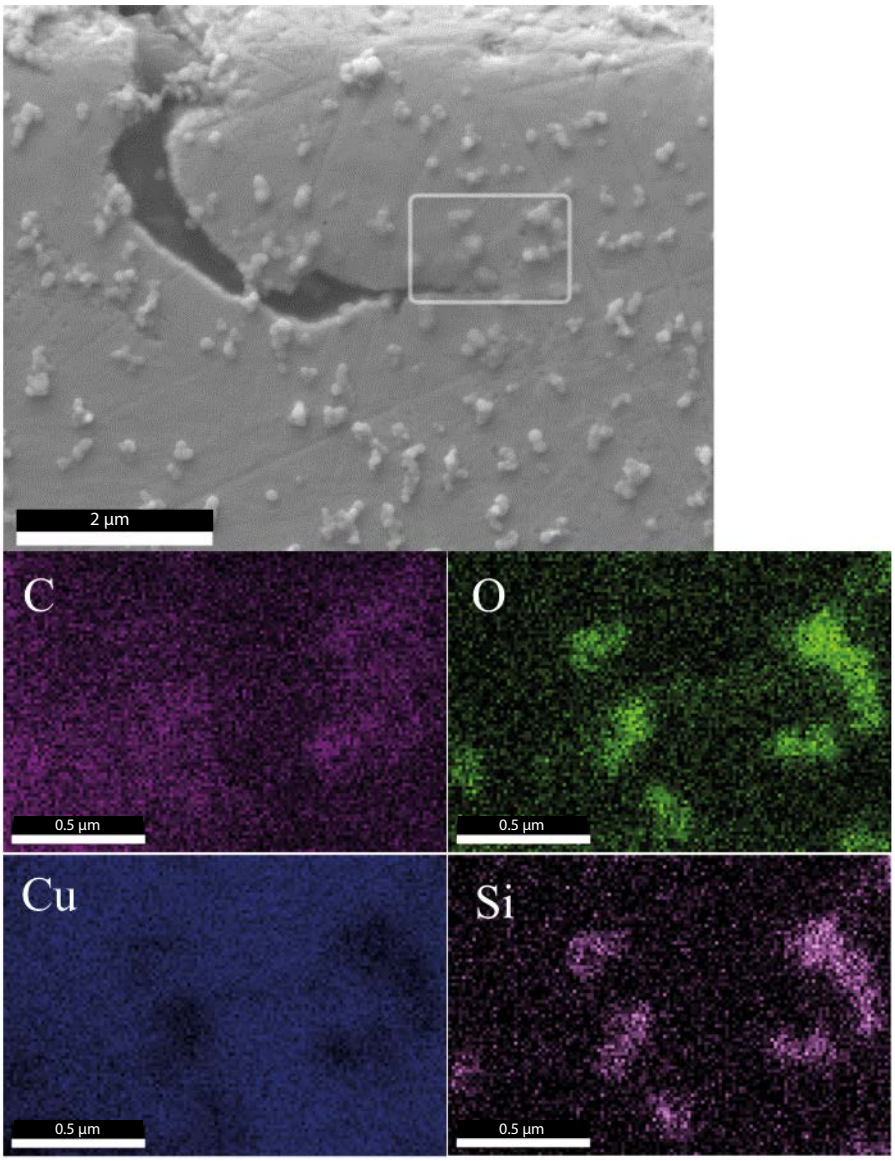

Figure 5-69. *EDS area map of the tip of a surface defect.*

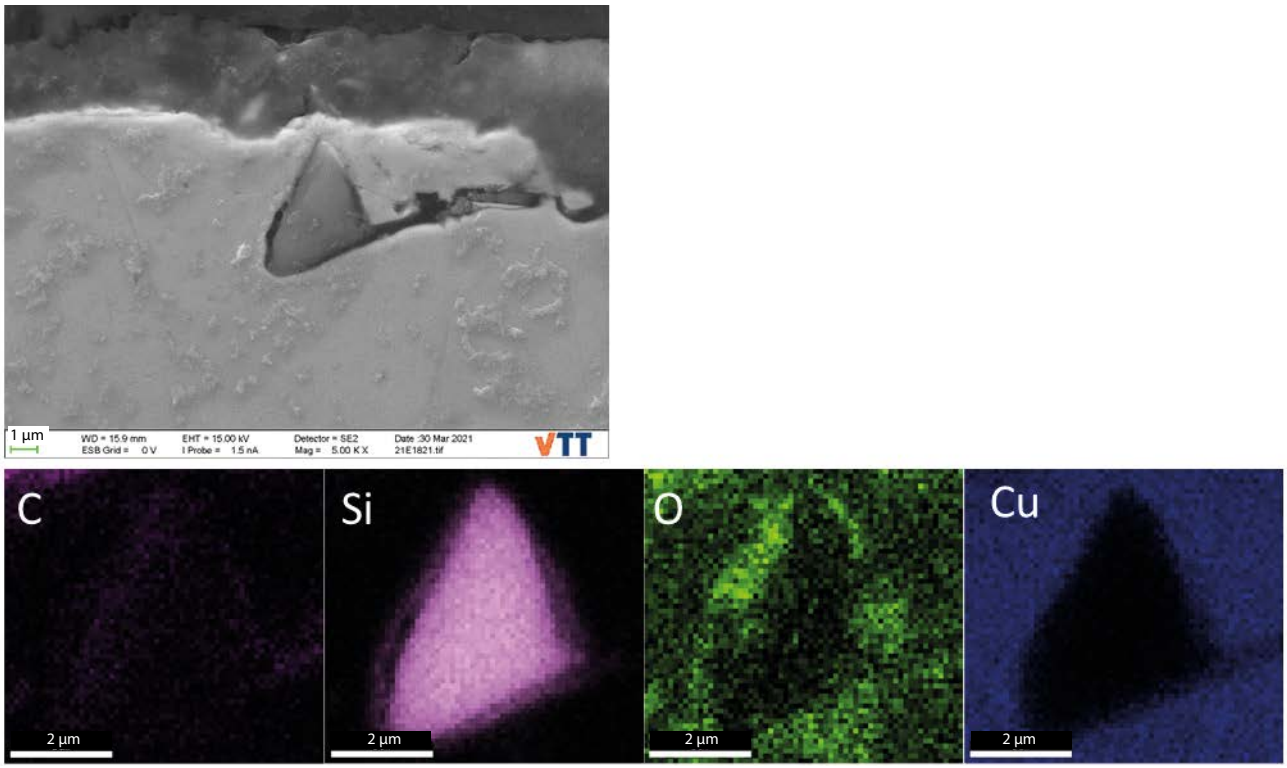

Figure 5-70. *EDS area map of an inclusion (Si) within the surface layer.*

SEM sample 5; creep in water without sulphide

The sample showed a few small surface cracks extending a few µm into the copper material, Figure 5-71. In the about 0.5 mm length covered in Figure 5-71a, only two locations (marked with a blue circle) were identified with a surface crack. Figure 5-71b shows the second one in more detail, revealing three surface cracks with a maximum penetration into the copper material of about 2–3 µm, similar to those found in Sample 4 (tested in air).

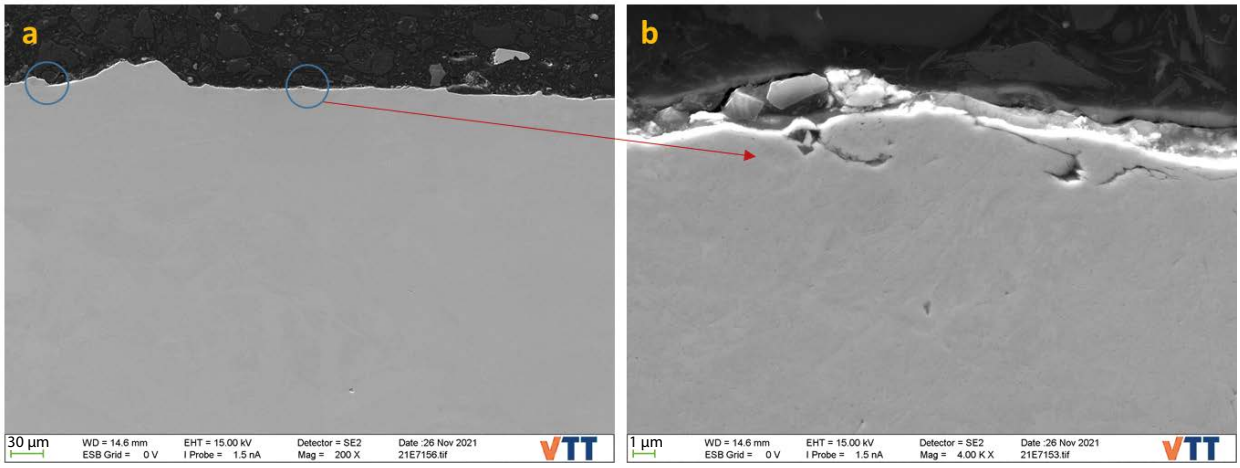

Figure 5-71. *Cross-section of Sample 5 (Creep test Nr 7).*

5.3.3 SEM of surfaces with sulphide film removed

This investigation was performed mainly to verify whether the crack-like features found in the sulphide film (see e.g. Figure 5-51 to Figure 5-53) indicate micro-cracks in the underlying copper metal. The sulphide film on creep experiment 3 (with one anodic polarization) and creep experiment 6 (with three cathodic polarizations), was removed by a chemical treatment, after which the surface was studied with SEM. The method used was developed by Dr. J. Chen and Prof. D. Shoesmith at the University of Western Ontario, and applied according to instructions by e-mail correspondence. The chemical treatment involved the following steps: 1 – remove oxygen from 1 M $HClO_4$ + 0.025 M $C_6H_{12}N_4$ (hexamethylenetetramine) solution by bubbling with high-purity Ar for at least 45 min; 2 – immerse the Cu sample into the solution for 3 min; 3 – rinse the Cu sample with ion pure water and dry with Ar gas; 4 – remove the corrosion products using an adhesive tape by applying it to the surface and removing the tape rapidly; 5 – repeat (4) until no further corrosion products can be removed, 6 – sonicate the Cu sample in methanol for 20 min, and 7 – rinse the Cu sample with ion pure water, dry the sample using a jet of Ar stream, and store the sample in a desiccator.

Figure 5-72 shows the stereomicroscope pictures of samples 3 and 6 after the sulphide film removal. Based on these it seems that the removal was not complete (despite several adhesive tape applications), since there are darker areas on the surfaces. The darker areas are much smaller and much more numerous on the sample from experiment 3 compared to the sample from experiment 6.

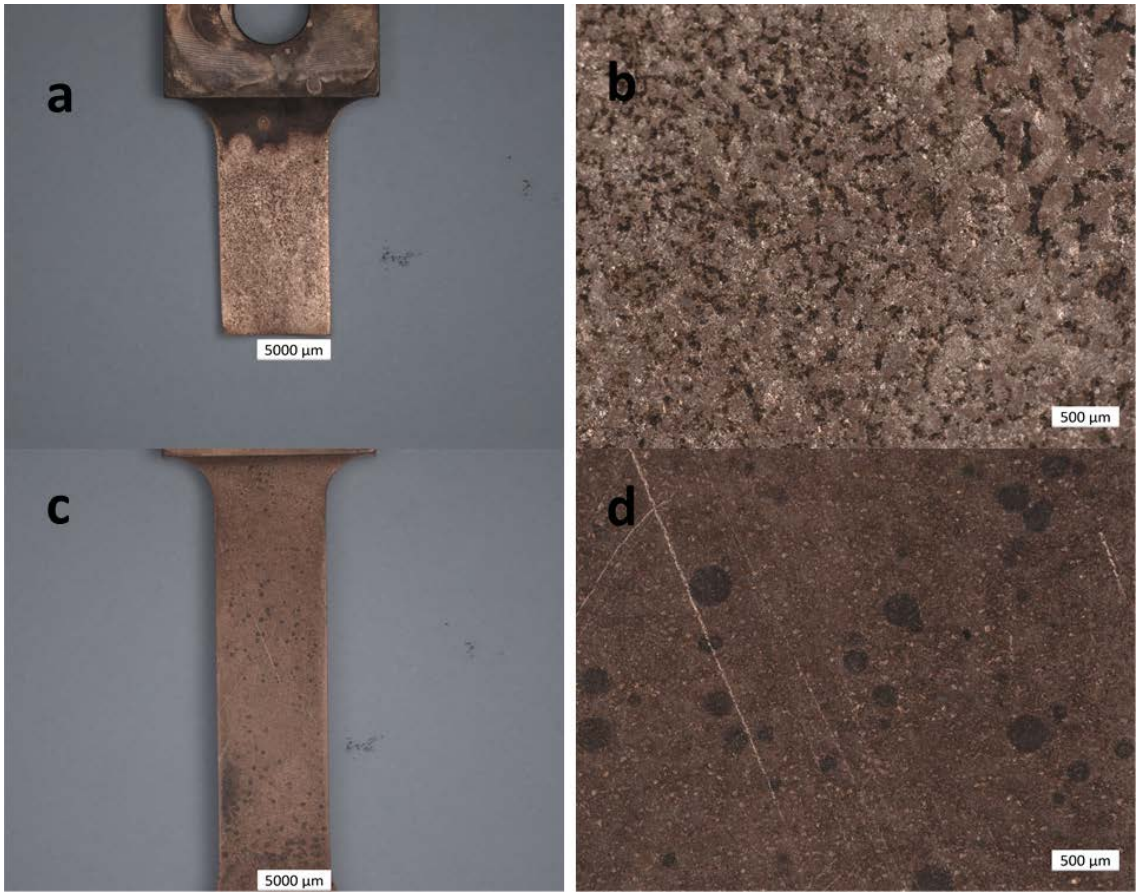

Figure 5-72. *Stereo pictures of samples from experiment 3 (a and b) and experiment 6 (c and d) after the sulphide film removal.*

The surfaces were further studied with SEM. In case of creep experiment 3, the surface cracks were easy to detect, Figure 5-73, indicating that the cracks seen in the sulphide film (Figure 5-51–Figure 5-53) were most probably due to the micro-cracks forming in the copper material and not due to e.g. stresses produced by volume changes in the sulphide. The EDS-analysis of the surroundings of one micro-crack shown in Figure 5-74 indicated the presence of only Cu (spots 1 and 2), Cu with 0.6 % Ni (spot 3) and Cu with 7.2 % C (spot 4). It is noteworthy here that even though some of the EDS spots analysed reside in areas thought to represent the darker areas shown in Figure 5-72, no sulphide was detected.

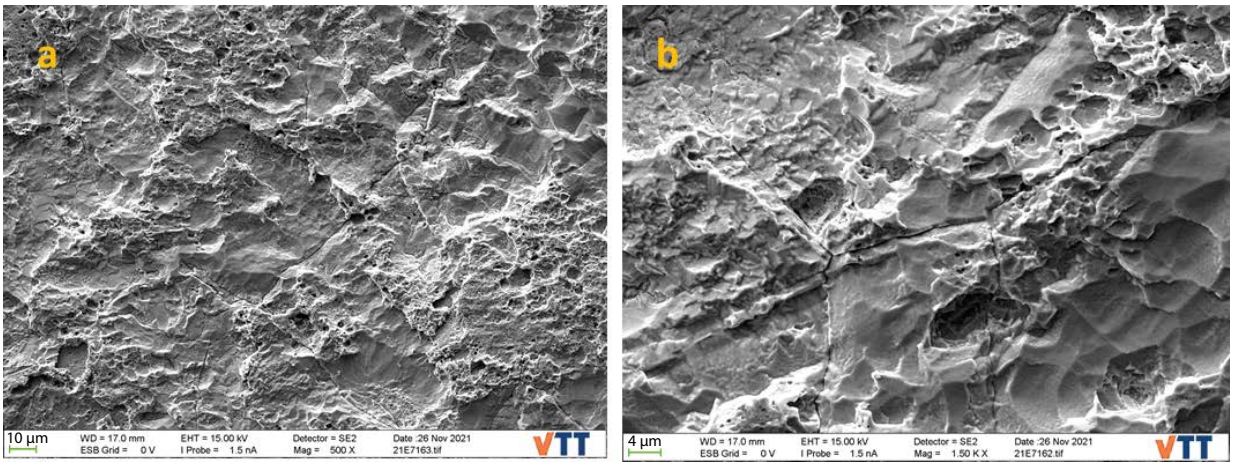

Figure 5-73. *SEM-pictures of the surface of specimen from creep test Nr 3 after sulphide film removal. Scales: a – 10 µm, b – 4 µm.*

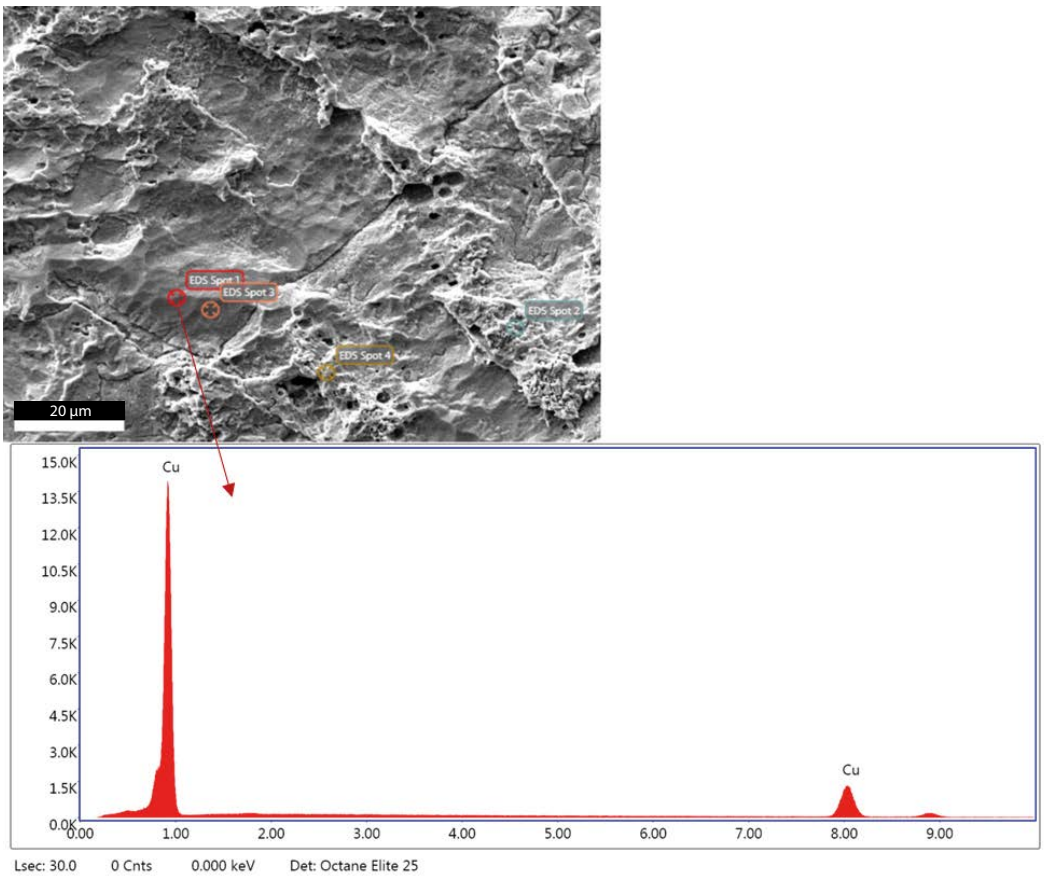

Figure 5-74. *SEM-picture of the surface of specimen from creep test Nr 3 after sulphide film removal, with four EDS points.*

In the case of creep experiment 6, micro-cracks were also found, Figure 5-75, although clearly less than on the specimen from creep experiment 3. Similarly to the specimen from creep experiment 3, the EDS-analysis of the surroundings of one micro-crack (Figure 5-76) indicated the presence of only Cu (spots 1 and 2), Cu with 9.0 % O (spot 3) and Cu with 8.2 % C (spot 4).

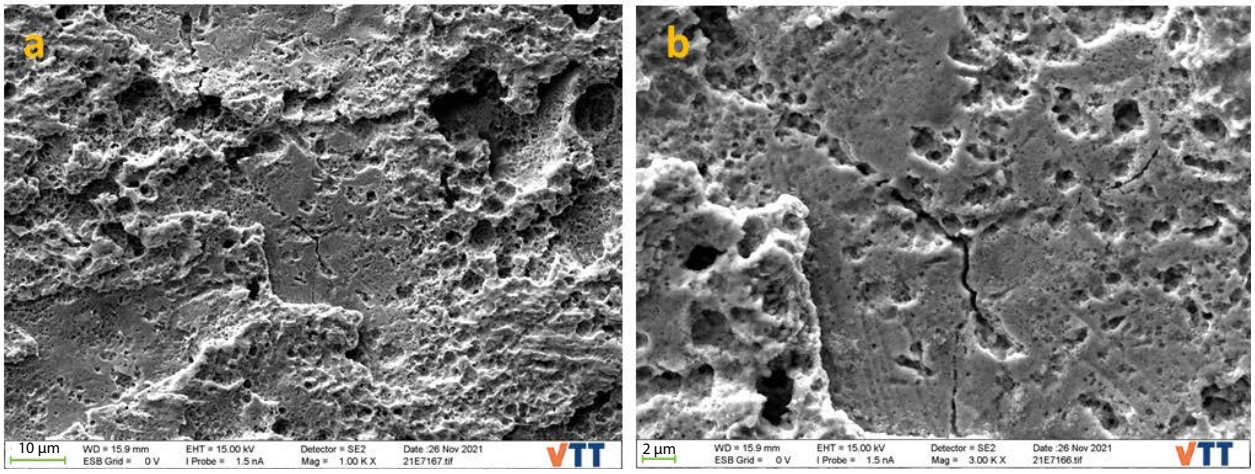

Figure 5-75. *SEM-pictures of the surface of specimen from creep test Nr 6 after sulphide film removal. Scales: a – 10 µm, b – 2 µm.*

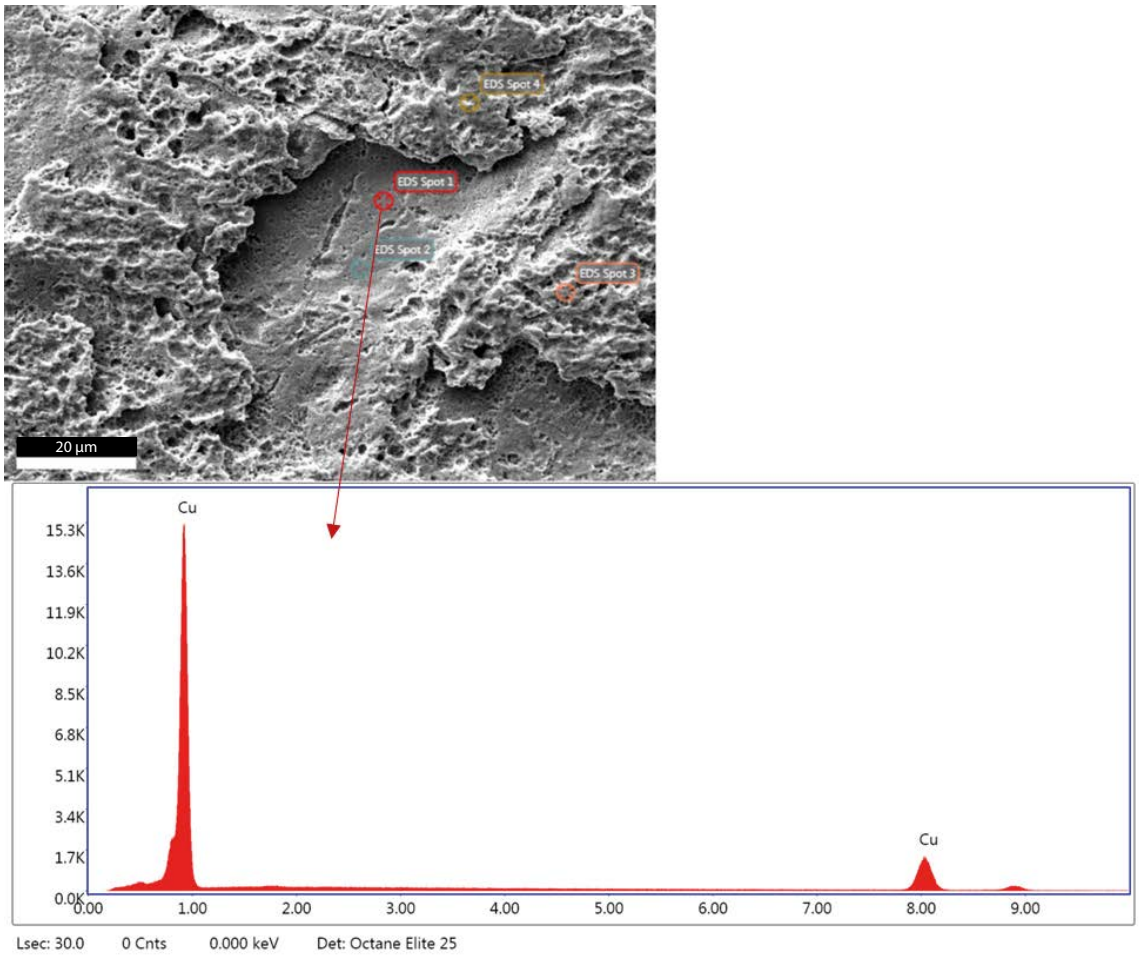

Figure 5-76. *SEM-picture of the surface of specimen from creep test Nr 6 after sulphide film removal, with four EDS points.*

5.3.4 Summary of SEM findings of the creep specimens

- At the shoulder area outer surface of all specimens, machining marks with some defects can be observed. However, the surface defects were found not to extend into the base material. The cross section SEM only revealed some machining marks.
- The surface film thickness of samples 1 (tested in 1 M $NaNO_2$), 2 (tested in 10^{-4} M HS^-) and 3 (tested in 10^{-3} M HS^-) was around 14, 9 and 6 µm, respectively. Mind that the thickness of surface film can vary locally. In sample 4 (creep experiment 8 tested in air), no surface film was detected. No surface defects or machining marks were found to penetrate the surface film. Real SCC cracks can penetrate the surface film, as observed in sample 1.
- Some crack-like surface defects were observed at the cross section of body part in sample 4 (creep experiment 8 tested in air), with a sharp tip with tip-branching. The crack-like surface defects were most likely formed by the mechanical opening of the pre-existing machining marks or surface defects during the creep testing. Si-containing inclusions were observed from the cross section of the sample 4.
- There is a radical difference in the surface appearance of samples 2 and 3 at the body part. SEM shows a very different surface appearance with lots of deposited crystals in case of sample 3 and no such crystals in case of sample 2. However, the shoulder part of samples 2 and 3 are similar. Potential boundary attack was observed in specimen 2. The surface layer consisted of hexagonal crystals and an amorphous structure surrounding the hexagonal crystals on specimen 3. The differences of surface film morphology and structure between specimens 2 and 3 most likely stem from the anodic dissolution at the end of test 2, which has led to the dissolution and reduction of surface films. Hexagonal crystals mainly consist of Cu-S-O and the amorphous-like structure mainly of Na-P-O.
- For the specimens tested in water environment (with or without sulphur), the O content in the surface film has a depletion in the mid of the film and an enriched O layer can be seen at the boundary of surface film layer and the base material. The enriched O layer at the lower bound can be clearly observed as oxides in the low-kV SE images. The enriched O layer at the interface between the matrix and the surface film was analysed with the low-kV SE images and low kV EDS points analysis, which indicate the enriched O layer was formed by Cu-O-S crystals with dimension of 100–300 nm.
- Clear matrix dissolution and oxidation along the SCC cracking path was observed. As seen in the cross section of sample 1, there are SCC cracks in both TG and IG mode (BSE images), which are in accordance with the fracture surface.
- Crack-like surface defects extending a few µm into the Cu-OFP material were detected in the cross section of the body of sample 4 (but not in the shoulder area) never exposed to water. Thus, they are most probably due to pre-existing defects within the material opening up due to plastic deformation and not formed by reactions with the environment (air). In other samples, such defects would have been consumed by the oxidation process forming surface layers 6 to 14 µm thick, and would thus not be any more detected in the cross-sections. Not being able to find crack-like defects in the cross-sections of the samples tested in water actually indicates that they are pre-existing or that they form (open-up) very early during the test so that the forming surface film is able to “consume” them.
- Since the crack-like defects in sample 4 (creep experiment 8 tested in air) and real cracks in sample 1 tested in 1 M $NaNO_2$ are clearly detectable in the cross-sections, it can be concluded that the polishing method used does not “smear” copper metal onto the small details and hide them.
- No sulphur (S) was detected in the cross-sections (only in the outer surfaces) of samples 2 and 3, although the samples were exposed to 25 mg/l of HS^-. It is proposed that most of the Cu_2S had dissolved after stopping the sulphide feed, and the deposited crystals were detached from the surface during preparation of the SEM cross-section samples and thus would not be seen in the analyses. Copper sulphide, probably due to its non-protective character, is proposed to dissolve rather easily when the sulphide “pressure” from the environment is removed.

- After removing the sulphide layer (by chemical treatment) from two samples (creep experiments 3 and 6), surface microcracks were identified with maximum length of about 20–30 μm.
- The temporary increase in creep rate (by about two orders of magnitude) after stopping the sulphide feed, lasting about 7 and 50 hours in case of samples 2 and 3, respectively, could be explained by the reductive dissolution of Cu_2S, producing vacancies that promote creep rate. Thus, the mechanism of creep acceleration would be similar to that observed due to the anodic polarisations and not likely related to hydrogen.

6 Validation of results

The method used to study creep in Cu-OFP used in this study was validated by performing a creep test at room temperature with standard conventional creep testing equipment (dead load) with a square cross-section specimen geometry. Both methods resulted in closely similar creep rates, thus confirming the reliability of the method and specimen geometry used in further tests of this study. The finding of remnants of the EDM manufacturing procedure on the surface of some of the specimens (despite the polishing), possibly causing the microcrack-like defects found on some locations could be thought to have an influence on the results. However, the fact that the observed microcrack-like defects (possibly acting as favourable SCC crack initiation sites) did not cause SCC cracks to form in Cu-OFP samples exposed to sulphide indicates that sulphide is not likely to cause SCC in Cu-OFP.

7 Summary and Discussion

The method of creep testing used in this work has been shown to be reliable through comparison of creep data measured using a standard conventional (dead weight) method and the current method in air at room temperature (Figure 5-21).

The main objectives of this work were to find if the creep rate of Cu-OFP is influenced by the presence of sulphide and either anodic or cathodic polarisation. In the first part of the study performed in sodium nitrite (1 M $NaNO_2$) without sulphide, the creep rate was found to be accelerated by anodic polarisation to +1 mA/cm^2, in line with the results by Aaltonen et al. (2003). However, the reason for the acceleration remains somewhat unresolved since the specimen failed by SCC, and the contribution of SCC micro-cracks (forming early on during the test) onto the creep rate could not be determined.

The test in $NaNO_2$ solution and the tests in sulphide containing buffer solution show that anodic polarisation to +1 mA/cm^2 results in (a transient) acceleration of the Cu-OFP creep rate. At lower anodic current densities of +0.05 and +0.1 mA/cm^2 creep acceleration was not present, and since these sequences were preceded by the more heavy anodic polarisation, no definite conclusion can be made of the influence of the current density level.

Presence of sulphide tends to lower the creep rate of Cu-OFP during anodic polarisation. In two strictly comparable experiments, anodic polarisation to +1 mA/cm^2 resulted in an increase of the strain rate to about 3×10^{-6} 1/s with [HS^-] = 3 mg/l (Figure 5-8), and to about 2×10^{-7} 1/s with [HS^-] = 25 mg/l (Figure 5-15), indicating an inverse correlation of sulphide concentration and the maximum strain rate achieved during the anodic polarisation. Under open circuit conditions (i.e. without polarisation), addition of sulphide had no measurable effect on the strain rate. However, stopping the sulphide feed (at [HS^-] = 25 mg/l) resulted, after some incubation time, in an (transient) increase of strain rate by about an order of magnitude.

Cathodic polarisation can also result in a transient increase of creep rate (test 5 and test 7). This effect was found to occur mainly during the first cathodic polarisation sequence only (in a series of similar polarizations). This result may be linked to the presence of a surface film (reductive dissolution injecting vacancies into the Cu-OFP and accelerating creep in a transient manner).

Comparing the results of cathodic polarisations (to −1 mA/cm^2) in test 5 (without preceding sulphide exposure) and in test 6 (with preceding sulphide exposure) shows that the presence of sulphide film on Cu-OFP brings about a marked (although transient) increase in the strain rate as a result of the cathodic polarisation. This could indicate, if one assumes that the increase in strain rate is caused by hydrogen interaction with the dislocation structure in Cu-OFP that the sulphide film acts as a hydrogen recombination poison thus increasing the amount of hydrogen entering the Cu-OFP material.

Assuming that at the pH = 7.2 used in this study, almost all of the sulphide in the water phase is in the form of HS^-, formation of a copper sulphide film on the surface releases H^+, which, if the sulphide film acts as a recombination poison, has a better chance of entering the Cu-OFP material (as atomic H) even without external cathodic polarisation. The result that the strain rate seems to increase after termination of the sulphide feed and not during it needs further investigations.

Presence of sulphide (up to 25 mg/l) tends to lower the creep rate of Cu-OFP during anodic polarisation, indicating an inverse correlation of sulphide concentration and the maximum strain rate achieved during the anodic polarisation. Surface inspection with scanning electron microscope after exposure to both sulphide and anodic polarisation showed a number of line shaped openings, the length of which corresponds rather well with the grain size (≈100 µm) of the Cu-OFP material. The inclination of the lines was often close to 45° to the tensile axis, and other inclinations also appear. A further SEM-study, performed after chemically removing the sulphide film, showed that there were crack-like surface defects also under the sulphide film.

Cross-sections studied with SEM revealed crack-like surface defects extending a few μm into the Cu-OFP material in specimens tested in air and in water without sulphide, but not in specimens tested in water with sulphides. This was explained by the rather thick sulphide film (about 10 μm) having consumed the Cu-OFP surface material in which the crack-like surface defects appeared in the specimens tested in air and water without sulphide.

Under open circuit conditions (i.e. without polarisation), addition of sulphide had no measurable effect on the strain rate. However, stopping the sulphide feed resulted, after some incubation time, in a transient increase of strain rate by about an order of magnitude, lasting for about 40 hours. Cathodic polarisation resulted in some cases in a similar transient increase of strain rate. These results may possibly be due to hydrogen entering the Cu-OFP material and interacting with the dislocation structure or to reductive dissolution of surface films resulting in injection of vacancies into Cu-OFP, which again accelerate creep. Strenghtening either of these hypotheses would need further investigation.

8 Conclusions

Based on the results, the following main conclusions were made:

- The creep rate of Cu-OFP increases (in a transient manner) when a strong anodic polarization (+1 mA/cm^2, corresponding to a corrosion rate of about 1 mm/y) is applied.
- Cathodic polarisation was found to also accelerate creep rate of Cu-OFP (again only in a transient manner) under some conditions.
- Sulphide exposure per se was found not to affect the creep rate of Cu-OFP. However, when sulphide feed was stopped, a transient increase in the creep rate was observed.
- Crack-like surface defects (a few tens of μm in length) were observed by SEM in surfaces of specimens tested in air, in water without sulphide and in sulphide containing environments.
- The crack-like surface defects were found (in SEM cross-sections) to extend a few μm into the Cu-OFP material in specimens tested in air and in water without sulphide, but not in specimens tested in water with sulphides. The absence of crack-like surface defects in the cross-sections of specimens tested in water with sulphides was assumed to result from the surface films being so thick (about 10 μm) that these defects had been consumed by the surface films, indicating that sulphide corrosion had removed them.
- The fact that the crack-like surface defects did not appear in cross-sections of specimens tested in water with sulphides indicates that such crack-like defects are not able to grow in the sulphide containing water (at a higher rate than general corrosion), i.e. Cu-OFP is not susceptible to SCC in presence of sulphides at the studied concentration of about 25 mg/l.

References

SKB's (Svensk Kärnbränslehantering AB) publications can be found at www.skb.com/publications. SKBdoc documents will be submitted upon request to document@skb.se.

Aaltonen P, Jagodzinsky Y, Hänninen H, 2003. Vacancy generation in electrochemical oxidation/dissolution of copper in $NaNO_2$ solution and its role in SCC mechanism. In Moody N R (ed). Hydrogen effects on material behavior and corrosion deformation interactions: Proceedings of the International Conference on Hydrogen Effects on Material Behavior and Corrosion Deformation Interactions, Jackson Lake Lodge, Wyoming, 22–26 September 2002. The Minerals, Metals, and Materials Society, 597–606.

Chen J, Qin Z, Martino T, Shoesmith D W, 2017. Effect of chloride on Cu corrosion in anaerobic sulphide solutions. Corrosion Engineering, Science and Technology 52, sup 1, 40–44.

dos Santos Afonso M, Stumm W, 1992. Reductive dissolution of iron(III) (hydr)oxides by hydrogen sulfide. Langmuir 8, 1671–1675.

Kinnunen P, Varis P, 2011. Stress corrosion cracking investigation of copper in groundwater with ammonium under potential polarisation. Posiva Working Report 2011-05, Posiva Oy, Finland.

Leijon G, Ahlström J, Andersson-Östling H C M, 2018. In situ hydrogen charging of OFP copper during creep. SKB R-17-17, Svensk Kärnbränslehantering AB.

Mannesson K, Andersson-Östling H C M, 2016. Stress application and the effect on creep of copper. SKB R-14-31, Svensk Kärnbränslehantering AB.

Nečas D, Klapetek P, 2012. Gwyddion: an open-source software for SPM data analysis. Central European Journal of Physics 10, 181–188.

Revie R W, Uhlig H H, 1974. Effect of applied potential and surface dissolution on the creep behavior of copper. Acta Metallurgica 22, 619–627.

Välimäki T, 2009. SKB T58 tube structure evaluation. Report 1.6.2009, Luvata Pori Oy. SKBdoc 1216615 ver 2.0, Svensk Kärnbränslehantering AB.

Yagodzinsky Y, Malitckii E, Saukkonen T, Hänninen H, 2012. Hydrogen-enhanced creep and cracking of oxygen-free phosphorus-doped copper. Scripta Materialia 67, 931–934.

Arkitektkopia AB, Bromma, 2022

SKB is responsible for managing spent nuclear fuel and radioactive waste produced by the Swedish nuclear power plants such that man and the environment are protected in the near and distant future.

skb.se